Computer Physics Communications 316 (2025) 109766

Contents lists available at ScienceDirect

Computer Physics Communications

journal homepage: www.elsevier.com/locate/cpc

Computer Programs in Physics

BSMPT v3
a tool for phase transitions and primordial gravitational waves in extended Higgs sectors

Philipp Basler [a,1], Lisa Biermann [a,1], Margarete Mühlleitner [a,*,1], Jonas Müller [a,1], Rui Santos [b,c,1], João Viana [b,1]

[a] Institute for Theoretical Physics, Karlsruhe Institute of Technology, Wolfgang-Gaede-Str. 1, 76131 Karlsruhe, Germany
[b] Centro de Física Teórica e Computacional, Faculdade de Ciências, Universidade de Lisboa, Campo Grande, Edifício C8, 1749-016 Lisboa, Portugal
[c] ISEL - Instituto Superior de Engenharia de Lisboa, Instituto Politécnico de Lisboa, 1959-007 Lisboa, Portugal

ARTICLE INFO

The review of this paper was arranged by Prof. Z. Was

ABSTRACT

Strong first-order phase transitions (SFOPT) during the evolution of the Higgs potential in the early universe not only allow for the dynamical generation of the observed matter-antimatter asymmetry, they can also source a stochastic gravitational wave (GW) background possibly detectable with future space-based gravitational waves interferometers. As SFOPTs are phenomenologically incompatible with the Standard Model (SM) Higgs sector, the observation of GWs from SFOPTs provides an exciting interplay between cosmology and particle physics in the search for new physics. With the C++ code BSMPTv3, we present for the first time a tool that performs the whole chain from the particle physics model to the gravitational wave spectrum. Extending the previous versions BSMPTv1 and v2, it traces the phases of beyond-SM (BSM) Higgs potentials and is capable of treating multiple vacuum directions and multi-step phase transitions. During the tracing, it checks for discrete symmetries, flat directions, and electroweak symmetry restoration, and finally reports the transition history. The transition probability from the false to the true vacuum is obtained from the solution of the bounce equation which allows for the calculation of the nucleation, percolation and completion temperatures. The amplitude and characteristic frequencies of the GWs originating from bubble collisions and highly relativistic fluid shells, sound waves and turbulence, are evaluated after the calculation of the thermal parameters at the transition temperature, and finally the signal-to-noise ratio at LISA is provided. The code BSMPTv3 is a powerful self-contained tool that comes more than timely and will be of great benefit for investigations of the vacuum structure of the early universe of not only simple but also complicated Higgs potentials involving several vacuum directions, with exciting applications in the search for new physics.

Contents

* Corresponding author.
E-mail addresses: philipp.basler@alumni.kit.edu (P. Basler), lisa.biermann@kit.edu (L. Biermann), margarete.muehlleitner@kit.edu (M. Mühlleitner), rasantos@fc.ul.pt (R. Santos), jfvvchico@hotmail.com (J. Viana).
[1] All authors can be reached via: bsmpt@lists.kit.edu.

https://doi.org/10.1016/j.cpc.2025.109766
Received 1 August 2024; Received in revised form 23 June 2025; Accepted 13 July 2025

Available online 7 August 2025

NEW VERSION PROGRAM SUMMARY

Program Title: BSMPT - Beyond the Standard Model Phase Transitions: A C++ package for the computation of phase transitions and of gravitational waves sourced by first-order phase transitions (FOPT) in beyond-Standard-Model (BSM) theories with extended Higgs sectors.
CPC Library link to program files: https://doi.org/10.17632/sjtp7bb33t.2
Developer's repository link: https://github.com/phbasler/BSMPT
Licensing provisions: GPLv3
Programming language: C++17
Journal reference of previous version: Comput. Phys. Commun. 269 (2021) 108124, https://doi.org/10.17632/sjtp7bb33t.1
Does the new version supersede the previous version?: Yes
Reasons for the new version: Add algorithms for multi-step phase tracking, the computation of the bounce solution, of thermal parameters and of the spectrum of gravitational waves sourced by FOPTs.
Summary of revisions: BSMPTv3 can track multiple non-global and global minima of the effective potential as a function of the temperature, solve the bounce equation to calculate the tunnelling rate and compute the spectrum of the primordial gravitational waves sourced by FOPT as well as their signal-to-noise ratio at LISA, a future space-based gravitational waves observatory.
Nature of problem: Scalar extensions are promising models capable of providing a strong first-order electroweak phase transition, one (i.e. departure from thermal equilibrium) of the three Sakharov conditions for successful electroweak baryogenesis. Furthermore, they can provide additional sources of CP violation, which is another Sakharov condition. Such FOPT can source gravitational waves that are possibly detectable at future GW observatories. In order to decide if and which phase transitions take place during the evolution of the universe, the effective potential of the model under consideration has to be computed at higher orders including the thermal mass corrections. Its non-global and global minima then have to be traced as function of the temperature. For overlapping minima, the tunnelling rate from the false to the true minimum needs to be calculated. For this the bounce equation has to be solved. For the phase transitions that take place, the thermal parameters are then determined. They are required for the computation of the generated GW spectrum. Finally, the signal-to-noise ratio is computed for the future GW observatory LISA.
Solution method: The minima are tracked across the temperature range by using a Newton-Raphson method with seed points determined by the BSMPTv2 routines. For the computation of the tunnelling rate, the bounce equation is solved by the path deformation algorithm. This consists of splitting the bounce equation into a tangential and a perpendicular component, and then solve it iteratively until convergence is reached. With the

tunnelling rate as a function of the temperature, the nucleation, percolation and completion temperatures are calculated as well as the other thermal parameters (released latent heat, inverse time scale) required for the computation of the GW spectrum. The computations of the spectrum and its respective signal-to-noise ratio are performed using results from numerical simulations and fits available online.

Additional comments including restrictions and unusual features: The wall velocity is considered an input parameter. It can be set to a specific constant value or alternatively chosen between two different approximations. If none of these is chosen, the wall velocity is set by default to 0.95. Models with a spontaneously broken discrete symmetry can lead to domain walls. The code does not take into account the possible existence of different domains separated by domain walls. In this case, only phase transitions with the shortest path between false and true vacuum are considered. The code assumes only one transition taking place between one pair of false and true vacuum phases. The code calculates GWs originating from bubble collisions and highly relativistic fluid shells, sound/shock waves and magneto-hydrodynamic turbulence.

1. Introduction

Despite the success of the Standard Model (SM), which has been structurally completed with the discovery of the Higgs boson [1,2] and tested to great accuracy, there are open questions which cannot be answered by the SM. The investigation of the development of the vacuum structure during the evolution of the universe allows us to get exciting insights, which may help to find answers to some long-standing open problems. Among these is the question of the generation of the observed baryon asymmetry [3] of the universe. A dynamical explanation is given by electroweak baryogenesis (EWBG) [4–12], provided the three Sakharov conditions [13] are fulfilled. While these could in principle be met by the SM, for the measured value of the SM-like Higgs mass of 125 GeV, there is a smooth cross-over [14,15]. Since EWBG requires a strong first-order electroweak phase transition (SFOEWPT), compatibility with Higgs phenomenology hence leads to the investigation of beyond-the-SM (BSM) Higgs sectors. The requirement of an SFOEWPT restricts the allowed parameter space of BSM models entailing observable consequences at collider experiments, like the Large Hadron Collider (LHC), and provides us with an indirect probe of new physics scenarios.

The first direct observation of gravitational waves (GWs) reported by the LIGO Collaboration in 2016 [16], was awarded the Nobel Prize for physics in 2017 and initiated a new era of multi-messenger astronomy. Future GW observatories with increased sensitivity provide new exciting avenues with unprecedented opportunities for the exploration of particle physics. Thus, first-order phase transitions (FOPTs) can source a stochastic gravitational wave background that can be detectable with future space-based gravitational waves interferometers. This would not only provide us with the exciting possibility to directly probe the echo of a cosmological FOPT, but it would also amount to the discovery of physics beyond the SM.

The combination of collider phenomenology and cosmological observations is hence an exceptional opportunity to get insights into the true physics that underlies nature, spanning a large range of energy scales. For this to be meaningful, we have to consistently combine information from collider observables and gravitational wave observation. Specific new physics models, that fulfil all relevant theoretical and experimental constraints, are tested w.r.t. their ability to induce an FOPT, and if the gravitational wave spectrum that is generated during this transition may be detectable at future GW observatories. This program has to be performed at the highest possible precision taking into account all available state-of-the-art information. There exist several codes that are publicly available, which trace the minima of extended Higgs sector potentials at non-zero temperature some of which also determine the bounce action. None of these codes, however, performs the whole chain from testing an arbitrary extended Higgs sector model w.r.t. its constraints via tracing the minima of its scalar potential at non-zero temperatures, the determination of the bounce solution and the possible phase transitions, to the computation of the gravitational wave spectrum originating from these first-order phase transitions, in a self-contained way. Moreover, some codes become very slow and even fail when it comes to the determination of the various vacuum phases of involved potentials with multiple field directions. Last but not least, the widely used code `CosmoTransitions` [17] is not publicly maintained any more.

It is hence timely and imperative to develop a new self-contained code being able to perform the whole chain of calculations starting from a particle physics model considering all relevant constraints to the spectrum of gravitational waves from FOPTs, implementing the state-of-the-art approaches at highest available precision, which are updated constantly when new developments appear. This is the aim of the `C++` code `BSMPT` and the here presented extension `BSMPTv3`. With `BSMPTv1/v2` [18,19] and the link to `ScannerS` [20–24] the check of new physics models w.r.t. their potential of generating an FOPT while simultaneously being compatible with all relevant theoretical and experimental constraints is possible. In this paper, we present the new release `BSMPTv3`, a `C++` code that extends the previous versions substantially by the ability to

- track temperature-dependent coexisting minimum phases over arbitrary temperature intervals;
- trace multi-step phase transitions;
- deal with discrete symmetries;
- deal with flat directions;
- test electroweak symmetry restoration at high temperature;
- calculate the bounce solution for regions of coexisting minima;
- determine the critical temperature, the nucleation temperature, the percolation temperature, the completion temperature, and the reheating temperature;
- calculate the released latent heat α and the inverse time scale β/H of the phase transition;
- derive the amplitude and characteristic frequencies of gravitational waves, with bubble collisions and highly relativistic fluid shells, sound waves and turbulence as their possible origins;
- calculate the signal-to-noise ratio at `LISA`;

for all models implemented in `BSMPT` and those included by the user.

The outline of the paper is as follows. We start with a description of the state-of-the-art and the new features of `BSMPTv3` in Sec. 2. In Sec. 3, we describe in great detail the program. After giving details on download and installation in Sec. 3.1, we describe the structure and new algorithms of the code, before moving on to the presentation of the newly implemented classes `MinimumTracer`, `BounceSolution`, `GravitationalWave`, and `TransitionTracer` in Secs. 3.3-3.6. Subsequently, we describe the new executables `MinimaTracer`, `CalcTemps`, `CalcGW` and `PotPlotter` in Secs. 3.7-3.10, as well as new stand-alone features in Sec. 3.11. We finish the program section in Sec. 3.12 with the summary on the status codes that are given out. Section 4 contains example runs, the discussion of their results as well as comparisons with the existing code `CosmoTransitions`.

Our conclusions are given in Sec. 5. The appendix details the improvement on the bosonic thermal function used in BSMPT that we implemented together with this new version of the code.

2. State-of-the-art and new features

The vacuum structure of the universe is theoretically described by the effective Higgs potential at non-zero temperature. As the universe cools down and expands, its vacuum structure changes. At a certain temperature a new minimum evolves which may eventually become degenerate with the existing one, and finally become the global minimum. The degenerate situation defines the critical temperature T_c and the corresponding critical vacuum expectation value (VEV) v_c, but it does not guarantee that actually a phase transition from the false to the true vacuum takes place. First-order phase transitions from the false to the new true vacuum proceed via bubble nucleation. The bubbles with non-zero VEV evolve and expand until they dominate the universe. These bubbles generate GWs through friction with the thermal plasma and through collisions (see e.g. Refs. [25–29] for reviews).

The crucial quantity for the phase transition is the decay rate of the false vacuum, or in other words the tunnelling rate for the transition from the false vacuum to the true vacuum. The probability for the phase transition to take place at finite temperature is computed via minimisation of the $O(3)$-symmetric Euclidean action S_3, the bounce action, of the scalar field. For the bounce solution the trajectory in field space connecting the local minima needs to be found, which minimises the Euclidean action. This is technically very challenging and is complicated by the fact that the vacuum structure of extended Higgs sector potentials is very involved and changes when loop and temperature effects are included. The behaviour of the ground state of the universe as it cools down is hence highly non-trivial and requires tracing the ground states, given by the minima of the effective potential, as a function of the temperature. Through the decay rate and the Euclidean action the thermal parameters characterising FOPTs are obtained. These are the transition temperature, the inverse duration of the PT and the transition strength given by the latent heat released during the PT. Together with the bubble wall velocity, they ultimately determine the characteristic frequencies and the amplitude of the gravitational wave spectrum.

There are several codes on the market, besides BSMPT, which trace the minima of involved scalar potentials and some of them also provide bounce solutions. They are briefly reviewed here:

- CosmoTransitions [17]: traces minima upwards and downwards in the temperature, initiating the tracing with a collection of starting points that are then optimized locally using a Nelder-Mead-type algorithm. It contains Python modules to calculate the bounce solution via path deformation. The nucleation temperature is obtained using the approximation $S_3(T)/T \lesssim 140$.
- In Vevacious [30] homotopy continuation is exploited to find all extrema of the tree-level potential. These are then used as starting points for gradient-based minimisation of the one-loop effective potential. Tunnelling times are obtained by using CosmoTransitions.
- VevaciousPlusPlus [30,31] has no new implementation of the bounce solution calculation, but a C++ code wrapper of CosmoTransitions interfaced with models in the framework of SARAH [32–35].
- AnyBubble [36] is a Mathematica code for finding bubble nucleation instantons via a multiple shooting algorithm.
- EVADE [37–39] performs the minimisation of the scalar potential through polynomial homotopy continuation and estimates the decay rate of the false vacuum in a multi-scalar theory by using the straight-path approximation.
- BubbleProfiler [40] is a C++ is library for finding the bounce solution via a semi-analytic algorithm formulated in [41].
- The C++ code PhaseTracer [42] tracks phases and identifies critical temperatures using an algorithm that is similar to the one used in CosmoTransitions, but faster. It handles discrete symmetries and can be linked to potentials implemented in FlexibleSUSY [43,44] and BSMPT.
- SimpleBounce [45] applies the gradient flow method from [46] to calculate the bounce solution.
- FindBounce [47] finds the bounce solution via the polygonal multi-field method described in [48].
- OptiBounce [49] obtains the bounce solution via solving the 'reduced' minimisation problem [50].
- TransitionListener [51,52] extends CosmoTransitions by functionalities to study the case of dark sector phase transitions and also derive e.g. stochastic GW spectra and signal-to-noise ratios.

The C++ code BSMPTv1 [18] has been developed to compute the loop-corrected daisy-resummed effective potential of BSM Higgs sectors at non-zero temperature, applying an on-shell (OS) renormalization scheme. It checks for absolute vacuum stability requiring the electroweak vacuum to be the global minimum of the one-loop corrected effective potential at zero temperature. This ensures that we live in a stable vacuum today, however, it excludes the valid parameter region of points with metastable vacuum configurations.[2] Our code BSMPTv1/v2 traces the position of the global minimum for temperatures $T \in \{0, 300\}$ GeV, looking for a discontinuity in the electroweak VEV as the order parameter of the phase transition between the high-temperature symmetric and the electroweak vacuum at $T = 0$ GeV. However, this approach only shows the possible coexistence of two minima. It does not guarantee that the transition actually takes place. It can also not reveal the possible existence of multiple phases during the evolution of the universe. In BSMPTv2 [19] the code was extended to the computation of the generated baryon asymmetry in the CP-violating 2-Higgs-Doublet Model (C2HDM), and included a new model, the Complex Singlet Extension of the SM (CxSM). A detailed description of BSMPTv1 and v2 is given in the two corresponding manuals [18] and [19], respectively, phenomenological investigations using the code can be found in [55–90].

The here presented version BSMPTv3[3] extends BSMPT into a capable single and multi-step phase transition finder. Starting from an absolutely stable electroweak vacuum at zero temperature, it traces the electroweak and all emerging global minima as functions of the temperature and calculates all possible found transitions and key parameters (temperature scales, released latent heat, inverse time scale etc.) as well as the resulting

[2] The electroweak vacuum of the SM at zero temperature is metastable [53,54], its quartic coupling λ is negative for scales $\gtrsim 10^{10}$ GeV and a lifetime larger than the age of the universe.

[3] For a phenomenological study, an early version of the code was used in [91].

gravitational wave spectra. We also implement a framework of status codes that report e.g. on electroweak symmetry non-restoration at high temperature,[4] as well as vacuum trapping.[5]

The code BSMPT with its extension to v3 goes beyond existing codes in the following sense. First of all, the innovations related to the versions v1 and v2 are:

- BSMPT was the first code to implement an on-shell renormalization scheme [55], where, at zero temperature, the loop-corrected masses and mixing angles are renormalized to their corresponding leading-order (LO) values in the minimum of the potential. Crucial for phenomenology, this allows for directly checking the relevant theoretical and experimental constraints of the investigated model without resorting to an involved time-consuming iterative procedure. In this on-shell renormalization scheme UV-finite counterterms are added after the potential has been renormalized in the $\overline{\text{MS}}$ scheme. We have fixed the renormalization scale in the $\overline{\text{MS}}$ scheme to the value of the VEV, $v = 246$ GeV. Since this fixing does not allow to study the renormalisation scale dependence of the obtained results, we provided the option to change the value of the renormalisation scale in the model file. This allows the users to use their own preferred value for the renormalisation scale. Furthermore, it provides the possibility to study the impact of the change of the renormalisation scale on the results. This residual scale dependence originates from the fact that the on-shell renormalisation conditions for the masses and mixing angles are derived for the minimum of the zero-temperature potential and that moreover the Higgs self-interactions are not renormalised on-shell.
- The code can be easily linked to ScannerS [20–24], so that extensive scans in the parameter spaces of the investigated models can be performed checking for the relevant theoretical constraints, implemented in ScannerS, and (through the links to HiggsBounds [97–103] and HiggSignals [104–107], which have been recently merged into the new package HiggsTools [108], and MicrOMEGAs [109–118]) for the experimental collider and DM constraints. ScannerS also checks for flavour constraints, and, in CP-violating models, tests the compatibility with results from the electric dipole moments.
- Several models are already pre-implemented, namely the complex singlet extension of the SM (CxSM) [19], the CP-conserving, i.e. real, 2-Higgs-Doublet Model (R2HDM) [18] and its CP-violating version C2HDM [18], the next-to-minimal 2HDM (N2HDM) [18], and the model 'CP in the Dark' [77,85]. New models can easily be added following the prescription in the manual of BSMPTv2 [19]. Also, consult the README.md-file on how to use our SymPy [119] as well as Maple [120] and Mathematica [121] interfaces for model implementation. In BSMPTv3, we furthermore added an exemplary model file for the SM.
- The code allows to calculate the loop-corrected trilinear Higgs self-couplings of the pre-implemented models and any model provided and implemented by the user, from the effective potential calculated in the code, at zero temperature.
- In BSMPTv2 the computation of the baryon asymmetry for the model C2HDM was implemented.

The new version v3 presented here surpasses the existing codes because of the following features:

- Our algorithms for tracing minima and calculating the bounce solutions are more stable than the ones in CosmoTransitions, in particular for complicated potentials with numerous field directions. It is for most scenarios faster than CosmoTransitions. Importantly, it finds phase transitions, where CosmoTransitions fails to identify them. We will discuss the comparison with CosmoTransitions in Sec. 4.
- BSMPTv3 allows to check for symmetry restoration at high temperature, and it can treat potentials with discrete symmetries and potentials with flat directions.
- In the derivation of the nucleation temperature, we do not only rely on the approximation applied in CosmoTransitions $S_3(T)/T \lesssim 140$, to get the nucleation temperature, but also derive it from the condition that the tunnelling decay rate per Hubble volume matches the Hubble rate.
- Unlike existing codes, BSMPTv3 calculates the nucleation, the percolation, the completion and the reheating temperature. The user can optionally define the values of the false vacuum fractions to be applied for the percolation and completion temperature, respectively.
- The user can select the characteristic temperature scale at which the thermal parameters relevant for the gravitational wave spectrum are calculated.
- Contrary to the above listed codes, BSMPTv3 computes the gravitational wave spectrum originating from bubble collisions and highly relativistic fluid shells, from sound waves and magneto-hydrodynamic turbulence.
- BSMPTv3 computes the related signal-to-noise ratio at LISA.

The code BSMPTv3 hence provides the whole chain from tracing the phases of extended Higgs sectors, calculating the bounce action, the transition rate, the strength of the phase transition to the gravitational wave spectrum (and it calculates also the baryon asymmetry in case of the C2HDM), in a self-contained framework applying on-shell renormalization in the effective potential.

Recently, an excellent overview has been published in [122], which reviews comprehensively the path from a particle physics model to GWs. The review also briefly comments on lattice methods. Lattice simulations allow to complete the incomplete perturbative approach to the study of EWPTs. They are computationally demanding, however, and not able to explore in detail many beyond-SM extensions. For lattice treatments of the effective potential cf. e.g. [123–126], for works on lattice simulations of gravitational waves, cf. e.g. [127]. An algorithm for the construction of an effective, dimensionally reduced, high-temperature field theory for generic models has been implemented in DRalgo [128], which allows to better describe infrared effects [129] that can only be treated properly by lattice simulations [130]. The approximation through leading-order perturbation theory, which is widely used, contains large theoretical uncertainties because it converges only slowly, as has been pointed out in [131–134]. In [122], also gauge-independent approaches are reviewed which address the problem of gauge dependence of the effective potential [135,136]. For recent developments, cf. e.g. [124,133,137–141]. The review introduces all relevant quantities, discusses related obstacles and open problems, reviews the state-of-the-art and related literature, and provides useful formula. While we restrict here to a minimal description for the introduction of our notation needed for the presentation of our code and its new features, without a discussion of pros and cons of different approaches,[6] we refer the reader for further background information to Ref. [122].

[4] The possibility and consequences of electroweak symmetry non-restoration were studied in e.g. [69,81,92–95].
[5] Vacuum trapping has been studied in e.g. [69,81,96].
[6] Where appropriate, we provide flags that allow the user to choose between approaches.

3. Program description

In the following, we describe how to install and use BSMPTv3 focusing on the new executables and describing the new structure.

3.1. Download and installation

The program was developed and tested on Arch Linux, OpenSuse 15.3 and macOS 13.2.1 with a range of compilers: GNU 7.5.0-13.2.1[7] and Clang 14.0.3.[8,9] The here presented version v3, as well as all previously released versions, can be obtained from:

https://github.com/phbasler/BSMPT.

The code is structured into the following directories:

example	example input and output files for all executables and models
include	header files
manual	manuals
profiles	Conan profiles
sh	Python files for converting input data files to required format
src	source files
standalone	stand-alone example codes that allow users to directly use selected algorithms
tests	input and source files used for the unit tests
tools	a SymPy [119] as well as a Maple [120] and a Mathematica [121] interface to calculate all necessary input needed to implement a new model, as well as configurations for the installation with CMake

The directory src contains the following:

src/prog	executable source code
src/models	implemented models and SM parameters
src/minimiser	minimisation routines
src/ThermalFunctions	thermal integrals
src/WallThickness	calculation of the wall thickness
src/Kfactors	calculation and interpolation of the thermal transport coefficients
src/baryo_calculations	VIA and FH approach to calculate the baryon asymmetry of the universe[10]
src/minimum_tracer	(multi-step) phase tracing and identification of coexisting phase pairs
src/bounce_solution	bounce solution and characteristic temperatures
src/gravitational_waves	derivation of GW spectrum parameters
src/transition_tracer	transition history evaluator that operates the classes minimum_tracer, bounce_solution, gravitational_waves for the new executables

BSMPTv3 requires a C and C++ compiler that supports the language standard 17, as well as an installation of CMake[11] and Conan.[12] The latter two can e.g. be installed with the Python package manager pip [151] through the command pip3 install cmake conan.

For a default installation of BSMPTv3, our Build.py script can be used. This script installs the necessary Conan profiles for the operating system, handles the dependencies and compiles BSMPT with its default settings. It is executed via the command (from within the main directory of BSMPTv3):

```
python3 Build.py
```

If the installation is successful, a new directory build is created and the following new executables are built in $BSMPT/build/[operating-system-specific-name]/bin:

MinimaTracer	Tracing of minima as function of the temperature (Sec. 3.7)
CalcTemps	Calculation of the bounce solution and characteristic temperatures for first-order phase transitions between pairs of coexisting phases (Sec. 3.8)
CalcGW	Calculation of the gravitational wave spectrum sourced by first-order phase transitions (Sec. 3.9)
PotPlotter	Visualization of multi-dimensional potential contours (Sec. 3.10)

By default, also the BSMPTv2-executables BSMPT, CalcCT, NLOVEV, TripleHiggsCouplingsNLO, Test, VEVEVO are built. To build the baryogenesis executables, CalculateEWBG, PlotEWBG_nL and PlotEWBG_vw, one needs to set CompileBaryo=True when installing BSMPT via our Setup.py script, as will be described below. Before doing so, we first comment on the dependencies that are used by Conan:

[7] https://gcc.gnu.org/.
[8] https://clang.llvm.org/.
[9] We furthermore continuously ensure that BSMPT compiles and passes all unit tests under the latest versions of macOS, Windows and Ubuntu as well as Ubuntu-20.09.
[10] We used the FH [142–145] and the VIA [146–149] approach to compute the baryon asymmetry of the universe in the C2HDM. Recently, it was argued, however, that the source term in the VIA method vanishes at leading order [150], which would have consequences for the derived baryon asymmetry in this method.
[11] https://cmake.org/.
[12] https://conan.io/.

- The library GSL [152] is required for its routines for numerical derivation, integration, interpolation as well as minimisation and its mathematical algorithms.
- Eigen3[13] is used for matrix- and vector-manipulations.
- nlohmann_json [153] is used for the option to supply input to the executables in the form of json-files as further described below.
- Catch [154] and benchmarks [155] are used for unit tests. If the unit tests should not be compiled, the option EnableTests=False must be set when using the detailed installation method via the Setup.py script, as further described below.
- Boost[14] is optional and only required for the calculations related to baryogenesis. In order to compile the baryogenesis calculation, the option CompileBaryo=True must be set in the detailed installation method, as described below.

In addition to GSL, at least one of the following minimisation libraries should be used. By default, both are installed:

- libcmaes [156] is a C++ implementation of the Covariance Matrix Adaptation Evolution Strategy algorithm. If an installation is not wanted, UseLibCMAES=False must be specified when using Setup.py for installation, as will be explained below.
- NLopt [157] uses the DIRECT_L [158] algorithm. If the user does not want to install NLopt, the option UseNLopt=False can be specified analogously.

We provide the script Setup.py which allows for a customized installation. It can take several optional arguments, e.g. all above listed options and more. All possible optional arguments can be viewed by running python3 Setup.py -h or python3 Setup.py -help.[15] A complete installation of BSMPTv3 using our Setup.py script looks like:

```
python3 Setup.py [optional arguments]
cmake --preset ${profile}
cmake --build --preset ${profile} -j
cmake --build --preset ${profile} -j -t doc
```

The -t doc uses doxygen[16] to create the documentation in the local build directory.[17] The ${profile} parameter depends on the operating system. After running Setup.py, cmake -list-presets gives a list of all selectable profiles.

When BSMPTv3 is successfully compiled (with option EnableTests=True), unit tests can be run by calling (in the main directory):

```
ctest --preset ${profile} -j
```

These tests should be extended if the user implements a new model.

3.2. Structure and description of the algorithms of BSMPTv3

The main objective of the code BSMPTv3 is the tracing of (multiple) phases as a function of the temperature and the calculation of the transition probability from the respective false to the true vacuum, the computation of the relevant thermal parameters and the determination of the gravitational wave spectrum from a FOPT. The solution is divided into three steps: (*i*) Construction of the loop-corrected effective potential (evaluated in the Landau gauge) including thermal masses and applying the on-shell renormalization scheme; tracing the minima of this potential and identification of pairs of coexisting phases. (*ii*) Determination of the bounce solution for each of the found pairs of coexisting phases; calculation of the tunnelling rate from the false to the true vacuum of the phase pair; computation of the critical, nucleation, percolation, and completion temperatures. (*iii*) For the found FOPT, computation of the gravitational wave spectrum based on the transition temperature (percolation temperature by default) and the bounce solution determined in step (*ii*). These three steps are performed in the corresponding three classes MinimumTracer, BounceSolution, and GravitationalWave and organized by a fourth class, TransitionTracer, cf. Fig. 1. The user interface to extracting the results is given by four executables, namely MinimaTracer.cpp (reports on all found minima as functions of the temperature), CalcTemps.cpp (gives out characteristic temperatures for all found coexisting phase pairs), CalcGW.cpp (reports on characteristic temperatures and GW parameters for all found coexisting phase pairs) and PotPlotter (calculates potential contours useful for visualization).

In the following four sections 3.3-3.6, we will describe the four classes with our applied solutions and the relevant formulae. In the four subsequent sections 3.7-3.10, the four executables will be explained together with the flags that can be applied. In this context, we will also describe various algorithms that can be chosen by the user through the flags. In Sec. 3.11 we collect functions that the user might want to use for specific computations. The last section 3.12 finally is devoted to the summary of the given out status codes and their explanation.

3.3. The class MinimumTracer

The computation of the effective potential in the on-shell renormalization scheme for an already implemented model or a new model implemented by the user was described in the BSMPT manuals of v1 and v2, to which we refer the user for details. Here we describe the newly implemented algorithm for the tracing of (possibly multiple) coexisting phases as function of the temperature.

Between a user-defined high temperature T_{high} and the low temperature $T_{\text{low}} = 0\,\text{GeV}$, MinimumTracer traces phases using found global minima at high and low temperature as well as the zero-temperature electroweak minimum as seed points. We start with the definitions of phases and phase transitions in Sec. 3.3.1 and then give in Sec. 3.3.2 details on the algorithm for tracing one phase. In Sec. 3.3.3 we describe how we identify symmetries of the potential and find the closest distinct phases in field space. Section 3.3.4 shows how BSMPTv3 deals with flat directions in potential space. More details on how BSMPTv3 traces landscapes with possibly multiple coexisting phases are given below in Sec. 3.7.1.

[13] http://eigen.tuxfamily.org/ and https://gitlab.com/libeigen/eigen.
[14] https://www.boost.org/.
[15] Note, that if a compiled version of BSMPT is distributed to other machines, which do not share the same or related CPUs, it is advisable to disable vectorization for its compilation. This can be done by setting UseVectorization=False.
[16] https://www.doxygen.nl/index.html.
[17] The documentation for BSMPT can also be found online at https://phbasler.github.io/BSMPT/documentation/.

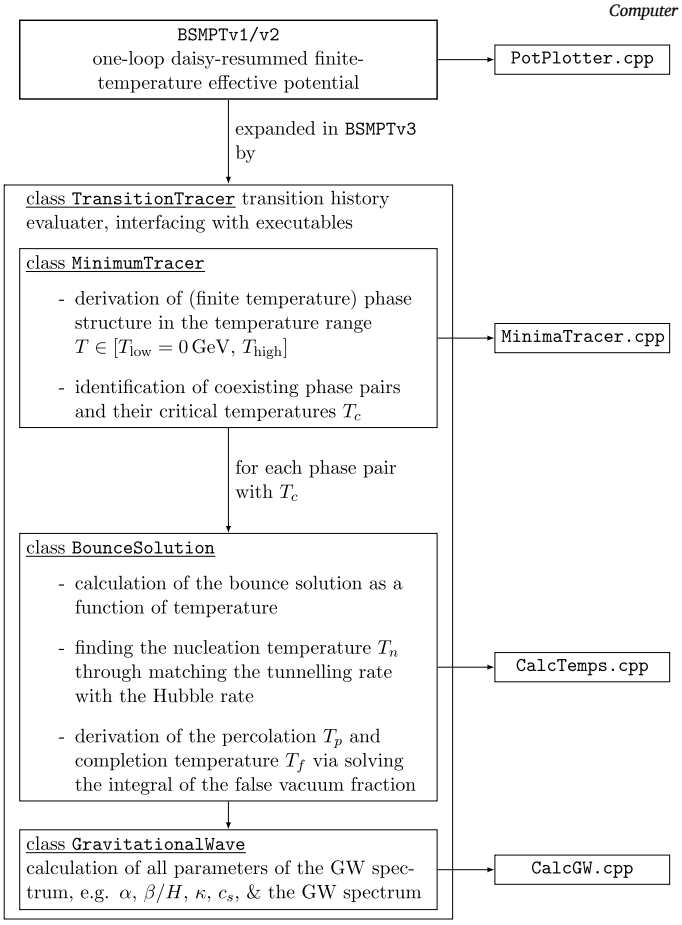

Fig. 1. Structure and dependencies of the algorithm of BSMPTv3. The four classes are compiled as libraries. The class TransitionTracer acts as a logic interface between the executables and the three subclasses that contain the steps of the calculation and, based on the results, reports on the transition history.

3.3.1. Phases, first and second order phase transitions

Multi-scalar Higgs potentials exhibit complicated cosmological histories accompanied by possibly a multitude of phase transitions between different vacuum states. For the sake of clarity, we have to define the meaning of the expressions *phase* as well as *first-order* and *second-order phase transition* as they are used in our code for the derivation of the gravitational waves related to a first-order phase transition. The *phase* of a multi-scalar potential is defined by the values of its temperature-dependent vacuum expection values of the complete set of scalar fields. Different phases differ in the scalar field directions in which they exhibit a non-zero VEV. With decreasing temperature during the evolution of the universe, the temperature-dependent effective potential changes and different minima, maxima, and saddle points at different locations in field space and with different potential values evolve. Starting from a global minimum at high temperature, with decreasing temperature at some moment a second minimum starts evolving, which may become degenerate with the existing global minimum at the critical temperature T_c, however, separated by a barrier, so that we then have a discontinuity in the VEVs of the two degenerate global minima. Finally, the second minimum becomes the global one and then, if the tunnelling rate is sufficiently large, a *first-order phase transition* from the false to the true vacuum takes place. In a *second-order phase transition*, on the other hand, we have a continuous change of the VEV as a function of the temperature. In BSMPTv3, we only consider GWs sourced by FOPTs.

3.3.2. Phase tracker

Our goal is to find the transition rate between two distinct phases as a function of the temperature T. Thus, before we do any calculation, it is of utmost importance to have an accurate description of the vacuum structure of a particular BSM model. Usually, models are too complex to allow for an analytical description of their vacuum so that we need to employ numerical methods to find the phases and track them across the whole temperature range.

The location of the global minimum in BSMPTv2 is searched for using algorithms of the libraries GSL, libcmaes or NLopt. These gradient-free methods only use potential values to locate the minimum, so that they are rather fast. The available precision provided in BSMPTv2 was considered sufficient in previous iterations. However, for the identification of the bounce solution in BSMPTv3, significantly higher precision is required, primarily as a result of the complexity of the boundary conditions. In BSMPTv3, we still use these gradient-free methods to find the seed points from where we start the tracing.

To find the minimum $\vec{\phi}$ of the potential we have to search for points with vanishing gradient, $\nabla V(\vec{\phi}) = \vec{0}$. The method that we settled for is the Newton–Raphson method which uses the gradient and the Hessian matrix to take an educated step in the right direction. To understand the core of the method let us Taylor expand the gradient around a point $\vec{\phi}$,

$$\nabla V(\vec{\phi} + \vec{\varepsilon}) = \nabla V(\vec{\phi}) + H(\vec{\phi})\vec{\varepsilon} + \mathcal{O}(\vec{\varepsilon}^2)\,, \tag{3.1}$$

where $H(\vec{\phi})$ is the Hessian matrix calculated at $\vec{\phi}$. Suppose that this small step takes us to the minimum of the potential, i.e. $\nabla V(\vec{\phi}+\vec{\varepsilon})=0$, then we can invert the equation to find the step $\vec{\varepsilon}$,

$$\vec{\varepsilon} = -H(\vec{\phi})^{-1}\nabla V(\vec{\phi})\,. \tag{3.2}$$

In our code, we start with an initial guess $\vec{\phi}_0$ provided by the gradient-free minimisers and take educated steps $\vec{\phi}_{i+1} = \vec{\phi}_i - H(\vec{\phi}_i)^{-1}\nabla V(\vec{\phi}_i)$ until the gradient vanishes. This method is the equivalent of locally approximating the potential with a multivariate second-degree polynomial and finding the minimum with a single iteration. Although each iteration is computationally costly, as one needs to numerically calculate the gradient and the Hessian and its inverse, the convergence is so fast that near the minimum only a few iterations are needed to find the minimum.

We then want to track the phases across the whole temperature range, so after finding the minimum for some temperature T we slightly change the temperature $T \to T + \delta T$ and rerun the algorithm starting at the minimum found at T. If the minimum is now a saddle point (which can also be found by the method) then we decrease δT. If the Hessian matrix is singular this method will not work because the Hessian matrix will have no inverse. This might be a problematic scenario because the Hessian matrix eigenvalues coincide with the masses of scalar particles and massless particles are a possibility. To circumvent this scenario we add a small constant to the diagonal elements of the Hessian, thereby shifting all eigenvalues by this constant value. This allows us to have zero, and even small negative eigenvalues to account for numerical errors, in the Hessian matrix without destroying the convergence.

This method uses gradients and Hessian matrices that, in our case, have to be calculated numerically. A useful trick that stabilises the numerical derivatives is to rescale the potential as

$$V(\vec{\phi}) \to \frac{V(\vec{\phi})}{1\ \text{GeV}^2 + T^2}\,. \tag{3.3}$$

Obviously, a minimum in the rescaled potential is also a minimum in the non-rescaled potential. The advantage comes from the fact that at high T the potential behaves as

$$\lim_{T\to\infty} V(\vec{\phi},T) \sim T^2\widetilde{V}(\vec{\phi}) + T^4 \times (\text{field-independent constants})\,, \tag{3.4}$$

where $\widetilde{V}(\vec{\phi})$ is the part of the potential proportional to T^2 and is T-independent.[18] The T^4 term is irrelevant for the derivatives, the other term scales as T^2 so that the rescaled potential becomes T-independent at high T. Because of this, it is much easier to choose a good step size for the numerical derivatives. We chose to rescale the potential with $1\ \text{GeV}^2 + T^2$ and not just T^2 in order not to run into $\frac{1}{0}$ at low T.

A short comparison with `CosmoTransitions` is in order. While we use the Newton-Raphson method to find the minimum, `CosmoTransitions` first uses a Newton-Raphson step combined with a gradient descent step in temperature from the previous temperature iteration to find a good approximation; next it uses the Nelder-Mead downhill simplex method [160] until it finds the minimum. While, as said above, our method is computationally more expensive, as we have to compute and invert the Hessian matrix, we found that it converges much faster than the Nelder-Mead simplex method, in particular if the temperature step is well-chosen.

3.3.3. Discrete symmetries

Some of the models may exhibit discrete $\mathbb{Z}_2$ symmetries in the scalar sector or $\mathbb{Z}_2$ subgroups of the gauge groups. As these symmetries increase the number of possible minima, it is important to know if two particular minima can be transformed from one to the other. By knowing the symmetries, `BSMPTv3` does not trace the same minimum twice which reduces the computational time. Another important issue is that, although minima which are related through symmetries have the same physics, they may have different transition rates to other minima. Let us consider a model with a symmetry transformation $\vec{\phi} \to \vec{\tilde{\phi}}$, and with a true vacuum $\vec{\phi}_t$ and a false vacuum $\vec{\phi}_f$ that cannot transform into each other or themselves applying the symmetry transformation. We hence have four distinct minima. Obviously, we have for the Euclidean action S_3 that $S_3(\vec{\phi}_f \to \vec{\phi}_t) = S_3(\vec{\tilde{\phi}}_f \to \vec{\tilde{\phi}}_t)$. But we also have other possibilities, $S_3(\vec{\phi}_f \to \vec{\tilde{\phi}}_t) = S_3(\vec{\tilde{\phi}}_f \to \vec{\phi}_t)$ etc., which might produce different transition rates. If this is not taken into account, the code might miss the transition with the lowest action. This is precisely what was noticed and discussed in Ref. [161] in the 2HDM and which alerted us for such scenarios.

The user does not need to provide the symmetries. `BSMPTv3` deals with this scenario by first computing the group G of all $\mathbb{Z}_2$ symmetries that the potential can have. The general group is given by the following direct product

$$G = \prod_i^n \mathbb{Z}_2^{(i)} \tag{3.5}$$

where $\mathbb{Z}_2^{(i)} = \{e, z^{(i)}\}$ is the symmetry group that affects the sign of the i-th component, i.e. e is the identity and $\{\phi_1,\cdots,\phi_i,\cdots,\phi_n)\} \overset{z^{(i)}}{\to} \{\phi_1,\cdots,-\phi_i,\cdots,\phi_n\}$. The order of the group G is 2^n where n is the dimension of the field space. As an example, we consider the 2HDM. The eight group generators of its symmetry group in the field basis $\{\omega_{\text{CB}}, \omega_1, \omega_2, \omega_{\text{CP}}\}^T$ are given in Table 1. The indices 'CB, 1, 2, CP' denote the charge-breaking, the two CP-even neutral and the CP-breaking VEV directions, respectively. In general, we denote VEV directions at arbitrary temperature by ω_i and at zero temperature by v_i. After generating the group elements, the code verifies which of the symmetries keeps the potential invariant and saves this information to be used later.

[18] There are two different approaches to implement the temperature-corrected masses in the effective potential, referred to as 'Arnold-Espinosa' [131] and 'Parwani' [159] approach. For details, cf. e.g. [55]. In `BSMPT`, the default option is the Arnold-Espinos approach, which consistently implements the thermal masses at one-loop level in the high-temperature expansion. The scaling with T^2 is found for the Arnold-Espinosa approach, for the Parwani approach it is $T^2 \log T^2$. The numerical advantage holds for both methods.

Table 1
2HDM group elements applied on the initial field configuration $\{-10, 5, -20, 0\}^T$ and the resulting measure $M(g_i\vec{\phi})$ in binary and decimal numbers. We can see that $\{10, 5, -20, 0\}^T$ is the field configuration mapped into the principal quadrant.

Group Element	Measure in binary	Measure in decimal
$\begin{pmatrix} 1&0&0&0\\ 0&1&0&0\\ 0&0&1&0\\ 0&0&0&1 \end{pmatrix}$	0101	5
$\begin{pmatrix} -1&0&0&0\\ 0&1&0&0\\ 0&0&1&0\\ 0&0&0&1 \end{pmatrix}$	1101	13
$\begin{pmatrix} 1&0&0&0\\ 0&-1&0&0\\ 0&0&-1&0\\ 0&0&0&1 \end{pmatrix}$	0011	3
$\begin{pmatrix} 1&0&0&0\\ 0&1&0&0\\ 0&0&1&0\\ 0&0&0&-1 \end{pmatrix}$	0101	5
$\begin{pmatrix} -1&0&0&0\\ 0&-1&0&0\\ 0&0&-1&0\\ 0&0&0&1 \end{pmatrix}$	1011	11
$\begin{pmatrix} -1&0&0&0\\ 0&1&0&0\\ 0&0&1&0\\ 0&0&0&-1 \end{pmatrix}$	1101	13
$\begin{pmatrix} 1&0&0&0\\ 0&-1&0&0\\ 0&0&-1&0\\ 0&0&0&-1 \end{pmatrix}$	0011	3
$\begin{pmatrix} -1&0&0&0\\ 0&-1&0&0\\ 0&0&-1&0\\ 0&0&0&-1 \end{pmatrix}$	1011	11

We also introduce the notion of 'principal quadrant'.[19] Its definition takes into account our preference for positive VEVs (which of course is an arbitrary choice) and makes sure, by comparing two elements, that we have all VEVs in the same quadrant so that we do not follow the same VEV twice. We apply the symmetries such that we get the largest number of positive VEVs in the upper components of the field vector. This means, given an arbitrary field configuration $\vec{\phi}$ we apply the group element g_i that maximizes the measure $M(g_i\vec{\phi})$ given by

$$M(g_i\vec{\phi}) = \left(\vec{\theta}(g_i\vec{\phi})\right)_2 = \sum_i^n 2^i \left\{\vec{\theta}(g_i\vec{\phi})\right\}_i , \tag{3.6}$$

where $\vec{\theta}(\vec{x}) \equiv \{\vec{\theta}(\vec{x})_i = \theta(x_i)\}$ is the vectorised Heaviside step function, and the subscript 2 indicates that we should interpret the components of the vector as a binary number. It is best to think of this measure as mapping the field space on binary numbers. Let us consider two field configurations $g_a\vec{\phi}$ and $g_b\vec{\phi}$ such that $g_a\vec{\phi} \neq g_b\vec{\phi}$. This means that the measures are different, i.e. $M(g_a\vec{\phi}) \neq M(g_b\vec{\phi})$, because they have different binary representations. With this we showed that given a field configuration $\vec{\phi}$ there is a single[20] $g_i\vec{\phi}$ that maximizes $M(g_i\vec{\phi})$. We choose the set of field configurations that maximize $M(g_i\vec{\phi})$ under the symmetries, to be the principal quadrant.

To give some context to this measure, we apply all group elements for an arbitrarily chosen 2HDM field configuration given by $\{-10, 5, -20, 0\}^T$, cf. Table 1. From the second and the sixth row of the table, we can conclude that there are two group elements that produce the same measure. This is not an issue, however, as both symmetries transform the initial field configuration into the same configuration $\{10, 5, -20, 0\}^T$.

The method has one caveat. Models with a spontaneously broken discrete symmetry give rise to domain walls, which are a topological defect [162–164]. If domain walls were to exist they would dominate the energy density of the universe at some late time [162,165,166] and be in contradiction with observation, which is also known as the domain wall problem. In this case, constraints would have to be placed on models that can lead to the formation of domain walls, such that the domain wall domination does not occur [167], or at least not until today.[21] In our code, we do not take into account the possible existence of different domains separated by domain walls. As an approximation, we only consider phase transitions with the shortest path between false and true vacuum. The users have to make sure themselves not to apply models with unphysical

[19] While depending on the number of VEVs connected through discrete symmetries, geometrically this is not necessarily a quadrant, for the sake of simplicity we still keep this expression.
[20] This is not a injective mapping, in particular if there are zeros in the components. In that case we can have two symmetries g_i and g_j that maximize the measure but then they are equal, i.e. $g_i\vec{\phi} = g_j\vec{\phi}$.
[21] For recent works on domain walls in the 2HDM, see [168–172].

domain walls, respectively, else be aware that the existence of domain walls is not taken into account by `BMSPTv3`. In case of explicitly (softly) broken discrete symmetries the vacuum configurations of the related minima have different energies, such that domain walls are unstable and the domain with the higher energy eventually decays into the lower energy configuration. Such decays can lead to gravitational waves [173]. The fact that the domain walls exist by some time, may furthermore influence the energy of the universe and hence also the cosmological history of the universe. Again such effects are not described by our code. In summary, while the impact of topological defects may play an interesting role in the dynamics of phase transitions and electroweak baryogenesis, this is beyond the present goal of our code and is left for future work.

3.3.4. Flat directions

Multi-dimensional scalar potentials can exhibit flat directions resulting in an effective sub-dimensional minimisation problem that is notoriously difficult to be dealt with numerically. In `BSMPTv3` we identify flat directions, i.e. in the one-dimensional case when the potential is invariant in one field direction ω_i with $\Delta\omega_i \gg \omega_i$,

$$V(\omega_i, \dots) = V(\omega_i + \Delta\omega_i, \dots), \tag{3.7}$$

or in the two-dimensional case when the potential is invariant in $\omega_i^2 + \omega_j^2$, $i \neq j$, with

$$V(\omega_i, \omega_j, \dots) = V(\omega_i + \Delta\omega_i, \omega_j + \Delta\omega_j, \dots) \quad \text{with} \quad \sum_{a\in\{i,j\}} \omega_a^2 = \sum_{a\in\{i,j\}} (\omega_a + \Delta\omega_a)^2, \tag{3.8}$$

and in the three-dimensional case, checking for invariance in $\omega_i^2 + \omega_j^2 + \omega_k^2$, $i \neq j \neq k$, $i \neq k$, analogously to the two-dimensional case above. In order to catch the largest possible flat dimension first, we check subsequently for three-dimensional, two-dimensional and one-dimensional flat directions. If an n-dimensional flat direction is encountered with $n \in \{1, 2, 3\}$, we set the last $(n-1)$ VEV directions in the model-specific `VevOrder` to zero and use the respective first one only to report on found phases and transitions.[22]

3.4. The class `BounceSolution`

In the following, we describe the newly implemented algorithm for the determination of the bounce solution, which is needed for the computation of the transition probability from a false to a true vacuum, the characteristic temperatures and the gravitational wave spectrum.

3.4.1. Bounce equation

Our starting point is the Lagrangian

$$\mathcal{L} = \frac{1}{2}\left(\partial_\mu \vec{\phi}\right)\left(\partial^\mu \vec{\phi}\right) - V(\vec{\phi}), \tag{3.9}$$

where $\vec{\phi}$ is the vector of scalar fields of some particular theory and $V(\vec{\phi})$ is the effective potential. As shown by Coleman [174] based on the WKB approximation developed by Banks, Bender and Wu in [175], the transition rate per unit volume of the false vacuum $\vec{\phi}_f$ into the true vacuum $\vec{\phi}_t$ is obtained by

$$\Gamma(\vec{\phi}_f \to \vec{\phi}_t) \equiv \Gamma = A(T)\, e^{-S_E}, \tag{3.10}$$

where S_E is the Euclidean action of the classical path given by

$$S_E(T) = \int d\tau d^3x \left[\frac{1}{2}\left(\partial_\mu \vec{\phi}\right)\left(\partial^\mu \vec{\phi}\right) + V(\vec{\phi})\right], \tag{3.11}$$

and $A(T)$ is a temperature-dependent prefactor that will be discussed shortly. At $T = 0$, the lowest Euclidean action is $O(4)$-symmetric [174], therefore, one can make the following change of variables $\rho = \sqrt{\tau^2 + \vec{x}^2}$ that simplifies the calculation of the action to

$$S_4(T) = 2\pi^2 \int_0^\infty d\rho\, \rho^3 \left[\frac{1}{2}\left(\frac{d\vec{\phi}}{d\rho}\right)^2 + V(\vec{\phi})\right]. \tag{3.12}$$

At finite T, the statistics of bosons is periodic in the imaginary time τ direction with period $\frac{1}{T}$. That allows us to combine all contributions into an $O(3)$-symmetric Euclidean action, with the imaginary time integration giving a factor $\frac{1}{T}$ [176], i.e. we have the replacement $S_4(T) \to \frac{S_3(T)}{T}$. Thus, we can make the change of variables $\rho = \sqrt{\sum_{i\leq 3} x_i^2}$, simplifying the action to

$$S_3(T) = 4\pi \int_0^\infty d\rho\, \rho^2 \left[\frac{1}{2}\left(\frac{d\vec{\phi}}{d\rho}\right)^2 + V(\vec{\phi})\right]. \tag{3.13}$$

The Euler-Lagrange equations are given by

$$\frac{d^2\vec{\phi}}{d\rho^2} + \frac{D-1}{\rho}\frac{d\vec{\phi}}{d\rho} = \nabla V(\vec{\phi}), \qquad \text{w/ the boundary conditions :} \qquad \vec{\phi}(\rho)\Big|_{\rho\to\infty} = \vec{\phi}_f, \qquad \frac{d\vec{\phi}}{d\rho}\Big|_{\rho=0} = 0, \tag{3.14}$$

[22] Furthermore, a message is printed on the screen if the corresponding `logginglevel` is enabled with `-logginglevel::mintracerdetailed=true`. More details on useful diagnosing output, managed by all implemented `logginglevels`, can be found in Sec. 3.7.

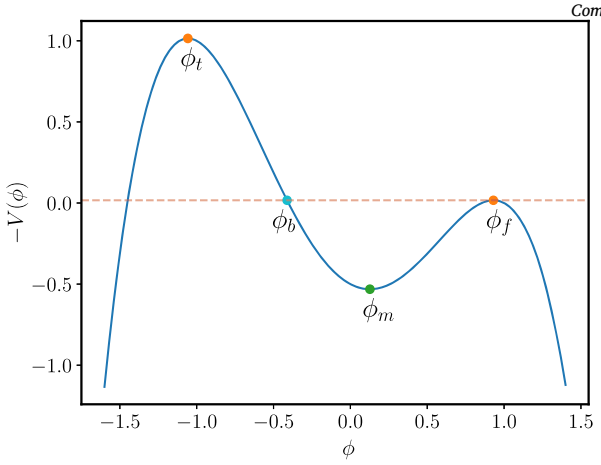

Fig. 2. Plot of a generic upturned potential. The orange points ϕ_f and ϕ_t are the false and true vacuum, respectively, the green point ϕ_m is the potential barrier, the cyan point ϕ_b is the point with the same potential value as the false vacuum, the dashed red line is the potential value of the false vacuum. (For interpretation of the colours in the figure(s), the reader is referred to the web version of this article.)

where $D = 4$ at zero temperature and $D = 3$ at finite temperature. The boundary conditions state that far away from the true vacuum bubble the false vacuum remains undisturbed, and that the transition happens at $\rho = 0$, which can be chosen without loss of generality. For $D = 3$, the prefactor $A(T)$ can be well approximated [176,177] by

$$A(T) \simeq T^4 \left(\frac{S_3}{2\pi T}\right)^{\frac{3}{2}} \quad \text{if} \quad T > 0\,. \tag{3.15}$$

We can cast the two expressions of the spherically symmetric action, S_3 and S_4, into a single expression ($D = 3, 4$)

$$S_D(T) = A_D \int_0^\infty d\rho\, \rho^{D-1} \left[\frac{1}{2}\left(\frac{d\vec{\phi}}{d\rho}\right)^2 + V(\vec{\phi})\right] = S_D^K(T) + S_D^V(T)\,, \tag{3.16}$$

where A_D denotes the area of the D-dimensional unitary sphere, and $S_D^K(T)$ and $S_D^V(T)$ are the contributions to the action coming from $\frac{d\vec{\phi}}{d\rho}$ and $V(\vec{\phi})$, respectively. We can draw a relation between these two contributions to the action [178]. To see that, let us assume that $\vec{\phi}(\rho)$ is a solution to the bounce equation. Making the ansatz $\vec{\phi}(\lambda\rho)$ for the solution, where λ is a real number, the action can be written as

$$S_D(T) = S_D^K(T)\lambda^{2-D} + S_D^V(T)\lambda^{-D}\,. \tag{3.17}$$

The action must be stationary at $\lambda = 1$ so that we must have

$$\left.\frac{dS_D(T)}{d\lambda}\right|_{\lambda=1} = (2-D)S_D^K(T) - DS_D^V(T) = 0 \implies S_D^K(T) = \frac{D}{2-D}S_D^V(T)\,, \tag{3.18}$$

which allows us to write the action as

$$\begin{aligned} S_D(T) &= S_D^K(T) + S_D^V(T) \\ &= \frac{2}{D}S_D^K(T) \qquad (3.19) \\ &= \frac{2}{2-D}S_D^V(T)\,. \qquad (3.20) \end{aligned}$$

This will be later used as a consistency check of the results: We compute $S_D^K(T)$ and $S_D^V(T)$, the kinetic and potential part of the action, respectively, and use Eqs. (3.19) and (3.20) to verify that they are consistent with the original expression for the action, Eq. (3.16). Let us note also that we assume that the finite-temperature transition rate is the dominant contribution for phase transitions taking place at finite temperature. We neglect zero-temperature contributions to the tunnelling rate.

The solution of Eq. (3.14) is highly non-trivial. Before diving into its detailed derivation, let us first discuss if the differential equation has a solution or not. In [174] it was shown that the one-dimensional version of the bounce action always has a solution. We shortly repeat this proof. If we take a look at Eq. (3.14), we can see that it resembles the equation of motion of a particle in an upturned potential that starts at rest in a position ϕ_0 at $\rho = 0$ and ends up at the false vacuum ϕ_f in the limit of $\rho \to \infty$. The solution of the bounce equation can be uniquely characterised by the starting position ϕ_0 so, to complete the proof, we must show that there is a starting position that makes the system end up at ϕ_f.

In the particle analogy, the variation of the energy as a function of ρ is given by [174]

$$\frac{d}{d\rho}\left[\frac{1}{2}\left(\frac{d\phi}{d\rho}\right)^2 - V(\phi)\right] = -\frac{D-1}{\rho}\left(\frac{d\phi}{d\rho}\right)^2 \leq 0\,, \tag{3.21}$$

which means that energy is lost due to the drag term. For this reason, if the starting position ϕ_0 is between ϕ_b and ϕ_f in Fig. 2, then it will never have enough energy to reach ϕ_f. We call this an undershoot. In the case of thin-walled situations, the particle stays close to ϕ_t across a large range of

ρ. In this case, we can neglect the drag term, as it is proportional to ρ^{-1}, making the particle go over ϕ_f without stopping. We call this an overshoot. Therefore, by continuity, between these two situations, there must exist a ρ_0 which solves the ODE, as to one side we overshoot and to the other we undershoot.

The bounce equation (3.14) can only be solved numerically, as will be described below, except for $\rho = 0$. Here an analytical approach is required, because of the $\frac{D-1}{\rho}\frac{d\vec{\phi}}{d\rho}$ term. This term has an $\infty \times 0$ indetermination. Another benefit of analytically integrating at $\rho = 0$ is that it allows for a quick integration over very thin-walled solutions, i.e. solutions that stay close to ϕ_t across a large range of ρ.

From now on, we use a different parametrisation for the equations of motion, similar to the one described in Refs. [17,179]. We parameterize the tunnelling path as

$$\vec{\phi}(\rho) \to \vec{\phi}(l(\rho))\,, \tag{3.22}$$

where we impose unitary velocity, i.e.

$$\left|\frac{d\vec{\phi}(l)}{dl}\right| = 1\,, \tag{3.23}$$

which allows us to interpret l as length along the tunnelling path. This parametrisation simplifies the Euler-Lagrange equation (3.14) into

$$\frac{d^2 l}{d\rho^2} + \frac{D-1}{\rho}\frac{dl}{d\rho} = \frac{dV(\vec{\phi})}{dl}\,, \tag{3.24}$$

with the boundary conditions

$$\left.\frac{dl}{d\rho}\right|_{\rho=0} = 0\,, \quad l(\rho=\infty) = l_f\,, \tag{3.25}$$

where l_f is the total length of the tunnelling path.

The analytical solutions are found by approximating the potential by a quadratic function and writing it as a function of the spline parameter l, with the starting position $l_0 \equiv l(\rho = 0)$ and the spline parameter of the true vacuum l_t. We made one further assumption, namely that the smallest bounce solution is monotonic in ρ. In the particle analogy this means that it never moves backwards, equivalent to $\frac{dl}{d\rho} \geq 0$. The solutions at $\rho = 0$ depend on D, and we are going to provide the solutions for the $D = \{3, 4\}$ cases specifically. We distinguish between the following solutions:

- **Solutions starting near the true minimum**
  In this scenario we start very close to the true vacuum at a position l_t. The potential is then approximated by $V(l) \approx \frac{1}{2}H(l - l_t)^2$, where $H \equiv \left.\frac{d^2V}{dl^2}\right|_{\rho=0}$. The solutions start at $l(\rho = 0) = l_0$ and are given by

$$l(\rho) = \begin{cases} l_t - \frac{(l_t - l_0)\sinh\left(\rho\sqrt{H}\right)}{\rho\sqrt{H}} & \text{for} \quad D = 3 \\ l_t - \frac{2(l_t - l_0)I_1\left(\rho\sqrt{H}\right)}{\rho\sqrt{H}} & \text{for} \quad D = 4 \end{cases}, \tag{3.26}$$

  where $\sinh(x)$ is the hyperbolic sine function and $I_1(x)$ is the modified Bessel function of the first kind.
- **Solution starting where $\mathbf{H > 0}$**
  In this scenario we still start near a local minimum but with a non-negligible potential gradient $G \equiv \left.\frac{dV}{dl}\right|_{\rho=0}$, which is taken to be positive to ensure the assumption that $\frac{dl}{d\rho} \geq 0$. Therefore, the potential is approximated by $V(l) \approx G(l - l_0) + \frac{1}{2}H(l - l_0)^2$ and the solutions are given by

$$l(\rho) = \begin{cases} l_0 - \frac{G}{H} + \frac{G\sinh\left(\rho\sqrt{H}\right)}{\rho H^{\frac{3}{2}}} & \text{for} \quad D = 3 \\ l_0 - \frac{G}{H} + \frac{2GI_1(\rho\sqrt{H})}{\rho H^{\frac{3}{2}}} & \text{for} \quad D = 4 \end{cases}. \tag{3.27}$$

- **Solution starting where $\mathbf{H < 0}$**
  In this scenario we start near the potential barrier with a non-zero gradient $G \equiv \left.\frac{dV}{dl}\right|_{\rho=0}$, which is taken to be positive to ensure the assumption that $\frac{dl}{d\rho} \geq 0$. The potential is approximated by $V(l) \approx G(l - l_0) + \frac{1}{2}H(l - l_0)^2$ and the solutions are given by

$$l(\rho) = \begin{cases} l_0 - \frac{G}{H} - \frac{G\sin\left(\rho\sqrt{-H}\right)}{\rho(-H)^{\frac{3}{2}}} & \text{for} \quad D = 3 \\ l_0 - \frac{G}{H} - \frac{2GJ_1(\rho\sqrt{-H})}{\rho(-H)^{\frac{3}{2}}} & \text{for} \quad D = 4 \end{cases}. \tag{3.28}$$

  The $J_1(x)$ is the Bessel function of the first kind.

There are two analytical solutions that can be used when $H > 0$, Eq. (3.26) and Eq. (3.27). To have a smooth transition between these two branches, we first calculate the branch switching point $l_{\text{threshold}}$ which minimizes the relative error on ρ between the two expressions. Secondly, given a starting point l_0, we compute both solutions and combine them in a logistic function weighted average based on the distance to $l_{\text{threshold}}$, such that the transition between the two branches is continuous.

3.4.2. Numerical solution of the bounce equation

The bounce equation that we need to solve to find the tunnelling rate has no analytical solution for a generic potential $V(\vec{\phi})$, so that we have to employ numerical methods to find an approximate solution, which we will sketch in the following.

The ordinary differential equation (ODE), presented in the last section, is difficult to solve. The main issue is that the boundary conditions are not applied at the same point in ρ and, since we are working with the inverted potential, i.e. with a potential with the opposite sign, the integration of the ODE is highly susceptible to small changes in $\vec{\phi}_0 \equiv \vec{\phi}(\rho = 0)$, which is exactly what we want to find. Once $\vec{\phi}_0$ is known, it is trivial to integrate the ODE. There is some bias for $\vec{\phi}_0$ to be around $\vec{\phi}_t$ but, apart from that, $\vec{\phi}_0$ lives in a space with the same number of dimensions as the number of fields that can acquire a VEV. From a computational point of view, this problem is very difficult to solve since, as mentioned above, small variations of the starting position $\vec{\phi}_0$ will produce very different solutions to the bounce equation. For this reason, trying to guess the initial position is very inefficient, requiring an alternative approach.

The approach of `CosmoTransitions` [17] is to start with a guess path, a straight line between $\vec{\phi}_t$ and $\vec{\phi}_f$, and solve Eq. (3.24), which is computationally feasible. Then one deforms the path such that

$$\frac{d^2\vec{\phi}}{dl^2}\left(\frac{dl}{d\rho}\right)^2 = \nabla_\perp V(\vec{\phi}), \tag{3.29}$$

where

$$\nabla_\perp V(\vec{\phi}) = \nabla V(\vec{\phi}) - \left(\nabla V(\vec{\phi}) \cdot \frac{d\vec{\phi}}{dl}\right)\frac{d\vec{\phi}}{dl}, \tag{3.30}$$

is fulfilled. This equation imposes that the curvature of the path matches the perpendicular forces originating from the potential. This is done by selecting points on the guess path and applying a small (rescaled) force to them,

$$\vec{N} = \frac{d^2\vec{\phi}}{d^2l}\left(\frac{dl}{d\rho}\right)^2 - \nabla_\perp V(\vec{\phi}), \tag{3.31}$$

until they converge and this produces a new, hopefully better, path. Then one goes back to Eq. (3.24), solves it, and deforms the path again. This process is repeated until convergence is achieved, i.e. $\vec{N} = 0$.

While there are numerous methods to numerically solve the problem (cf. e.g. the algorithm of the codes described Sec. 2 as well as [49] and references [28-36] therein), we chose in `BSMPTv3` an algorithm fulfilling our needs, that is very similar to the one used by `CosmoTransitions` described here above, but with a few differences. `CosmoTransitions` relies on B-splines to describe the tunnelling path, whereas we use cubic-splines with not-a-knot boundary conditions to describe it. This allows for a more general tunnelling path as B-splines have a finite resolution. During path deformation, however, we also use B-splines to remove slight numerical instabilities. The step size for the path deformation is calculated in the same way as in `CosmoTransitions`. i.e. we start with a small step size. If we are constantly deforming in the same direction we increase the step size; if the direction inverts we reduce the step size. For the computation of the relevant thermal quantities, it is necessary to have the Euclidean action S_3/T as a function of the temperature for a wide temperature range. For this reason, after solving the bounce equation for a given temperature T we solve the bounce equation for a temperature $T + \delta T$ by slightly warping the path from the solution previously found. This increases the reliability of the computation and considerably decreases the computational time.

To find the solution we apply bisection until the desired resolution is reached. Here, we initially perform the binary search on a linear scale but if a thin-walled solution is detected we switch to a log scale. Note, however, that the solution needs not be unique. Furthermore, for more than one field a solution does not always exist [180]. This does not mean that the false vacuum is stable, but rather that the decay rate must be computed differently [181–184].

After providing the one-dimensional solution for the bounce equation using the overshoot/undershoot method as described above, we deform the path with a force perpendicular to the path and proportional to $\vec{N}$, cf. Eq. (3.31). Since the normal force depends on the one-dimensional solution, it only makes sense to deform the path from the initial position at $\vec{\phi}_0 = \vec{\phi}(\rho = 0)$ up until $\vec{\phi}_f(\rho = \infty)$, so that the path from $\vec{\phi}_t$ to $\vec{\phi}_0$ is thrown away during each path deformation iteration. This can be problematic because we cannot guarantee that the new path can solve the bounce equation. If e.g. the new path is longer or has a steeper starting position, then it can dissipate more energy than the previous iteration, making it impossible to solve the one-dimensional bounce equation. For this reason, it is necessary to add path to the beginning of the current guess. We do that by using the spline to extrapolate the beginning of the path until we reach through this backwards propagation ('bp') a point $\vec{\phi}_{\rm bp}$ with $\frac{dV\left(\vec{\phi}(l)\right)}{dl}\Big|_{\vec{\phi}=\vec{\phi}_{\rm bp}} = 0$. This condition ensures that, since $-V(\vec{\phi}_{\rm bp}) > -V(\phi_f)$, the one-dimensional bounce equation has a solution for the same reasons presented above.

3.4.3. Characteristic temperature scales

The effective potential and hence also the vacuum decay rates are temperature-dependent. Depending on the temperature, the transition rate may eventually become large enough to make the universe go from one to the other vacuum with the cosmological FOPT taking place in a certain temperature interval. It is hence useful to consider certain characteristic moments of the transition as the decay rate grows, which, instead of time, is done using the temperature of the universe. We will present here these characteristic temperatures and how they are calculated in `BSMPTv3`. They will be used in the calculation of the spectrum of the gravitational waves presented below.

- **Critical Temperature** - T_c - This is the temperature, where the effective potential has two degenerate minima and, consequently, the transition from the false vacuum to the true vacuum may start via quantum tunnelling.
- **Nucleation Temperature** - T_n - This is the temperature at which the tunnelling decay rate per Hubble volume matches the Hubble rate,

$$\frac{\Gamma(T_n)}{H^4(T_n)} = 1, \tag{3.32}$$

which can be further approximated as (cf. e.g. [17])

$$\frac{S_3(T_n)}{T_n} \sim 140\,. \tag{3.33}$$

We note that BSMPTv3 calculates and outputs the nucleation temperature calculated via Eq. (3.32) as well as Eq. (3.33) in order to compare to e.g. CosmoTransitions which uses this approximation.

– **Percolation Temperature** - T_p - This is the temperature at which at least 29% of the false vacuum has tunnelled into the true vacuum or, equivalently, the probability of finding a point still in the false vacuum is 71 % [185–187]. This condition imposes that at the percolation temperature there is a large connected structure of true vacuum that spans the whole universe, and that is stable and cannot collapse back to the false vacuum. This large structure is known as the *percolating cluster*. The probability of finding a point in the false vacuum is given by

$$P_p = P(T=T_p) = e^{-I(T=T_p)} = \epsilon_p, \qquad I(T) = \frac{4\pi v_w^3}{3}\int_T^{T_c}\frac{\Gamma(T')dT'}{T'^4 H(T')}\left(\int_T^{T'}\frac{d\tilde{T}}{H(\tilde{T})}\right)^3, \tag{3.34}$$

where v_w denotes the wall velocity. To find the percolation temperature one has to solve $I(T_p) = 0.34$ or, equivalently, $P(T_p) = 0.71$. This is the default set in BSMPTv3. The user has the possibility, however, to set ϵ_p through the input.

– **Completion Temperature** - T_f - This is the temperature, at which the transition completes, no finite regions in the universe in the false vacuum are left. It is obtained from demanding the probability of finding a false vacuum to be

$$P_f = P(T=T_f) = \epsilon_f\,, \tag{3.35}$$

with the default setting $\epsilon_f = 0.01$. Again, the user has the possibility to choose a different value of ϵ_f through the input.

3.5. The class GravitationalWave

In this class both the gravitational wave spectrum as well as the signal-to-noise ratio at the Laser Interferometer Space Antenna (LISA) [28,188,189] are calculated as will be described in the following.

3.5.1. Gravitational wave spectrum

Thermal parameters, like the transition temperature, the transition strength, the characteristic length scale, the bubble wall velocity, not only characterise FOPTs, they are also relevant for the gravitational wave predictions. Thermal parameters are evaluated, however, only at a single temperature. Gravitational waves on the other hand are produced during the whole phase transition. The question is hence, which temperature to apply when evaluating the thermal parameters used in gravitational wave predictions. In the following, we generically call this transition temperature and denote it by T_*. A common choice for T_* is the nucleation temperature T_n. Since GWs originate from bubble collisions and sound shells and the following turbulence, it might be more appropriate to chose the percolation temperature T_p. Another choice might be the completion temperature. In a plasma reheating to a homogeneous temperature $T_{\rm reh}$ after the completion of the transition, the redshift of the GWs should be calculated from $T_{\rm reh}$, see Eq. (3.55) below, instead from T_* [190], but not the characteristic length scale and the energy available for the production of gravitational waves, as they take place before reheating. In the following, we will give the formulae for the relevant thermal parameters of the gravitational waves at the transition temperature T_*. In BSMPTv3 the default setting is

$$\text{Default in BSMPTv3}: T_* = T_p\,. \tag{3.36}$$

The user can also choose other settings using the input flags.

The second key parameter is the strength of the phase transition, which is measured by the parameter α. It can be, and most commonly is, defined by the trace anomaly [127,191] as

$$\alpha = \frac{1}{\rho_\gamma(T_*)}\left[V(\vec{\phi}_f) - V(\vec{\phi}_t) - \frac{T}{4}\left(\frac{\partial V(\vec{\phi}_f)}{\partial T} - \frac{\partial V(\vec{\phi}_t)}{\partial T}\right)\right]_{T=T_*}, \tag{3.37}$$

where $\rho_\gamma(T_*)$ is the energy density of a radiation dominated universe at T_*, written as a function of the effective number of relativistic degrees of freedom $g(T)$, which we derive as a function of the temperature in Appendix C. The ρ_γ is given by

$$\rho_\gamma(T) = g(T)\frac{\pi^2}{30}T^4\,. \tag{3.38}$$

The parameter α measures the energy budget available for the production of GWs. A common classification is that $\alpha \sim \mathcal{O}(0.01)$ corresponds to weak transitions, $\alpha \sim \mathcal{O}(0.1)$ to intermediate transitions, and $\alpha \gtrsim \mathcal{O}(1)$ to strong transitions. Strong phase transitions not only may source preferably GWs through bubble collisions, but may also lead to an early onset of turbulence [26,127,191,192], which we account for by introducing the GW source lifetime factor Υ, see Eq. (3.77) below. Note, that some studies use in the nominator of the right-hand side of Eq. (3.37) the latent heat released during the transition, which does not have the factor 1/4 in the second term. The definition used here, has been shown to describe the energy budget better, however, [193].

We take the occasion to comment on the notion of the strength of the phase transition. One of the three Sakharov conditions [13] for successful electroweak baryogenesis is a strong first-order EWPT. It is quantified by the sphaleron suppression criterion which classifies a PT as of strong first-order if the ratio ξ_c of the critical VEV v_c and the critical temperature T_c is larger than one [7,194],

$$\xi_c = \frac{v_c}{T_c} > 1\,. \tag{3.39}$$

Here v_c is the vacuum expectation value at the critical temperature T_c taking into account only the doublet VEV values. Non-zero singlet VEVs in models where they are available, are not included here. There is hence some ambiguity in the definition of the strength of the PT, so that it has to be made clear, where necessary, which definition is used. Note, also that a value of $\xi_c > 1$ does not guarantee that an SFOPT actually takes place.

The universe could also be trapped in the wrong vacuum, cf. e.g. [69,81,96]. This can only be decided by applying the criterion for the nucleation temperature, Eq. (3.32).

The third important thermal parameter is the inverse duration of the phase transition in Hubble units, denoted as β/H, and defined as (cf. e.g. [192])

$$\frac{\beta}{H_*} = T_* \left.\frac{d}{dT}\left(\frac{S_3(T)}{T}\right)\right|_{T_*} , \tag{3.40}$$

with H_* being the Hubble rate at the transition temperature T_*, $H_* = H(T = T_*)$.

The Hubble rate as a function of temperature is derived taking into account contributions from the radiation energy density ρ_γ, as well as from the difference in the vacuum energy between the false and the true vacuum, $\Delta V = V_{\text{false}} - V_{\text{true}}$, cf. [195–197],

$$H^2(T) = \frac{1}{3\widetilde{M}_{\text{Pl}}^2}\left(\rho_\gamma(T) + \Delta V(T)\right) = \frac{1}{3\widetilde{M}_{\text{Pl}}^2}\left(\frac{g(T)\pi^2}{30}T^4 + \Delta V(T)\right) , \tag{3.41}$$

where $\widetilde{M}_{Pl} \approx 2.4 \cdot 10^{18}$ GeV is the reduced Planck mass. The inverse time scale β/H is obtained from a linear approximation of the action in time, i.e. $S_3(t)/T(t) \approx S_3(t_*)/T(t_*) - \beta(t - t_*)$, assuming an adiabatic expansion of the universe with $dT/dt = -T\,H(T)$ [122], which leads to an additional factor $H_* T_*$. This expansion allows us to write the tunnelling rate as

$$\Gamma \approx e^{-\frac{S_3(t_*)}{T(t_*)} + \beta(t - t_*)} = e^{-\frac{S_3(T_*)}{T_*} - \frac{\beta}{H_* T_*}(T - T_*)} . \tag{3.42}$$

Although there is no physical reason to impose any lower bound on β/H_*, it has been argued in Refs. [122,198,199] that $\beta/H_* < 1$ would constitute a GW wavelength which is larger than the Hubble-horizon and would lead to difficulties with causality bounds on the amplitude [122,200]. We therefore only consider GW signals with $\beta/H_* \geq 1$ to be realistic. Furthermore, within our internal testing we even found GWs point with negative β/H_* which are not necessarily a mistake. These points might have an action that plateaus around 140 and the percolation temperature is only reached when the action is increasing again as the temperature lowers. For these cases, we still consider that the universe transitions into a different phase, but do not compute the gravitational waves spectrum. In such an instance, the characteristic time scale of the transition would have to be determined differently, which is beyond the current scope of the code.

The fourth parameter that determines the GW spectrum is the bubble wall velocity v_w. This parameter is extremely complicated to determine. The bubble walls start at rest and accelerates due to the difference of pressure between the phases, so that the wall velocity is a time-dependent quantity. The wall velocity is subject to a lot of ongoing activity and (also controversial) discussions.[23] We therefore treat the (terminal) wall velocity as input parameter. If it is not given by the user it is by default set to

$$\text{default wall velocity: } v_w = 0.95 . \tag{3.43}$$

Furthermore, the user can choose to use the approximate expression (α and ρ_γ evaluated at T_*) [202,203]

$$v_w \simeq \begin{cases} \sqrt{\frac{\Delta V}{\alpha\rho_\gamma}} & \text{if} \quad \sqrt{\frac{\Delta V}{\alpha\rho_\gamma}} < v_{\text{CJ}} , \\ 1 & \text{if} \quad \sqrt{\frac{\Delta V}{\alpha\rho_\gamma}} > v_{\text{CJ}} , \end{cases} \tag{3.44}$$

or the formula given in [201],

$$v_w = \left(\left|\frac{3\alpha + \Psi - 1}{2\left(2 - 3\Psi + \Psi^3\right)}\right|^{\frac{p}{2}} + \left|v_{\text{CJ}}\left(1 - a\frac{(1-\Psi)^b}{\alpha}\right)\right|^{\frac{p}{2}}\right)^{\frac{1}{p}} , \tag{3.45}$$

where $a = 0.2233$, $b = 1.704$, $p = -3.433$ are numerically fitted values, $\Psi = \omega_t/\omega_f$ is the ratio of enthalpies $\omega_i = -T\frac{dV(\vec{\phi}_i)}{dT}$ at the transition temperature T_* and v_{CJ} is the Chapman-Jouguet velocity, for general sound speeds c_s defined as [193]

$$v_{\text{CJ}} = \frac{1 + \sqrt{3\alpha\left(1 - c_{s,\text{f}}^2 + 3c_{s,\text{f}}^2\alpha\right)}}{1/c_{s,\text{f}} + 3c_{s,\text{f}}\alpha} , \tag{3.46}$$

where $c_{s,\text{f}}$ denotes the sound speed in the false vacuum. The sound speeds in the true and false vacuum, respectively, are calculated as [204]

$$c_{s,\text{t}}^2 = \frac{1}{T_*}\frac{V'(\vec{\omega}_\text{t}, T_*)}{V''(\vec{\omega}_\text{t}, T_*)} , \qquad c_{s,\text{f}}^2 = \frac{1}{T_*}\frac{V'(\vec{\omega}_\text{f}, T_*)}{V''(\vec{\omega}_\text{f}, T_*)} \tag{3.47}$$

where the prime denotes the partial derivative with respect to the temperature. In the derivation of both expressions for the velocity, the authors assumed local thermal equilibrium, and for the result (3.44) a constant temperature across the bubble was assumed. As argued by the authors of [201], their result can be interpreted as an upper bound on the wall velocity, as out-of-equilibrium effects always slow down the wall velocity compared to the equilibrium case. Alternatively, the user can calculate the bubble wall velocity with the recently published code `WallGo` [205].

The primordial GW signals produced in such violent out-of-equilibrium cosmological processes as given by the FOPTs, are redshifted by the cosmological expansion and look today like a cosmic gravitational stochastic background. The corresponding power spectrum [206–210] of the GW is given by

[23] For a recent summary of the discussion, cf. [201], which provides a model-independent determination of bubble wall velocities in local thermal equilibrium.

$$h^2\Omega_{\rm GW}(f) \equiv \frac{h^2}{\rho_c}\frac{\partial\rho_{\rm GW}}{\partial\log f}\,, \tag{3.48}$$

where ρ_c is the critical energy density today and $h = 0.674 \pm 0.005$ is the reduced Hubble constant [211]. It can be split into three contributions,

$$h^2\Omega_{\rm GW}(f) = h^2\Omega_{\rm coll}(f) + h^2\Omega_{\rm sw}(f) + h^2\Omega_{\rm turb}(f)\,. \tag{3.49}$$

In our analysis we consider GWs originating from the collision of bubbles and highly relativistic fluid shells (coll), as well as from sound/shock waves (sw) and from magnetohydrodynamic turbulence (turb) [28,212] which are generated by breaking the spherical symmetry through the process of rapid expansion of the bubble wall in, and especially through its interaction with, the surrounding plasma in the early universe. For non-runaway bubbles with $\alpha < 1$, the shock wave is the contribution that dominates the GW spectrum [28].

We implement the spectra of [212] for gravitational waves sourced by first-order phase transitions. The spectrum for gravitational waves sourced by the collision of bubbles and by highly relativistic fluid shells, is modelled by a broken power law [212] as

$$\Omega_{\rm coll}(f) = \Omega_b^{\rm coll}\left(\frac{f}{f_b^{\rm coll}}\right)^{n_1}\left[\frac{1}{2}+\frac{1}{2}\left(\frac{f}{f_b^{\rm coll}}\right)^{a_1}\right]^{\frac{n_2-n_1}{a_1}}\,, \tag{3.50}$$

with $n_1 = 2.4$, $n_2 = -2.4$, $a_1 = 1.2$ and the amplitude and characteristic frequency given by [213,212]

$$\Omega_b^{\rm coll} \simeq 0.05\, F_{\rm GW,0}\, K_{\rm coll}^2\left(\frac{\beta}{H(T_*)}\right)^{-2}\,, \tag{3.51}$$

$$f_b^{\rm coll} \simeq 0.11\, H_{*,0}\frac{\beta}{H(T_*)}\,. \tag{3.52}$$

The redshift of the Hubble rate, $H_{*,0}$, and the redshift of the fractional energy density $K_{\rm coll}$, $F_{\rm GW,0}$, are expressed as [212]

$$H_{*,0} = 1.65\times10^{-5}\,{\rm Hz}\left(\frac{g_*}{100}\right)^{1/6}\left(\frac{T_{\rm reh}}{100\,{\rm GeV}}\right)\,, \tag{3.53}$$

$$h^2\, F_{\rm GW,0} = 1.64\times10^{-5}\left(\frac{100}{g_*}\right)^{1/3}\,, \tag{3.54}$$

with the *reheating* temperature $T_{\rm reh} \geq T_*$ approximated by

$$T_{\rm reh} = \begin{cases} T_* & ,\, \alpha(T_*) < 1 \\ T_*\left[1+\alpha(T_*)\right]^{1/4} & ,\, \text{else} \end{cases}\,, \tag{3.55}$$

assuming that the universe enters radiation domination almost instantaneously, cf. [197]. Note, that this simplified prescription is only valid for large enough bubble wall velocities in the case of strong enough phase transitions, cf. [122] and references within. We therefore print a warning if for $\alpha(T_*) > 1$, $v_w < v_{\rm CJ}$, with $v_{\rm CJ}$ as defined in Eq. (3.46). In contrast to [212], we introduce the model-dependent efficiency factor $\kappa_{\rm coll}$ of [214], as also used in [197], in the definition of the fractional energy density, $K_{\rm coll}$, of the collision GW source

$$K_{\rm coll} = \frac{\kappa_{\rm coll}\,\alpha}{1+\alpha}\,. \tag{3.56}$$

The efficiency factor $\kappa_{\rm coll}$ for bubble collisions is defined as the fraction of the vacuum energy that is stored in the bubble walls. We implement the updated prediction [214,215,213,195] of

$$\kappa_{\rm coll} = \left(1-\frac{\alpha_\infty}{\alpha}\right)\left(1-\frac{1}{\gamma_{\rm eq}^n}\right)\frac{R_{\rm eq}}{R_*}\frac{\gamma_*}{\gamma_{\rm eq}}\,, \tag{3.57}$$

where α_∞ defines the weakest strength of the phase transition for which Eq. (3.63) (see below) is valid if the next-to-leading order friction contribution $P_{1\to N}$ is neglected [214,215], and it is given by

$$\alpha_\infty = \frac{P_{1\to1}}{\rho_\gamma}\,, \tag{3.58}$$

where ρ_γ is the energy density given by Eq. (3.38) and $P_{1\to1}$ is the leading-order friction given below in Eq. (3.66). The Lorentz factor γ_* in the absence of plasma friction at the moment of collisions is derived from

$$\gamma_* = \min(\gamma_{\rm eq}, \gamma_{\rm run-away})\,, \tag{3.59}$$

with [216]

$$\gamma_{\rm run-away} = R_*/(3R_0) \quad \text{and} \quad R_{\rm eq} = 3R_0\gamma_{\rm eq}\,. \tag{3.60}$$

This definition takes into account whether the bubbles were still accelerating at collision or if they reached their terminal velocity. The initial bubble radius R_0 [195] is given by

$$R_0 = \left[\frac{3S_3}{8\pi\Delta V}\right]^{\frac{1}{3}}\,, \tag{3.61}$$

and the average bubble radius at the transition temperature R_* [217–220,195,197,221] is given by

$$R_* = \left[T_*^3 \int_{T_*}^{T_c} \frac{dT'}{T'^4} \frac{\Gamma(T')}{H(T')} \mathrm{e}^{-I(T')} \right]^{-1/3} . \tag{3.62}$$

The above derivation of the collision efficiency factor is valid in the regime where the bubble wall is accelerated by the pressure difference

$$\Delta P = \Delta V - P_{1\to 1} - P_{1\to N}^{(n)} \tag{3.63}$$

between vacuum pressure ΔV and the plasma friction terms, $P_{1\to 1}$ and $P_{1\to N}^{(n)}$. The leading-order pressure contribution [222] is given by

$$P_{1\to 1} \simeq \frac{1}{24} \Delta m^2 T_*^2 , \tag{3.64}$$

where

$$\Delta m^2 = \sum_i k_i c_i (m_{i,\mathrm{t}}^2 - m_{i,\mathrm{f}}^2) \tag{3.65}$$

with $c_i = 1\,(1/2)$ for bosons (fermions) and k_i denoting the internal number of degrees of freedom. The masses of the particles i in the true and the false vacuum are denoted by $m_{i,\mathrm{t}}$ and $m_{i,\mathrm{f}}$, respectively. For the next-to-leading order (NLO) pressure contribution there are two conflicting results [223,214,216,224] that have different scalings with the Lorentz γ and will, in general, produce a different terminal Lorentz factor γ_{eq}. To the best of our knowledge, the correct result is an open question so that we include both results in our implementation. The NLO pressure [223,214,216] result with linear γ-scaling is given by

$$P_{1\to N}^{(1)} \simeq \gamma \sum_i g_i^2 \Delta m_i T_*^3 , \tag{3.66}$$

where the sum runs only over the gauge bosons, g_i is the gauge coupling and Δm_i is the difference in the masses of the gauge bosons in the true vacuum and the false vacuum, respectively. The NLO pressure [224] result with the γ^2-scaling is given by

$$P_{1\to N}^{(2)} \simeq \gamma^2 \sum_i k_i g_i^2 T_*^4 . \tag{3.67}$$

The bubble wall accelerates driven by the energy difference until it reaches at equilibrium pressure $\Delta P = 0$ a terminal velocity with a Lorentz γ_{eq}, which in general is given by [215,195]

$$\gamma_{\mathrm{eq}} = \sqrt[n]{\frac{\Delta V - P_{1\to 1}}{P_{1\to N}^{(n)}/\gamma^n}} , \tag{3.68}$$

where (n) denotes the $\gamma^{(n)}$-scaling chosen for the NLO pressure contribution.

We set κ_{coll} as defined in Eq. (3.57) to zero if either $\alpha < \alpha_\infty$, or if $\gamma_{\mathrm{eq}} < 1$. The former allows us to deal with supercooled and non-supercooled phase transitions simultaneously, the latter excludes situations with an unphysical Lorentz factor γ. The spectrum for sound waves and for magnetohydrodynamic turbulence is fitted with a double broken power law template [212],

$$\Omega_{\mathrm{GW}}^{\mathrm{DBPL}}(f) = \Omega_{\mathrm{int}} \times S(f) = \Omega_2 \times S_2(f) , \tag{3.69}$$

with the shape function

$$S(f) = N \left(\frac{f}{f_1}\right)^{n_1} \left[1 + \left(\frac{f}{f_1}\right)^{a_1}\right]^{\frac{-n_1+n_2}{a_1}} \left[1 + \left(\frac{f}{f_2}\right)^{a_2}\right]^{\frac{-n_2+n_3}{a_2}} , \tag{3.70}$$

and $\{n_1, n_2, n_3, a_1, a_2\} = \{3, 1, -3, 2, 4\}$ for sound waves and $\left\{3, 1, -\frac{8}{3}, 4, 2.15\right\}$ for turbulence, respectively, and $S_2(f) = S(f)/S(f_2)$. The normalization N of the shape function is then determined via the requirement $S_2(f_2) = 1$. The characteristic frequency breaks $f_{1,2}$ of the sound wave spectrum are

$$f_1^{\mathrm{sw}} \simeq 0.2 H_{*,0} \left(H_* R_*\right)^{-1} , \tag{3.71}$$

$$f_2^{\mathrm{sw}} \simeq 0.5 H_{*,0} \Delta_w^{-1} (H_* R_*)^{-1} , \tag{3.72}$$

with $\Delta_w = \xi_{\mathrm{shell}}/\max(v_w, c_{s,\mathrm{f}})$ and the fluid shell thickness estimated as $\xi_{\mathrm{shell}} = \xi_{\mathrm{front}} - \xi_{\mathrm{rear}}$ with [212,225]

$$\xi_{\mathrm{front}} = \begin{cases} \xi_{\mathrm{shock}} , & \text{for } v_w < v_{\mathrm{CJ}} \\ v_w , & \text{for } v_w \geq v_{\mathrm{CJ}} \end{cases} , \qquad \xi_{\mathrm{rear}} = \begin{cases} v_w , & \text{for } v_w < c_{s,\mathrm{t}} \\ c_{s,\mathrm{t}} , & \text{for } v_w \geq c_{s,\mathrm{t}} \end{cases} . \tag{3.73}$$

We determine the shock velocity ξ_{shock} from the fluid velocity profile that is determined by solving the hydrodynamics equations using the method of [193,204].

For sound waves, the integrated amplitude Ω_{int} is derived as [212]

$$\Omega_{\mathrm{int}}^{\mathrm{sw}} = F_{\mathrm{GW},0} A_{\mathrm{sw}} K_{\mathrm{sw}}^2 \left(H_* R_*\right) \Upsilon , \tag{3.74}$$

where $A_{\mathrm{sw}} = 0.11$ and with the kinetic energy fraction

$$K_{\mathrm{sw}} = \frac{0.6\, \kappa_{\mathrm{sw}}\, \alpha}{1 + \alpha} . \tag{3.75}$$

We calculate the efficiency factor $\kappa_{\rm sw}$ from $\kappa_{\rm sw}^{\mu\nu}$ which we obtain with the template model introduced by [193,204],

$$\kappa_{\rm sw} = \frac{\alpha_{\rm eff}}{\alpha}\kappa_{\rm sw}^{\mu\nu}\,, \tag{3.76}$$

by a rescaling with the effective strength $\alpha_{\rm eff} \equiv \alpha(1-\kappa_{\rm coll})$ to account for supercooled transitions, where a large portion of the energy goes into collisions. For non-supercooled transitions we have that $\alpha \simeq \alpha_{\rm eff}$ as the collision efficiency factor is small, i.e. $\kappa_{\rm coll} \ll 1$.

The suppression factor Υ arising from the finite lifetime $\tau_{\rm sw}$ of sound waves, is estimated by [127,192,214,226–228]

$$\Upsilon = 1 - \frac{1}{\sqrt{1+2H_*\tau_{\rm sw}}}, \quad \text{where} \quad H_*\tau_{\rm sw} = \min\left[\frac{2H_*R_*}{\sqrt{3K_{\rm sw}}}, 1\right]. \tag{3.77}$$

The sound wave amplitude Ω_2 at f_2 is expressed in terms of the integrated amplitude $\Omega_{\rm int}$ as

$$\Omega_2 = \frac{1}{\pi}\left(\sqrt{2} + \frac{2f_2/f_1}{1+f_2^2/f_1^2}\right)\Omega_{\rm int}\,. \tag{3.78}$$

Magnetohydrodynamic (MHD) turbulence is characterized by

$$f_1 = \frac{\sqrt{3\Omega_s}}{2\mathcal{N}} H_{*,0}\left(H_*R_*\right)^{-1}\,, \tag{3.79}$$

$$f_2 \simeq 2.2 H_{*,0}\left(H_*R_*\right)^{-1}\,, \tag{3.80}$$

$$\Omega_2 = F_{\rm GW,0}\, A_{\rm MHD}\, \Omega_s^2\, \left(H_*R_*\right)^2\,, \tag{3.81}$$

with $A_{\rm MHD} = 4.37\times10^{-3}$ and $\Omega_s = \kappa_{\rm turb}K_{\rm sw}$, where $\kappa_{\rm turb}$ represents the fraction of the overall kinetic energy in the bulk motion that is converted to magnetohydrodynamic turbulence, and $\mathcal{N} \simeq 2$. The turbulence efficiency factor $\kappa_{\rm turb}$ is set to

$$\kappa_{\rm turb} = \epsilon\,\kappa_{\rm sw}\,, \tag{3.82}$$

with the efficiency factor ϵ that can be set by the user to a value between 0 and 1 or to the upper bound given [122] by

$$\epsilon = \sqrt{1-\Upsilon}\,. \tag{3.83}$$

3.5.2. Signal-to-noise ratio at LISA

The stochastic gravitational wave signal produced in an FOPT is in a frequency range to which the future space-based gravitational wave observatories like `LISA` [28,188,189] could potentially be sensitive. The Signal-to-Noise ratio (SNR) of the GWs tells us if a GW signal from an FOPT can be detected by `LISA`. It can be computed as [28]

$$\mathrm{SNR} = \sqrt{\mathcal{T}\int_{f_{\rm min}}^{f_{\rm max}} \mathrm{d}f \left[\frac{h^2\Omega_{\rm GW}(f)}{h^2\Omega_{\rm Sens}(f)}\right]^2}, \tag{3.84}$$

where $h^2\Omega_{\rm GW}(f)$ is the gravitational wave signal, $h^2\Omega_{\rm Sens}(f)$ is the nominal strain sensitivity of `LISA` [229] of a given `LISA` configuration to stochastic sources, $\mathcal{T}$ is the experimental acquisition time in seconds, and $f_{\rm min}$ and $f_{\rm max}$ are minimum and maximum frequency, respectively, to which `LISA` is sensitive. The expected acquisition time of data for `LISA` is around 4 years with a minimum duty cycle of 75% [230] so that we choose $\mathcal{T} = 3\,\text{years}\cdot 365.25\,\text{days/year}\cdot 86400\,\text{s/day} = 94672800\,\text{s}$, and hence

$$\text{SNR in } \texttt{BSMPTv3}\text{: } \mathrm{SNR}(3\,\text{years})\,. \tag{3.85}$$

In case one wants to calculate the SNR with an acquisition time of $\mathcal{Y}$ years, the SNR calculated by `BSMPT` can be rescaled as

$$\mathrm{SNR}(\mathcal{Y}) = \sqrt{\frac{\mathcal{Y}}{3}}\mathrm{SNR}(3\,\text{years})\,. \tag{3.86}$$

The nominal sensitivity $h^2\Omega_{\rm Sens}(f)$ can be written as a function of the power spectral density $S_h(f)$, given in the `LISA` mission requirements [230,226,231] as

$$\Omega_{\rm Sens}(f) = \frac{4\pi^2}{3H_0^2} f^3 S_h(f)\,, \tag{3.87}$$

where $H_0 = 67.4 \pm 0.5\,\text{km}/s/\text{Mpc}$ is the Hubble constant today [211]. A GW signal is considered to be detectable if it gives rise to an SNR > 10.

3.6. The class `TransitionTracer`

The class `TransitionTracer` interfaces all previously described classes, `MinimumTracer`, `BounceSolution` and `GravitationalWave`, with the executables. It initiates the phase tracking, calling the routines of `MinimumTracer`, and collects all phases and coexisting phase pairs with

their critical temperatures. It then goes through all pairs of coexisting false and true phases[24] for which a critical temperature could be determined[25] and tries to determine a bounce solution using the algorithms described in `BounceSolution`. If a bounce solution is successfully determined, it is evaluated in the temperature range of the overlap region to determine the characteristic temperatures of the transition, i.e. the nucleation temperature (cf. Eq. (3.32)), the percolation temperature (cf. Eq. (3.34)), and the completion temperature (cf. Eq. (3.35)). If requested by the user, we then calculate the gravitational wave signal for each phase pair that was found to have the transition temperature (as chosen by the user through the input).

`BSMPTv3` calculates characteristic temperatures and gravitational wave signals for all phase pairs that are found. However, some transitions might cosmologically be impossible to realize due to the respective false phase never getting populated by a sufficient fraction of the universe. Therefore, apart from managing the calculation, the class `TransitionTracer` also reports on the transition history for each point. We label found phases and coexisting phase pairs with increasing indices $\{0, 1, \dots\}$ for decreasing upper temperatures T_{high}. After studying all phase pairs with the algorithms of `BounceSolution` and `GravitationalWave` as described above, we collect all phase pairs for which a *completing* transition could be calculated, meaning a completion temperature was reached. Then, starting from the initial phase which is assumed to be the global minimum at the user-specified highest temperature of the tracing, T_{high}, phase `0`, `TransitionTracer` goes through all pairs with false phase `0` until a first pair with T_{compl} is found before any other transition becomes possible. Then, the old true phase becomes the new false phase and we continue to look for transitions until no transition for the current false phase can be found anymore. We then report the transition history for the point in a column `transition_history` in the form of a string of the following form in the output file, as further described in the following sections for the executables,

$$0 - (\texttt{i1}) \to \texttt{j1} - (\texttt{i2}) \to \texttt{j2} - \dots ,$$

with `i1`, `i2` being placeholders for the phase pair indices and `j1` and `j2` being placeholders for the phase indices in the notation described above. In this example, first in the pair `i1` a transition completes into the true phase `j1` that then is the false phase of a second transition in the pair `i2` into the true phase `j2`. For examples on how the transition history is reported and how the output is interpreted, consult Sec. 4 where we illustrate results for benchmark points.

Note, that `BSMPTv3` assumes non-overlapping transitions: The calculation of the percolation and completion temperatures described in Sec. 3.4.3 and the reported transition history are only valid for one transition happening between one pair of false and true phases.

During the calculation, we report on its intermediate state by throwing status codes, managed by `TransitionTracer`. In the sections about the executables, Secs. 3.7-3.9, all relevant codes are introduced, and a complete summary of them is given in Sec. 3.12.

3.7. The executable `MinimaTracer`

The minimum tracing algorithm is capable of identifying the temperature evolution of non-global and global minima in a user-defined temperature interval $T_{\text{low}} = 0\,\text{GeV} \leq T \leq T_{\text{high}}$. Minimum tracing is the first step before we determine the characteristic temperatures and from there calculate the spectrum of gravitational waves. The executable `MinimaTracer` allows to separately perform the phase tracing for one or more input parameter points and saves all found phases in one output file per point. Calling the executable without arguments `./bin/MinimaTracer` or with the `-help`-flag `./bin/MinimaTracer -help` prints out the following menu:

```
MinimaTracer traces phases in T = [0, Thigh] GeV
it is called by

  ./bin/MinimaTracer model input output firstline lastline

or with arguments

  ./bin/MinimaTracer [arguments]

with the following arguments, ([*] are required arguments, others are optional):

argument                    default   description
--help                                shows this menu
--model=                              [*] model name
--input=                              [*] input file (in tsv format)
--output=                             [*] output file (in tsv format)
--firstline=                          [*] line number of first line in input file
                                          (expects line 1 to be a legend)
--lastline=                           [*] line number of last line in input file
--thigh=                    300       high temperature [GeV]
--multistepmode=            default   multi-step PT mode
                                      default: default mode
                                      0: single-step PT mode
                                      >0 for multi-step PT modes:
                                      1: tracing coverage
                                      2: global minimum tracing coverage
                                      auto: automatic mode
```

[24] With decreasing temperature newly appearing phases are first local minima relative to the already existing phases. Therefore, in a pair of coexisting phases, the phase which is found to exist since a higher temperature is always considered the respective false phase.

[25] A critical temperature can be determined if the false phase starts as the lower minimum at the highest temperature of the overlap and ends as the higher minimum at the lowest temperature of the overlap, or if the true phase starts already as the lower minimum at the highest temperature of the overlap. In the former case, the critical temperature is found in between the lowest and the highest temperature of the coexisting temperature region, in the latter case the critical temperature is set to the highest temperature of the overlap.

```
--num_pts=                10        intermediate grid-size for default mode
--checkewsr=              on        check for EWSR at high temperature
                                    on: perform check
                                    off: check disabled
--usegsl=                 true      use GSL library for minimization
--usecmaes=               true      use CMAES library  for minimization
--usenlopt=               true      use NLopt library for minimization
--usemultithreading=      false     enable multi-threading for minimizers
--json=                             use a json file instead of cli parameters
```

A minimal example call being

```
./bin/MinimaTracing --model=MODEL --input=input.tsv --output=output --firstline=2 --lastline=2
```

traces the point of model `MODEL` found in the second line of the tab-separated input file `input.tsv` in between $T \in \{0, 300\}$ GeV. Note that the first line of the input file is expected to be a legend. The temperature range for the tracing can be specified by setting the optional flag `-thigh` to a user-defined value. The optional mode for multi-step phase tracing `-multistepmode` with its optional grid size `-num_pts` for the default mode is discussed in detail below in Sec. 3.7.1. The check of electroweak symmetry restoration controlled via `-checkewsr` is discussed in detail below in Sec. 3.7.2. The flags `-UseGSL`, `-UseCMAES`, `-UseNLopt` can be used to enable or disable the three implemented minimising libraries separately. By default, all installed and linked libraries are enabled. Setting `-UseMultithreading=true` enables CPU-parallelization via the `C++-thread` class. Additional terminal output for any of the executables can be requested by enabling any or all of the following `logginglevels` of the `Logger` class. All output of `BSMPT` is channelled through the `Logger` class since `BSMPTv2.3`, the new release of `BSMPTv3` extends this by five new `logginglevels` so that we have

`-logginglevel::`	default	description
`default=`	`true`	print output enabled by default
`debug=`	`false`	print additional output useful for debugging
`disabled`	-	disable all output
`ewbgdetailed=`	`false`	show additional output during the calculation of the baryon asymmetry[a]
`progdetailed=`	`false`	show status messages generated by executables
`minimizerdetailed=`	`false`	show additional minimizer-output
`transitiondetailed=`	`false`	show additional output of the `TransitionTracer` class
`mintracerdetailed=`	`false`	show additional output of the `MinimumTracer` class
`bouncedetailed=`	`false`	show additional output of the `BounceSolution` class
`gwdetailed=`	`false`	show additional output of the `GravitationalWave` class
`complete=`	`false`	enable all `logginglevels` above except `minimizerdetailed`

[a] We remind the reader, that this is only relevant for the C2HDM, as only in this model the baryon asymmetry is calculated.

The executables also accept input in form of `json` files if the package [153] was found during installation. Examples for all executables, on how `json`-files can look like can be found in `example/JSON`. After the executable ran successfully, the output is saved in `output_1.tsv`[26] in tabular-separated form by extending `input.tsv` by the status columns (a summary on all status codes is presented in Sec. 3.12)

`status_nlo_stability` Reports `success` if the next-to-leading order (NLO) zero-temperature global minimum is found to lie at the position of the electroweak tree-level minimum and `no_nlo_stability` if not. Note, that for the `MinimaTracer` executable NLO stability is merely a status, not an error code.

`status_ewsr` Stores information on the status of the check for electroweak symmetry restoration, more information is found in Sec. 3.7.2.

`status_tracing` Contains information on the success of the tracing; details on the multi-step phase transition mode can be found in Sec. 3.7.1.

as well as the following columns for each found and traced phase `i`:

`Temp_i` Temperature in [GeV] of each tracing step in phase `i`.

`omega_X(Temp_i)` Field value of direction `X` in [GeV] at temperature `Temp_i`. The labels of direction `X` are model-specific and defined in `addLegendVEV()` in the respective model file.

`Veff(Temp_i)` Value of the one-loop corrected effective potential in [GeV] at phase configuration `omega_X(Temp_i)` at temperature `Temp_i`.

The last column `runtime` logs the runtime of the code after each tracing step in seconds.

Note, that in addition to the new `MinimaTracer` executable, we continue to ship the `VEVEVO` executable with `BSMPTv3`. `VEVEVO` calculates and outputs the location of the global minimum in a multi-dimensional field space using minimisation routines from `GSL`, `CMAES` and `NLopt`. For a documentation consult [19]. The new executable `MinimaTracer` is designed to use the new algorithms of local-minimum tracing enabling `BSMPTv3` to track the location of global and non-global minima over temperature ranges and to look for regions of coexisting phases.

The next section, Sec. 3.7.1, describes in detail how we manage the tracing of multiple, possibly coexisting, phases and how the users can customize the tracing method according to their needs.

[26] The index refers to the point number, for which the output is given.

3.7.1. Multi-step phase transition mode

We trace individual phases using the algorithms described in Sec. 3.3. In order to be able to study phase transition histories with multiple phases that possibly exist in overlapping temperature regions we make the following assumptions:

1. At the user-defined temperature T_{high} and at $T_{\text{low}} = 0\,\text{GeV}$ the universe is realized in the global minimum of its one-loop corrected effective potential.
2. Phases that always remain the non-global minimum over the whole temperature range escape our multi-step phase tracing as we, for the moment, only use global minima positions as *seeds* for the phase tracing.

   The only exception to this assumption is the electroweak minimum with $v = 246\,\text{GeV}$ at $T = 0\,\text{GeV}$, that we always use as an additional seed point, as this is at least a local minimum due to the choice of our counterterm potential. For the executables `CalcTemps` (see Sec. 3.8) and `CalcGW` (see Sec. 3.9) the potential is required to be NLO stable by default, meaning that unphysical points with a one-loop global minimum at zero temperature, which is different from the electroweak minimum, are discarded immediately. However, the user can switch off this requirement with `-checknlo=off`. In this case then also an only non-global electroweak minimum gets traced.
3. Phases start as a non-global minimum when they are first found at their highest temperature, they only become the global minimum at a lower temperature. This statement assumes that `BSMPTv3` is able to trace the phase over the whole temperature region in which it exists.

The user can specify how the minimum tracing algorithm detects possible multi-step phase transitions by setting the flag `-multistepmode` to `default`, `0`, `1`, `2` or `auto`. By default, `mode default` is selected. For most points, it will provide successful tracing with `status_tracing = success`, while being the most resource-optimized. In addition to `mode default`, we offer four tracing modes with slightly different algorithms. These are `mode 0`, which is optimal if the user is only interested in one-step first-order phase transitions; `mode 1` if one wants to ensure tracing coverage with a global minimum check at phase endpoints for multi-step phase tracing; `mode 2` enforces global minimum tracing coverage explicitly. The `auto` mode automatizes `mode 1` and `mode 2` by running `mode 2` in case the global minimum check at phase endpoints fails for `mode 1`.

More details on all five implemented multi-step phase transition modes are given in the following. In Fig. 3 the respective tracing algorithms are illustrated.

`mode default` The default tracing mode provides a fast and customizable grid-checked way of tracking phases for points with multi-step phase transition. It starts at the global minimum at the user-defined T_{high} and tries to trace it down to $T_{\text{low}} = 0\,\text{GeV}$. When the currently traced phase ends, the new global minimum is traced subsequently until a phase existing down to $T_{\text{low}} = 0\,\text{GeV}$ is found. The global minimum at $T_{\text{low}} = 0\,\text{GeV}$ is also traced up to T_{high}. The default mode then uses the global minima found at an equidistant temperature grid as additional seed points to check the completeness of the tracing. Each of these points are checked whether they are part of an already traced phase, and if not, are traced between $\{0, T_{\text{high}}\}$ and added as a new phase. By increasing the grid-size of equally-spaced intermediate checked points, by setting `-num_pts` to a value larger than the default value `-num_pts=10`, the user can fine-tune the tracing granularity.

Note, that this mode returns success, `status_tracing=success`, if tracing *coverage* is found, so if at least one phase is found for each temperature in the traced temperature interval. This does not necessarily indicate that the found phase structure contains the global minimum in the whole temperature range, which we call *global minimum coverage*. Global minimum coverage, if not already achieved with the default settings of `-multistepmode=default`, can be ensured by requesting a larger grid-size.

In case temperature gaps between traced phases are identified, we try to *patch up* such gaps by explicitly choosing and tracing seed points inside the temperature gap. Note, that we attempt to patch up gaps until $\Delta T < 10^{-6}\,\text{GeV}$. Gaps smaller than $10^{-6}\,\text{GeV}$ are no longer patched up. In that case we cannot numerically find tracing coverage with `mode default` and `status_tracing` is set to the error code `no_coverage`.

`mode 0` **one-step phase transition mode**: This is a dedicated mode to exclusively look for one-step first-order phase transitions. It only traces the global minima from $T_{\text{low}} = 0\,\text{GeV}$ towards T_{high} and from T_{high} towards $T_{\text{low}} = 0\,\text{GeV}$, respectively. If they are found to overlap and the high-temperature phase is found to be the global minimum when the low-temperature phase ends at its highest temperature and vice versa, a valid one-step phase transition point was found and `status_tracing` reports `success`.

The calculation for this mode reports an error code if the low-temperature and the high-temperature phase are not found to overlap (`no_coverage`) or no global minimum coverage was found (`no_glob_min_coverage`), indicating that no valid one-step phase transition can exist for this point. If in this mode we cannot find a stable seed point for the two phases, an error code `no_mins_at_boundaries` is reported.

`mode 1` **enforced tracing coverage mode**: This mode is specialized to deal with multi-step phase transitions, and will (as far as it is numerically possible) enforce coverage while checking for global minimum coverage in a performance-optimized way, similarly to the check done by `mode 0`, as elaborated below. It therefore can deal best with points illustrated in Fig. 3 (second from right), which have multiple phases and multiple overlaps between them which only consist of exactly two phases at a time. Again, like in `mode 0`, the initial low- and high-temperature phases are traced and if they are not found to coexist, then, at their respective phase-end-points, we determine the global minimum again and trace it up and down in temperature, until we reach full coverage by traced phases over the whole temperature region. Temperature gaps with no phases found larger than $10^{-6}\,\text{GeV}$ are patched up as described for `mode default`. Global minimum coverage is ensured by checking at all temperatures coinciding with phase end points (from tracing up and down in temperature) whether the lower and higher temperature phases coincide with the global minimum. If global minimum coverage is achieved in this sense, we classify a valid multi-step phase transition point with `status_tracing=success`. In this case, using `mode 1` and not `mode 2`, can significantly save runtime. If for any intermediate overlap we do not find the global minimum as part of any of the already traced phases, we miss tracing the global minimum in some areas of the temperature region. Then, rerunning the parameter point with `-multistepmode=2` is recommended and minima tracing fails with `status_tracing=no_glob_min_coverage`.

`mode 2` **enforced global minimum tracing coverage mode**: Finally, `mode 2` has the strongest implemented check for global minimum coverage. It can reliably deal with multi-step phase transition points with multiple overlaps between any number of phases as well as overlaps between phases that only coexist while both no longer include the global minimum, as illustrated in Fig. 3 (right).

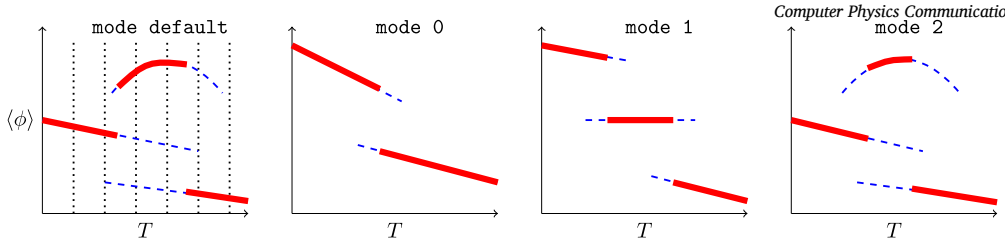

Fig. 3. Illustration of the multi-step phase transition modes `default`, `0`, `1`, `2` (from left to right) for the exemplary class of points where the respective mode performs best. Mode `auto` attempts to run `mode 1` and only if unsuccessful, immediately afterwards starts `mode 2`. All modes are described in detail in the text. The diagrams show the phases in the generic field coordinate $\langle\phi\rangle$ for each point as a function of the temperature T. Temperature regions in which the found minimum is the global minimum are marked by bold red lines, regions in which the phase contains only a non-global minimum are marked by thinner dashed blue lines. The vertical dotted black lines in the left-most diagram that illustrates `mode default` represent the grid points that are used for additional tracing seeds.

It works similarly to `mode 1`, but in addition we track how long a traced minimum is still found to be the global minimum. At temperatures where the global minimum is no longer part of the traced phase, a new phase gets traced and added using the new global minimum as a seed point. The procedure is repeated until the whole temperature range is covered, making sure that the global minimum is a subset of all traced phases in the whole traced temperature range. In this mode we again patch up gaps as described for `mode default` and it can only fail with `no_coverage` in case tracing coverage can numerically not be achieved.

`mode auto` **automatic mode**: This mode automatizes the choice between `mode 1` and `mode 2`. It first attempts to run `mode 1` and switches to the more resource-intensive `mode 2` in case of failure with `no_glob_min_coverage`. Note that `mode auto` therefore relies in a first iteration on the global minimum coverage check that only takes into account phase end points, as described above, and only in case of failure, moves on to `mode 2`.

All above-mentioned status codes for the minima tracing are logged in the `status_tracing` column. Note that, as described above, even though the performance-optimized modes suffice, `success` in `mode default`, `mode 0` or `mode 1` (and `mode auto`) can still mean that the global minimum is not part of the traced phases at every temperature inside the interval. The `mode 0` and `mode 1` only check if the global minimum at the endpoints of the traced phases is part of a different traced phase and therefore for complicated transition histories might miss phases.[27] The same applies to `mode auto`, as it relies in a first iteration on the reduced global minimum endpoint coverage check done by `mode 1`. Full global minimum coverage, however, can be achieved in the `default` mode by increasing the size of the checked point-grid by setting `-num_pts` to a value larger than the default value 10. For a reasonable choice of `-num_pts`, `mode default` is as accurate as `mode 2` while being orders of magnitude faster. The `mode 2` ensures full global minimum tracing coverage for any point independent of its phase structure at the expense of runtime.

3.7.2. Electroweak symmetry restoration check

The loop-corrected effective potential at finite temperature T as function of the classical constant field configuration, generically denoted by ω, implemented in `BSMPT` is given by

$$V(\omega,T) = V(\omega) + V^T(\omega,T) \equiv V^{(0)}(\omega) + V^{\rm CW}(\omega) + V^{\rm CT}(\omega) + V^T(\omega,T)\,, \tag{3.88}$$

where $V^{(0)}(\omega)$ is the tree-level potential, $V^{\rm CW}(\omega)$ is the zero-temperature Coleman-Weinberg potential, $V^{\rm CT}(\omega)$ is the counterterm potential and $V^T(\omega,T)$ contains the thermal corrections at finite temperature T. In the following, we derive the high-temperature limit of the effective potential, which is obtained from $V^T(\omega,T)$, that in the notation of [232] is given by

$$V^T(\omega,T) = \sum_{X=S,G,F} (-1)^{2s_X}\left(1+2s_X\right)\frac{T^4}{2\pi^2} J_\pm\left(\Lambda^{xy}_{(X)}/T^2\right), \tag{3.89}$$

where

$$J_\pm\left(\Lambda^{xy}_{(X)}/T^2\right) = {\rm Tr}\left[\int_0^\infty {\rm d}\mathbf{k}\, k^2 \log\left[1 \pm \exp\left(-\sqrt{k^2 + \Lambda^{xy}_{(X)}/T^2}\right)\right]\right], \tag{3.90}$$

is a function of the mass matrices $\Lambda^{xy}_{(X)}$ of scalars (S), gauge bosons (G) and fermions (F), respectively, that is evaluated via a trace Tr. The spins are denoted by s_X for the scalar, gauge and fermion fields, respectively, J_- is used for bosons and J_+ is used for fermions. Additionally, daisy corrections [233] $\Pi^{ij}_{(S)}$ and $\Pi^{ab}_{(G)}$ are also considered, given by

$$\begin{aligned}\Pi^{ij}_{(S)} =& \frac{T^2}{12}\left[(-1)^{2s_S}\left(1+2s_S\right)\sum_{k=1}^{n_{\rm Higgs}} L^{ijkk} + (-1)^{2s_G}\left(1+2s_G\right)\sum_{a=1}^{n_{\rm gauge}} G^{aaij}\right.\\ &\left.+(-1)^{2s_F}\left(1+2s_F\right)\frac{1}{2}\sum_{I,J=1}^{n_{\rm fermion}}\left(Y^{*IJi}Y^j_{IJ} + Y^{*IJj}Y^i_{IJ}\right)\right]\end{aligned} \tag{3.91}$$

[27] The multi-step modes `mode 1` (and `mode 0`) would report `success` even though the global minimum is missed in case of a phase (or an overlap of phases) that only for an intermediate region does not contain the global minimum. In this scenario, the global minimum moves to a new phase only in an intermediate temperature range of the initial phase that remains the global minimum for its lower and higher temperatures, therefore passing the global minimum coverage check that only relies on the check of the phase end points. Such a scenario, where `mode 1` would falsely report success, is shown in Fig. 3 (right) illustrating the overlap of two phases where the global minimum is no longer contained in any of the two phases.

$$\Pi^{ab}_{(G)} = T^2 \frac{2}{3}\left(\frac{\tilde{n}_H}{8}+5\right)\frac{1}{\tilde{n}_H}\sum_{m=1}^{n_{\text{Higgs}}}\Lambda^{aamm}_{(G)}\delta_{ab}\,, \tag{3.92}$$

where only the longitudinal modes of the gauge bosons get the daisy corrections and $\tilde{n}_H \leq n_{\text{Higgs}}$ is the number of Higgs fields coupling to the gauge bosons, and n_{fermion} and n_{gauge} are the numbers of the fermion and gauge fields in the theory, respectively. The definition of the tensors L^{ijkk}, G^{aaij}, Y^{IJj}, and $\Lambda^{aamm}_{(G)}$ can be found in [18]. There are two different approaches to implement the temperature-corrected Daisy-resummed masses in the effective potential. In the Arnold-Espinosa approach [131] one makes the replacement

$$V^T(\omega,T) \to V^T(\omega,T) + V_{\text{daisy}}(\omega,T) \tag{3.93}$$

$$V_{\text{daisy}}(\omega,T) = -\frac{T}{12\pi}\left[\sum_{i=1}^{n_{\text{Higgs}}}\left(\left(\overline{m}_i^2\right)^{3/2} - \left(m_i^2\right)^{3/2}\right) + \sum_{a=1}^{n_{\text{gauge}}}\left(\left(\overline{m}_a^2\right)^{3/2} - \left(m_a^2\right)^{3/2}\right)\right], \tag{3.94}$$

where m_i^2, $\overline{m}_i^2$, m_a^2, $\overline{m}_a^2$ are the eigenvalues of $\Lambda^{ij}_{(S)}, \Lambda^{ij}_{(S)} + \Pi^{ij}_{(S)}, \Lambda^{ab}_{(G)}, \Lambda^{ab}_{(G)} + \Pi^{ab}_{(G)}$, respectively. The tensors $\Lambda^{ij}_{(S)}$ and $\Lambda^{ab}_{(G)}$ are the coefficients of the Lagrangian terms bilinear in the scalar and in the gauge fields, respectively. Remark, that only the longitudinal modes of the gauge bosons get the thermal corrections $\Pi^{(ab)}_{(G)}$. In the Parwani approach [159], one replaces

$$\Lambda^{ij}_{(S)} \to \Lambda^{ij}_{(S)} + \Pi^{ij}_{(S)}, \tag{3.95}$$

and also

$$\Lambda^{ab}_{(G)} \to \Lambda^{ab}_{(G)} + \Pi^{ab}_{(G)}, \tag{3.96}$$

for the longitudinal modes. Therefore the Debye corrected masses are also used in the V^{CW} potential. Since the high-temperature limit of the potential depends on which of the two approaches is used, it has to be analysed for the two schemes separately.

In the Arnold-Espinosa scheme, the thermal correction are contained in $V^T(\omega,T)$ and $V_{\text{daisy}}(\omega,T)$. For high temperatures, i.e. $x^2 = m^2/T^2 \ll 1$, the thermal functions $J_\pm$ can be approximated as

$$\begin{aligned} J_+\left(x^2,n\right) = &-\frac{7\pi^4}{360} + \frac{\pi^2}{24}x^2 + \frac{1}{32}x^4\left(\log x^2 - c_+\right) \\ &- \pi^2 x^2 \sum_{l=2}^{n}\left(-\frac{1}{4\pi^2}x^2\right)^l \frac{(2l-3)!!\zeta(2l-1)}{(2l)!!(l+1)}\left(2^{2l-1}-1\right) \end{aligned} \tag{3.97}$$

$$\begin{aligned} J_-\left(x^2,n\right) = &-\frac{\pi^4}{45} + \frac{\pi^2}{12}x^2 - \frac{\pi}{6}\left(x^2\right)^{3/2} - \frac{1}{32}x^4\left(\log x^2 - c_-\right) \\ &+ \pi^2 x^2 \sum_{l=2}^{n}\left(-\frac{1}{4\pi^2}x^2\right)^l \frac{(2l-3)!!\zeta(2l-1)}{(2l)!!(l+1)}, \end{aligned} \tag{3.98}$$

where

$$c_+ = \frac{3}{2} + 2\log\pi - 2\gamma_E \tag{3.99}$$

$$c_- = c_+ + 2\log 4\,, \tag{3.100}$$

where γ_E denotes the Euler-Mascheroni constant, $\zeta(x)$ the Riemann ζ-function and $(x)!!$ the double factorial. Taking into account the leading two terms in the high-temperature expansion, the asymptotic behaviour of the $J_\pm$ is given by

$$J_+\left(x^2\right) \sim -\frac{7\pi^4}{360} + \frac{\pi^2}{24}x^2 \tag{3.101}$$

$$J_-\left(x^2\right) \sim -\frac{\pi^4}{45} + \frac{\pi^2}{12}x^2. \tag{3.102}$$

Inserting this high-temperature expansion in (3.93), we find the asymptotic behaviour of $V^T(\omega,T)$ as

$$\begin{aligned} V^T(\omega,T) \sim &-T^4\frac{\pi^2}{720}\left(8n_{\text{Higgs}} - (2\cdot 7)n_{\text{fermion}} + (3\cdot 8)n_{\text{gauge}}\right) \\ &+ \frac{T^2}{24}\left[\text{Tr}\left(\Lambda^{xy}_{(S)}\right) - \text{Tr}\left(\Lambda^{xy}_{(F)}\right) + 3\text{Tr}\left(\Lambda^{xy}_{(G)}\right)\right]. \end{aligned} \tag{3.103}$$

We do not expand the daisy corrections in the high-temperature limit, but explicitly factor out their dependence on the temperature as

$$\Pi^{xy}_{(S)} = T^2\tilde{\Pi}^{xy}_{(S)} \tag{3.104}$$

and

$$\Pi^{ab}_{(G)} = T^2\tilde{\Pi}^{ab}_{(G)}\,, \tag{3.105}$$

where the tilde denotes that these matrices are explicitly temperature independent. The eigenvalues of $\Pi^{xy}_{(S)}$ and $\Pi^{ab}_{(G)}$ can be written as $T^2\widetilde{m}_i^2$ and $T^2\widetilde{m}_a^2$, respectively, where $\widetilde{m}_i^2$ and $\widetilde{m}_a^2$ are the eigenvalues of $\tilde{\Pi}^{xy}_{(S)}$ and $\tilde{\Pi}^{ab}_{(G)}$, respectively. They are temperature independent. At high temperature, we expect $\overline{m}_i^2$ ($\overline{m}_a^2$) and $T^2\widetilde{m}_i^2$ ($T^2\widetilde{m}_a^2$) to differ by a perturbative effect induced by $\Lambda^{xy}_{(S)}$ ($\Lambda^{ab}_{(G)}$). Similar to perturbation theory in quantum mechanics and using the fact that the $\Pi^{xy}_{(S)}$ and $\Pi^{ab}_{(G)}$ are hermitian, the shift of the mass eigenvalues is given by

$$\overline{m}_i^2 \sim T^2\widetilde{m}_i^2 + \frac{\vec{\psi}_i \cdot \Lambda_{(S)}^{xy} \cdot \vec{\psi}_i}{(\vec{\psi}_i)^2} \tag{3.106}$$

$$\overline{m}_a^2 \sim T^2\widetilde{m}_a^2 + \frac{\vec{\psi}_a \cdot \Lambda_{(G)}^{ab} \cdot \vec{\psi}_a}{(\vec{\psi}_a)^2}\,, \tag{3.107}$$

where $\vec{\psi}_i$ ($\vec{\psi}_a$) are the eigenvectors of $\Pi_{(S)}^{xy}$ ($\Pi_{(G)}^{ab}$) associated with the eigenvalue $T^2\widetilde{m}_i^2$ ($T^2\widetilde{m}_a^2$). With this, we can write the asymptotic behaviour of the daisy-corrected potential as

$$V_{\text{daisy}}(\omega,T) \sim -\frac{T}{12\pi}\left[\sum_{i=1}^{n_{\text{Higgs}}}\left(\left(T^2\tilde{m}_i^2\right)^{3/2} + \frac{3}{2}T\left(\widetilde{m}_i^2\right)^{1/2}\frac{\vec{\psi}_i \cdot \Lambda_{(S)}^{xy} \cdot \vec{\psi}_i}{(\vec{\psi}_i)^2}\right) + \sum_{a=1}^{n_{\text{gauge}}}\left(\left(T^2\tilde{m}_a^2\right)^{3/2} + \frac{3}{2}T\left(\widetilde{m}_a^2\right)^{1/2}\frac{\vec{\psi}_a \cdot \Lambda_{(G)}^{ab} \cdot \vec{\psi}_a}{(\vec{\psi}_a)^2}\right)\right]. \tag{3.108}$$

In the Parwani scheme, the asymptotic behaviour of $V^T(\omega,T)$ can be written as

$$\begin{aligned} V^T(\omega,T) &= \sum_{X=S,G,F}(-1)^{2s_X}\left(1+2s_X\right)\frac{T^4}{2\pi^2}J_\pm\left(\frac{\Lambda_{(X)}^{xy}+\Pi_{(X)}^{xy}}{T^2}\right), \\ &= \sum_{X=S,G,F}(-1)^{2s_X}\left(1+2s_X\right)\frac{T^4}{2\pi^2}\sum_{i\in X}J_\pm\left(\frac{\overline{m}_i^2}{T^2}\right), \\ &\sim \sum_{X=S,G,F}\left(1+2s_X\right)\frac{(-1)^{2s_X}}{2\pi^2}\sum_{i\in X}\left[T^4J_\pm\left(\widetilde{m}_i^2\right) + T^2\frac{\vec{\psi}_i\cdot\Lambda_{(X)}\cdot\vec{\psi}_i}{(\vec{\psi}_i)^2}J'_\pm\left(\widetilde{m}_i^2\right)\right], \end{aligned} \tag{3.109}$$

where we used the same definitions as in the last section. In this scheme, the daisy corrections also affect the Coleman-Weinberg potential

$$\begin{aligned} &V^{\text{CW}}(\omega) \to V^{\text{CW}}(\omega,T) \\ &= \frac{\varepsilon}{4}\sum_{X=S.G.F}(-1)^{2s_X}\left(1+2s_X\right)\text{Tr}\left[\left(\Lambda_{(X)}^{xy}+\Pi_{(X)}^{xy}\right)^2\left(\log\left(\frac{1}{\mu^2}\left(\Lambda_{(X)}^{xy}+\Pi_{(X)}^{xy}\right)\right)-k_X\right)\right], \\ &\sim \frac{\varepsilon}{4}\sum_{X=S.G.F}(-1)^{2s_X}\left(1+2s_X\right)\left(T^2\log T^2\right)\text{Tr}\left[T^2\left(1+\frac{\log\tilde{\Pi}_{(X)}^{xy}}{\log T^2}\right)\left(\tilde{\Pi}_{(X)}^{xy}\right)^2 + \left\{\Lambda_{(X)}^{xy},\tilde{\Pi}_{(X)}^{xy}\right\}\right]. \end{aligned} \tag{3.110}$$

Using these results, we can factor out the temperature dependence from the effective potential in the two different approaches as ($AS \equiv$ Arnold-Espinosa $P \equiv$ Parwani) and arrive at

$$\left(\frac{V_{\text{eff}}}{T^2}\right)_{\text{Arnold-Espinosa}} \sim (\text{const.})_{AS}\cdot T^2 + V_{AS} + \vec{G}_{AS}\cdot\vec{\omega} + \vec{\omega}\cdot\frac{H_{AS}}{2}\cdot\vec{\omega} \tag{3.111}$$

$$\left(\frac{V_{\text{eff}}}{T^2\log T^2}\right)_{\text{Parwani}} \sim (\text{const.})_{P,1}\cdot T^2 + (\text{const.})_{P,2}\cdot\frac{T^2}{\log T^2} + V_P + \vec{G}_P\cdot\vec{\omega} + \vec{\omega}\cdot\frac{H_P}{2}\cdot\vec{\omega}\,. \tag{3.112}$$

The rescaled potentials Eq. (3.3) for both schemes have a field-independent temperature dependence. In the investigation of the electroweak symmetry restoration (EWSR) of the potential in the high-temperature limit we can therefore ignore the first term in Eq. (3.111) and Eq. (3.112), respectively. The remaining potential parameters $V_{AS}, V_P, \vec{G}_{AS}, \vec{G}_P, H_{AS}$, and H_P are field independent. The relevant part of the effective potential for our investigation is just a quadratic function in the fields $\vec{\omega}$, which has a field-independent Hessian. Therefore, if H_{AS}/H_P has a negative eigenvalue this means that the potential has a concavity in one of the directions. Therefore the minimum, if it exists, must be outside the region where the high temperature expansion holds. If the smallest eigenvalue is zero, then there is an infinite number of degenerate VEVs and more orders in the high-temperature expansion are needed in order to lift this degeneracy, which is not considered in this paper. If the Hessian is positive definite then there exists a single minimum in the region where the high temperature expansion is valid, and it is located at the VEV, given by

$$\langle\vec{\phi}\rangle_{T\to\infty}^{AS} = H_{AS}^{-1}G_{AS} \quad \text{for the Arnold-Espinosa scheme} \tag{3.113}$$

$$\langle\vec{\phi}\rangle_{T\to\infty}^{P} = H_{P}^{-1}G_{P} \quad \text{for the Parwani scheme.} \tag{3.114}$$

The flag `-checkewsr=` allows for the check of electroweak symmetry restoration (EWSR) at high temperature. The results of this check are reported in the column `status_ewsr` that is added in the output file. For the EWSR calculation we iteratively calculate the Hessian matrix of the rescaled potential at the origin $\vec{\omega}_0 = \{0,\cdots,0\}$ until its behaviour is temperature independent, allowing us to determine $\vec{G}_{AS}$ ($\vec{G}_P$) and H_{AS} (H_P), respectively, and, consequently, the shape of the potential. Iteratively means that we calculate the smallest eigenvalue of the Hessian matrix of V_{eff}/T^2, i.e. the lowest mass value, at three different temperatures until the relative difference of the obtained mass values is $\lesssim 10^{-6}$.

The four options that can be set for the flag `-checkewsr=` are

`on`	Enables the check and saves the result without removing any point.
`keep_pos_def`	Enables the check and removes all points that do not have a positive definite Hessian in the high temperature expansion. (Only for `CalcTemps` and `CalcGW`.)
`keep_ewsr`	Enables the check and removes all points with no electroweak symmetry restoration. (Only for `CalcTemps` and `CalcGW`.)
`off`	Disables the check. The `status_ewsr`-column in this case is filled with `off`.

The possible `status_ewsr` codes that can be reported in the output file and their respective meaning are

`off`	The test was disabled.
`failure`	The check failed, because the numerical precision was not sufficient.
`non_pos_def`	The potential does not have a positive definite Hessian.
`flat_region`	There is an infinite number of degenerate VEVs that minimise the rescaled potential.
`ew_sym_non_res`	There is a single minimum at high temperature that does not restore the EW symmetry.
`ew_sym_res`	There is a single minimum at high temperature that restores the EW symmetry.

It is important to note that our conclusions are only valid inside the region where the high-temperature expansion holds. If we predict that a parameter point restores the EW symmetry at high temperature, this does not rule out the possibility of another minimum with a lower energy than the EW-restoring minimum. The same reasoning applies to a parameter point with a non-positive definite Hessian which indicates that no minimum exists inside the region where the high-temperature expansion applies. Still, a minimum could exist outside this region. The conclusion that can definitely be drawn, however, is that if we find that the Hessian is not positive definite then there is no EWSR.

3.8. *The executable* `CalcTemps`

Based on the information obtained from the tracing of the phases in a temperature interval, we calculate characteristic temperatures for all found coexisting phase pairs. The `CalcTemps` executable is an interface to obtain these temperature values directly and therefore extends the `MinimaTracer` algorithm by additional steps to solve the bounce equation and derive the critical, nucleation, percolation and completion temperature, as described in Sec. 3.4.3. Calling `CalcTemps` without arguments, `./bin/CalcTemps`, or with the `-help` flag, `./bin/CalcTemps -help`, prints out the following menu:

```
CalcTemps calculates characteristic temperatures for phase transitions
it is called by

  ./bin/CalcTemps model input output firstline lastline

or with arguments

  ./bin/CalcTemps [arguments]

with the following arguments, ([*] are required arguments, others are optional):

argument                   default   description
--help                               shows this menu
--model=                             [*] model name
--input=                             [*] input file (in tsv format)
--output=                            [*] output file (in tsv format)
--firstline=                         [*] line number of first line in input file
                                         (expects line 1 to be a legend)
--lastline=                          [*] line number of last line in input file
--thigh=                   300       high temperature [GeV]
--multistepmode=           default   multi-step PT mode
                                     default: default mode
                                     0: single-step PT mode
                                     >0 for multi-step PT modes:
                                     1: tracing coverage
                                     2: global minimum tracing coverage
                                     auto: automatic mode
--num_pts=                 10        intermediate grid-size for default mode
--vwall=                   0.95      wall velocity: >0 user defined
                                     -1: approximation
                                     -2: upper bound
--perc_prbl=               0.71      false vacuum fraction for percolation
--compl_prbl=              0.01      false vacuum fraction for completion
--checknlo=                on        check for NLO stability
                                     on: only keep NLO stable points
                                     off: check disabled
--checkewsr=               on        check for EWSR at high temperature
                                     on: perform check and add info
                                     keep_bfb: only keep BFB points
                                     keep_ewsr: only keep EWSR points
                                     off: check disabled
--maxpathintegrations=     7         number of solutions of 1D equation =
                                     number of path deformations + 1
--usegsl=                  true      use GSL library for minimization
--usecmaes=                true      use CMAES library  for minimization
--usenlopt=                true      use NLopt library for minimization
--usemultithreading=       false     enable multi-threading for minimizers
--json=                              use a json file instead of cli parameters
```

Again, the required flags to set are the name of the model to investigate `-model=`, the name of the input file in tsv-format `-input=`, the name of the output file in tsv-format `-output=`, and the line number of the first and the last line in the input file, `-firstline=` and `-lastline=`, respectively. A minimal example call is

```
./bin/CalcTemps --model=MODEL --input=input.tsv --output=output.tsv --firstline=2 --lastline=2
```

Optionally, it is again possible to specify the temperature range in which to trace the phases, whether or not the check for NLO vacuum stability or the check for electroweak symmetry restoration at high temperature is enabled and which mode should be used to handle multi-step phase transitions. Note, that contrary to `MinimaTracer`, if `-checknlo=on`, `no_nlo_stability` acts as an error code, and `-checkewsr=keep_bfb` or `-checkewsr=keep_ewsr` only keep points that are bounded-from-below or restore the EW symmetry at high temperature, respectively. The wall velocity can be set via the flag `-vwall=`. The different options are:

>0	If a value $\in (0,1)$ is given, the wall velocity is set to this value. By default, if no flag is provided, the wall velocity is set to 0.95.
-1	For `-vwall=-1` the approximation, see Eq. (3.44), from Refs. [202,203] is chosen.
-2	For `-vwall=-2` the upper bound, see Eq. (3.45), defined in [122] is chosen.

Additionally, it is possible to define the false vacuum fraction used to define the percolation and the completion temperature via the flags `-perc_prbl` and the `-compl_prbl`, respectively. By default, the percolation false vacuum fraction is set to 71 %, `-perc_prbl=0.71`, and the completion false vacuum fraction to 1 %, `-compl_prbl=0.01`. By setting the optional `-maxpathintegrations=` flag one can specify the number of solutions to the 1D equation which equals the number of path deformations plus one. Note that the choice of the number of path integrations ideally finds a good (model-dependent) balance between the number of attempts and computational time. All other optional flags and the `Logger` classes work in the same way as for `MinimaTracer`, cf. Sec. 3.7.

A successful run of the `CalcTemps` executable attaches the following columns to `input.tsv` and creates and saves the output to `output.tsv`. The first columns report on several status codes whose output partially depends on the set flags:

status_nlo_stability	Information on whether the global minimum of the loop-corrected effective potential at $T = 0$ GeV coincides with the global minimum of the tree-level potential. `success` if the point is found to be NLO stable when `-checknlo=on`, if not `no_nlo_stability` discards the point and `off` indicates that the check is disabled with `-checknlo=off`.
status_ewsr	Information on electroweak symmetry restoration at high temperature, all details can be found in Sec. 3.7.2.
status_tracing	Status of the minima tracing, see Sec. 3.7.1.
status_coex_pairs	If the tracing is successful this column informs on whether (`success`) or not (`no_coex_pairs`) coexisting phases are found.
runtime	Runtime of code in seconds.

More details on all status codes can be found in Sec. 3.12. If pairs of coexisting phases can be identified, we then try to obtain a critical temperature for each pair `i` of coexisting phases:

status_crit_i	If for a phase pair coexisting in $\{T_{\mathrm{i,high}}, T_{\mathrm{i,low}}\}$ we have $\Delta V(T_{\mathrm{i,high}}) > 0$ and $\Delta V(T_{\mathrm{i,low}}) < 0$ with $\Delta V(T) \equiv V_{\mathrm{true}}(T) - V_{\mathrm{false}}(T)$, the critical temperature is identified via binary search between $T_{\mathrm{i,high}}$ and $T_{\mathrm{i,low}}$ and `success` is reported in the status column. If $\Delta V < 0$ in the whole range of coexistence, the true phase is always the lower minimum. We then set $T_c = T_{\mathrm{i,high}}$, and the reported status is `true_lower`. If $\Delta V > 0$ over the whole range of coexistence, the false phase is always the lower minimum and there is no critical temperature for this pair, the reported error is `false_lower`. The identification of the critical temperature for a pair of (false, true) phases fails with `failure` if the true phase starts as a lower minimum at $T_{\mathrm{i,high}}$ and the false phase ends as a lower minimum at $T_{\mathrm{i,low}}$.
T_crit_i, omega_X_crit_false_i, omega_X_crit_true_i	This set of columns for phase pair `i` contains information about the critical temperature T_c in [GeV], the coordinates of the false vacuum and the coordinates of the true vacuum at the critical temperature.

If a critical temperature can be identified successfully for a coexisting phase pair `i`, the next step is to solve the bounce equation and extend the output by the following columns:

status_bounce_sol_i	If a bounce solution for pair `i` can be calculated, the status is `success`, and the derivation of the nucleation, percolation and completion temperatures is attempted. If the calculation of the bounce solution fails, due to e.g. too small overlap, the status is `failure`, and no nucleation, percolation and completion temperature can be calculated for this transition.
status_nucl_approx_i	`success` if Eq. (3.33) can be met, `not_met` if not.
T_nucl_approx_i, omega_X_nucl_approx_false_i, omega_X_nucl_approx_true_i	Attached next are the columns for the approximate nucleation temperature T_n obtained from Eq. (3.33) and the false and true phase coordinates at this temperature, respectively.
status_nucl_i	`success` if Eq. (3.32) can be met, `not_met` if not.
T_nucl_i, omega_X_nucl_false_i, omega_X_nucl_true_i	Contains the nucleation temperature T_n derived from Eq. (3.32) and the false and true phase coordinates at T_n, respectively.
status_perc_i	`success` if Eq. (3.34) with $P_f(T_p)$ optionally set by `-perc_prbl` can be met, `not_met` if not.
T_perc_i, omega_X_perc_false_i, omega_X_perc_true_i	Reports the percolation temperature T_p derived from Eq. (3.34) and the false and true phase coordinates at T_p, respectively.
status_compl_i	`success` if Eq. (3.35) with $P_f(T_f)$ optionally set by `-perc_prbl` can be met, `not_met` if not.
T_compl_i, omega_X_compl_false_i, omega_X_compl_true_i	Informs on the completion temperature T_f derived from Eq. (3.35) and the false and true phase coordinates at T_f, respectively.

Note, that an error message `not_met` might indicate vacuum trapping. The last added column, `transition_history`, reports on the history of transitions that likely took place for the point. For details, compare Sec. 3.6 as well as see the examples in Sec. 4.

3.9. The executable `CalcGW`

Based on the tracing of the phases in the temperature interval $T_{\text{low}} = 0\,\text{GeV} \leq T \leq T_{\text{high}}$, the identification of coexisting phase pairs and the determination of the characteristic temperatures, the `CalcGW` executable provides the calculation of the spectrum of primordial gravitational waves sourced by sound waves and turbulence. The used terminology is introduced in Sec. 3.5.1. Running `./bin/CalcGW` or `./bin/CalcGW -help` prints the following menu, specifying all required and optional arguments:

```
CalcGW calculates the gravitational wave signal
it is called by

  ./bin/CalcGW model input output firstline lastline

or with arguments

  ./bin/CalcGW [arguments]

with the following arguments, ([*] are required arguments, others are optional):

argument                    default   description
--help                                shows this menu
--model=                              [*] model name
--input=                              [*] input file (in tsv format)
--output=                             [*] output file (in tsv format)
--firstline=                          [*] line number of first line in input file
                                          (expects line 1 to be a legend)
--lastline=                           [*] line number of last line in input file
--thigh=                    300       high temperature [GeV]
--multistepmode=            default   multi-step PT mode
                                      default: default mode
                                      0: single-step PT mode
                                      >0 for multi-step PT modes:
                                      1: tracing coverage
                                      2: global minimum tracing coverage
                                      auto: automatic mode
--num_pts=                  10        intermediate grid-size for default mode
--vwall=                    0.95      wall velocity: >0 user defined
                                      -1: approximation
                                      -2: upper bound
--perc_prbl=                0.71      false vacuum fraction for percolation
--compl_prbl=               0.01      false vacuum fraction for completion
--trans_temp=               perc      transition temperature, options are:
                                      nucl_approx: approx nucleation temperature
                                      nucl: nucleation temperature
                                      perc: percolation temperature
                                      compl: completion temperature
--epsturb=                  0.1       turbulence efficiency factor
                                      >0: user defined
                                      -1: upper bound
--pnlo_scaling=             1         1 -> N NLO pressure
                                      1: propto gamma
                                      2: propto gamma^2
--checknlo=                 on        check for NLO stability
                                      on: only keep NLO stable points
                                      off: check disabled
--checkewsr=                on        check for EWSR at high temperature
                                      on: perform check and add info
                                      keep_bfb: only keep BFB points
                                      keep_ewsr: only keep EWSR points
                                      off: check disabled
--maxpathintegrations=      7         number of solutions of 1D equation =
                                      number of path deformations + 1
--usegsl=                   true      use GSL library for minimisation
--usecmaes=                 true      use CMAES library  for minimization
--usenlopt=                 true      use NLopt library for minimization
--usemultithreading=        false     enable multi-threading for minimizers
--json=                               use a json file instead of cli parameters
```

In addition to the previously described required and optional arguments, cf. Secs. 3.7-3.8, `CalcGW` allows the user to set the transition temperature. By default, it is set to $T_* = T_p$, and by specifying `-trans_temp=` one can choose:

`nucl_approx`	Nucleation temperature determined via the approximation of Eq. (3.33).
`nucl`	Nucleation temperature determined via the condition, Eq. (3.32).
`perc`	Percolation temperature evaluated via Eq. (3.34). Note that the false vacuum fraction used to determine the percolation temperature can be set optionally with `-perc_prbl`.

compl Completion temperature calculated via Eq. (3.35). Note that the false vacuum fraction used to determine the completion temperature can be set optionally with `-perc_compl`.

The `-epsturb` flag allows the user to set the turbulence efficiency factor in case a value > 0 is entered. Alternatively, for `-1`, the upper bound of Eq. (3.83) can be chosen. With the flag `-pnlo_scaling=1,2` the user can switch between the NLO pressure with the linear γ scaling of Eq. (3.66) or with the γ^2 scaling of Eq. (3.67). By default, the linear γ scaling is used. A minimal example call can look like:

```
./bin/CalcGW --model=MODEL --input=input.tsv --output=output.tsv --firstline=2 --lastline=2
```

The first columns added to `input.tsv` in `output.tsv` are `status` columns, compare again with Secs. 3.7-3.8 and Sec. 3.12 for a summary of all status codes. Then for each identified coexisting phase pair `i`, the columns containing information on the bounce solution and characteristic temperatures are added, cf. Sec. 3.8. In addition, the information on the gravitational wave spectrum is given out in the following columns with the respective contents:

status_gw_i Status of the gravitational wave calculation, `success` if successful, `failure` if an error was encountered. Possible encountered errors are that the requested transition temperature could not be calculated or that $\frac{\beta}{H} < 1$, cf. Sec. 3.5.1.
T_star_i Transition temperature T_*.
T_reh_i Reheating temperature T_{reh}.
v_wall_i Wall velocity.
alpha_PT_i Strength of the phase transition, Eq. (3.37).
beta/H_i Inverse time scale, Eq. (3.40).
kappa_col_i Efficiency factor for bubble collisions as defined in Eq. (3.57).
kappa_sw_i Sound-wave efficiency factor derived with the method from [193,204], as described in Sec. 3.5.1.
eps_turb_i Efficiency factor for the turbulence contribution as defined in Eq. (3.82).
cs_f_i Sound velocity in the false vacuum as defined in Eq. (3.47).
cs_t_i Sound velocity in the true vacuum as defined in Eq. (3.47).
fb_col_i Characteristic frequency of the collision spectrum as defined in Eq. (3.52)
h2Omegab_col_i Amplitude of the collision spectrum as defined in Eq. (3.51)
f_1_X_i First characteristic frequency break for the sound wave and turbulence source, with `X = sw/turb`, as defined in Eqs. (3.71) and (3.79).
f_2_X_i Second characteristic frequency breaks for the sound wave and turbulence source, with `X = sw/turb`, as defined in Eqs. (3.72) and (3.80).
h2Omega_2_X_i Amplitude Ω_2 for sound waves, `X = sw`, and turbulence, `X = turb`, as defined in Eq. (3.78) and (3.81), respectively.
SNR(LISA-3yrs)_col_i Signal-to-noise ratio (SNR) at `LISA` with an acquisition period of three years, given by Eq. (3.84), for the collision contribution only.
SNR(LISA-3yrs)_sw_i Signal-to-noise ratio for the sound-wave contribution only.
SNR(LISA-3yrs)_turb_i SNR for the turbulence contribution only.
SNR(LISA-3yrs)_i SNR for the collision, sound-wave and the turbulence contribution combined.

The last added column, `transition_history`, reports on the history of transitions that likely took place for the point. For details, compare Sec. 3.6 as well as see the examples in Sec. 4.

3.10. *The executable* `PotPlotter`

Visualizing the multi-dimensional effective potential often is useful for understanding complicated minima landscapes. The executable `PotPlotter` provides an interface for extracting (multi-dimensional) effective potential data grids that can be used to generate different kinds of contour plots. If `./bin/PotPlotter -help` is called, its menu is printed:

```
PotPlotter calculates the effective potential on a user-specified field grid
it is called by

  ./bin/PotPlotter [arguments]

with the following arguments, ([*] are required arguments, others are optional):

argument                  default   description
--help                              shows this menu
--model=                            [*] model name
--input=                            [*] input file (in tsv format)
--output=                           [*] output file (in tsv format)
--line=                             [*] line number of line in input file
                                        (expects line 1 to be a legend)
--temperature=                      [*] temperature [GeV]
--point=                  0,..,0    grid reference point
--npointsi=               0         number of points in direction i
                                    (with i = [1,..,6])
--lowi=                   0         lowest field value in direction i
                                    [* if npointsi > 0] (with i = [1,..,6])
--highi=                  0         highest field value in direction i
                                    [* if npointsi > 0] (with i = [1,..,6])
--slice=                  false     enable slice mode
--min_start=                        [* in slice mode] start minimum
```

```
--min_end=                          [* in slice mode] end minimum
--npoints=                 100      grid size in slice mode
--json=                             use a json file instead of cli parameters
```

The user has to specify the model, the input and output files and the line number, as well as the temperature, at which the contour is to be evaluated. Furthermore, one of the two different operation modes of `PotPlotter` has to be chosen. The two modes work as follows:

`grid mode` The potential values are evaluated on a user-defined grid that lies along the field directions of the model, in which we (model-specifically) allow for the generation of a non-zero finite temperature VEV, called VEV directions in the following. The user has to specify the number of grid points and the grid ranges in all VEV directions in which the grid should span by setting `-npointsi=`, `-lowi=` and `-highi=` to the desired values. Note, that the index `i` runs from `1` to `n` with `n` being the total number of VEV directions. The order of the VEV coordinates is set in the model file and can be read e.g. from the model-specific implementation of `addLegendVEV()`. At the moment, up to six field dimensions are possible for a grid, for higher-dimensional VEV spaces, the algorithm needs to be extended. Optionally, the user can force the evaluation of the point grid with all VEV dimensions that are not axes of the grid set to the coordinates of a reference point. The reference point coordinates are supplied via `-point=x1,..,xn`. If no reference point is specified, all VEV coordinates that are not varied in the grid are set to zero. This is useful if a user wants to display a lower-dimensional projection of a higher-dimensional VEV space.

`slice mode` The potential values are evaluated along a straight line between two user-defined points. The result is a one-dimensional array of potential values along this one-dimensional path. In order to enable the `slice` mode, the user has to set `-slice=true` and specify the coordinates of the two points via `-min_start` and `-min_end`. Again, the order of the VEV coordinates is set in the model file and can be derived e.g. from the model-specific implementation of `addLegendVEV()`. Optionally, the number of points along the straight line at which the potential gets evaluated, can be changed by setting `-npoints=` to the requested number. By default, `-npoints=100` are evaluated.

The output of `PotPlotter` is then saved to the output file where each line corresponds to one grid or slice point. The columns are

`v_X` Field value of direction `X` in GeV for one grid or slice point. The labels of the direction `X` are model-specific and defined in `addLegendVEV()` in the respective model file.
`v_X_point` (only in `grid` mode) Coordinates of the reference point.
`Veff(v,T)` Value of the effective potential in GeV at the grid or slice point and temperature.
`Veff(point,T)` (only in `grid` mode) Effective potential value in GeV at the reference point and temperature.
`T` Temperature in GeV at which the effective potential is evaluated.

Examples on how the output of `PotPlotter` can be used for visualizations can be found in Figs. 8, 9, and 11. The figures in the respective left columns were made using the `slice` mode, the ones in the respective middle and the right columns were made with the `grid` mode with the coordinates of the global minimum chosen as the reference point of the two-VEV-dimensional projection.

3.11. The folder `standalone`

In case the user wants to use some particular function or class of `BSMPTv3`, such as those explained in the last sections, we also provide a few examples on how to do so. They are placed in the folder `standalone` and automatically compiled when `BSMPTv3` is compiled. If new `.cpp` files are created/moved into `standalone` then it is necessary to run `CMake` and compile again so that all libraries are properly linked. Three examples are already put inside `standalone`:

`CalculateAction.cpp` Solves the bounce equation and calculates the Euclidean action. The user is expected to provide the initial guess path and the potential, the gradient is optional.
`GenericModel.cpp` The user provides a potential $V(\vec{\omega})$, the zero temperature VEV and the dimensionality of the VEV directions. This tracks the minima and calculates the GWs spectrum.
`TunnellingPath.cpp` Solves the bounce equation using the full `BSMPTv3` and prints the tunnelling path and the VEV profile in `Mathematica` and `Python` formats.

Remark that the provided examples merely serve as demonstrations of how to use the classes. In case some functionality is missing, the recommended way of extending `BSMPT` is by adding these features in form of functions which can be tested in unit tests. Our team welcomes suggestions. To ensure everything is still working fine, we recommend running the unit tests during development.

3.12. Summary on status codes

We summarize here all codes in text format to log the status of several steps of the calculation. The new status code framework is used by all executables that were added with the release of `BSMPTv3`. For information on status codes of the previous versions, cf. [18,19]. The status codes are listed and described in the following and illustrated in Fig. 4:

`status_nlo_stability` The NLO stability status is set to `success` if the global minimum of the loop-corrected effective potential at $T = 0\,\text{GeV}$ coincides with the global minimum of the tree-level potential. It is set to `no_nlo_stability` otherwise.
`status_ewsr` Status of the EWSR check, described in Sec. 3.7.2. If the check is enabled, it will be filled with one of the following results: `failure` if the test failed; `non_bfb` if the potential is not bounded from below at high temperature; `flat_region` if there is an infinite number of degenerate VEVs that minimise the rescaled potential; `ew_sym_non_res` if

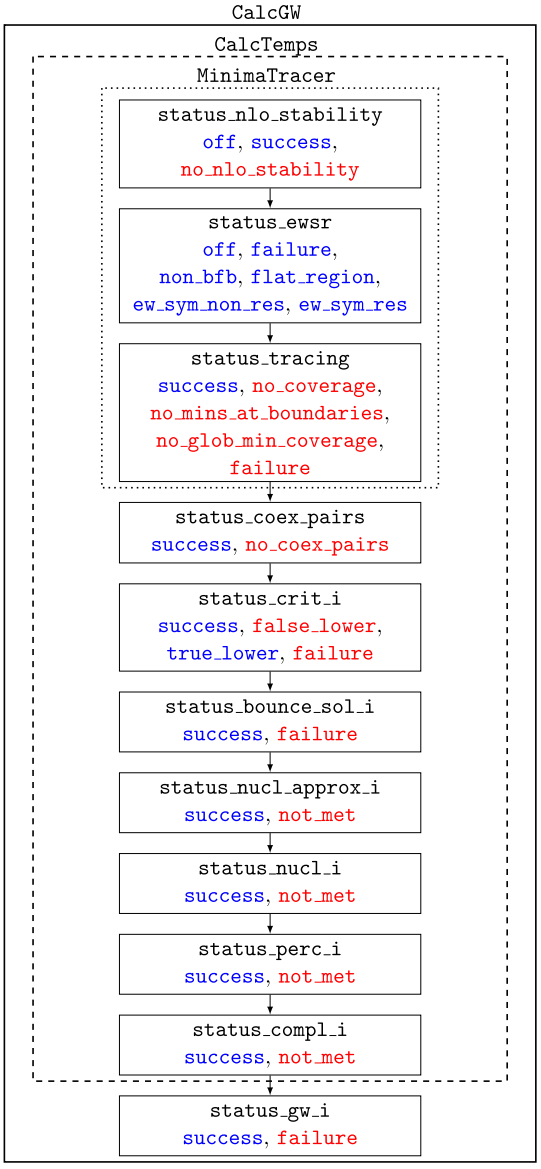

Fig. 4. Logical-flow diagram of `BSMPTv3`. Status codes are marked in blue, error codes in red. If `-checkewsr=keep_bfb` (`-checkewsr=keep_ewsr`) the codes `failure`, `non_bfb` and `flat_region` (`ew_sym_non_res`) for `status_ewsr` act as error codes. All possible error codes in `status_nlo_stability`, `status_ewsr` and `status_tracing` only act as status codes for the executable `MinimaTracer`. Codes are described in the text.

there is a single minimum at high temperature that does not restore the electroweak symmetry and `ew_sym_res` if there is a single minimum at high temperature that restores the EW symmetry.

`status_tracing` Status of the phase tracing algorithm. Successful tracing is logged with `success`. The tracing fails, if no coverage is found or the global minimum is missed for some temperature regions, reported as `no_coverage` and `no_glob_min_coverage`, respectively. If `mode=0` is chosen, meaning that it is searched for a one-step first-order phase transition exclusively, an error code `no_mins_at_boundaries` indicates that we cannot identify a numerically stable local minimum at the edge temperatures 0 or T_{high}. Successful tracing in the mode `default` can still mean that the global minimum escapes tracing in some temperature regions. In this case or in the case of failure, increasing the equidistant point grid size or using a different multi-step phase transition tracing mode might help, cf. also Sec. 3.7.1. The failure code `failure` is reported if either no phases could be traced or the global minimum at $T = 0$ GeV is found at too large field values.

`status_coex_pairs` Status of the check for coexisting phase pairs. If no coexisting phases are found for the point in the whole temperature range, this status is set to `no_coex_pairs`, ending the calculation for this parameter point. As soon as at least one coexisting phase pair is identified, `success` is reported.

`status_crit_i` Status of the calculation of the critical temperature for a coexisting phase pair `i`. If the false phase starts as the lower minimum at the upper temperature of the coexisting region and the true phase ends as the lower minimum at the lower temperature of the coexisting region, the critical temperature lies in between and the status is `success`. If the true phase is always the lower minimum, the critical temperature is located at the upper end of the overlap and the status is `true_lower`. If the false phase remains the lower minimum over the whole overlap region with the true

	phase, there is no critical temperature within the overlap and the error is `false_lower`. If the false phase is found to be the lower minimum at the low temperature and the true phase is found to be the lower minimum at the high temperature, the reported error is `failure` and there is no critical temperature for the identified pair of (false, true) phase.
`status_bounce_sol_i`	Status of the bounce solution calculation for coexisting phase pair `i`. `success` if a bounce solution can be calculated in the temperature range of the phase pair overlap, `failure` otherwise.
`status_nucl_approx_i`	Status of the approximate nucleation temperature calculation for coexisting phase pair `i`. `success` if Eq. (3.33) can be fulfilled, `not_met` if not.
`status_nucl_i`	Status of the nucleation temperature calculation for coexisting phase pair `i`. `success` if Eq. (3.32) can be fulfilled, `not_met` if not.
`status_perc_i`	Status of the percolation temperature calculation for coexisting phase pair `i`. `success` if Eq. (3.34) can be fulfilled, `not_met` if not.
`status_compl_i`	Status of the completion temperature calculation for coexisting phase pair `i`. `success` if Eq. (3.35) can be fulfilled, `not_met` if not.
`status_gw_i`	Status of the gravitational wave calculation for coexisting phase pair `i`. Set to `failure` if the requested transition temperature could not be calculated or a $\frac{\beta}{H} < 1$ is identified, `success` otherwise.

4. Examples and comparison with `CosmoTransitions`

This section illustrates the functionality and usage of `BSMPTv3` by discussing some sample parameter points and by performing a comparison between `BSMPTv3` and `CosmoTransitions`.[28] We start in Sec. 4.1 with the comparison of the solutions provided by the two codes for the bounce equation in a toy model. We then compare in Sec. 4.2 the phases and phase transitions for sample benchmark points. In Sec. 4.3 a comparison is performed on a broader basis by using a parameter point sample obtained from a parameter scan in the 2HDM which takes into account all relevant theoretical and experimental constraints.

4.1. Comparison in a toy model

We compare the results for the bounce equation found by `BSMPTv3` and `CosmoTransitions` for the toy model provided by `CosmoTransitions` as an example. It is given by the potential

$$V(\phi_x,\phi_y) = \left(c\,(\phi_x-1)^2+(\phi_y-1)^2\right)\left(c\,\phi_y^2+\phi_x^2\right) + f_x\left(\frac{\phi_x^4}{4}-\frac{\phi_x^3}{3}\right) + f_y\left(\frac{\phi_y^4}{4}-\frac{\phi_y^3}{3}\right). \tag{4.1}$$

For the potential parameters we choose $c=5$, $f_x=0$ and consider two cases $f_y=2$ and $f_y=80$. For all cases, the true vacuum of the potential sits at $(\phi_x,\phi_y)=(1,1)$ and the false vacuum at $(\phi_x,\phi_y)=(0,0)$. The potential contours for the two cases are depicted in Fig. 5 (upper). The middle plots show the tunnelling path obtained by `CosmoTransitions` (red) and `BSMPTv3` (blue), respectively, as a function of the distance ρ from the true vacuum. The lower plots display the difference between the tunnelling path calculated by `CosmoTransitions` and `BSMPTv3`. The left plots are for $f_y=2$ and the right plots for $f_y=80$.

In the case of $f_y=2$, the vacuum phases are almost degenerate so that the starting position is extremely close to the true vacuum, i.e. $\vec{\phi}(\rho=0)\simeq\vec{\phi}_t$. The field starts so close to the true vacuum that it stays near it across a large range of ρ before rolling down the inverted potential. This is because, since the minima are almost generated, the drag term $\propto 1/\rho$ needs to have a small impact on the dynamics. As can be inferred from the middle plot, there is a small difference between the `CosmoTransitions` solution (red) and the `BSMPTv3` solution (blue). This difference stems from the fact that thin-walled solutions extremely depend on the starting position which ultimately dictates when the field rolls down. Nevertheless, since the bounce solution minimises the Euclidean action and fulfils the Euler-Lagrange equations, we expect the action to be insensitive to small variations of the correct solution, which is indeed what we found. The relative error between both actions that is less than 0.2%. And the profile of the two solutions (lower plot) is very similar.

In the case of $f_y=80$, the vacuum phases are far apart in energy so that the starting position is not near the true vacuum, i.e. $\vec{\phi}(\rho=0)\not\approx\vec{\phi}_t$. There are differences in both the tunnelling paths (middle plot) and the profile solution (lower plot).[29] Although this is the case, the relative difference between both actions is around 1%.

The determination of the bounce action is a challenge both from a mathematical and computational point of view. The solution is highly dependent on the boundary conditions, i.e. the starting position of the field configuration. Hence, the calculation entails a numerical instability which has to be treated carefully. So it is not surprising that both codes attacking this complex problem numerically show some numerical discrepancies.

4.2. Benchmark points

For the purpose of illustrating `BSMPTv3`, we present and discuss in this section a few benchmark points. Benchmark points `BP1` and `BP2` have been chosen from an earlier publication of members of our group because they exhibit several vacuum directions and multi-step phase transitions as well as the interesting case of an intermediate charge-breaking phase at non-zero temperature. Benchmark point `BP3` has been chosen from the literature as example for flat field directions. We also comment on the results obtained with `CosmoTransitions` for each point and on differences in the results. If not explicitly stated otherwise, all our runtimes were obtained on one core of an `Apple M1 Pro` using `Clang 14.0.3` and `Python 3.9.13`.

[28] To the best of our knowledge, `CosmoTransitions` is the only other code that is capable of calculating the bounce solution and the critical as well as the nucleation temperature, where in `CosmoTransitions` the approximation of Eq. (3.33) is used.

[29] In `CosmoTransitions` the tunnelling path stops at a lower ρ value than in `BSMPTv3` due to different termination conditions in the codes.

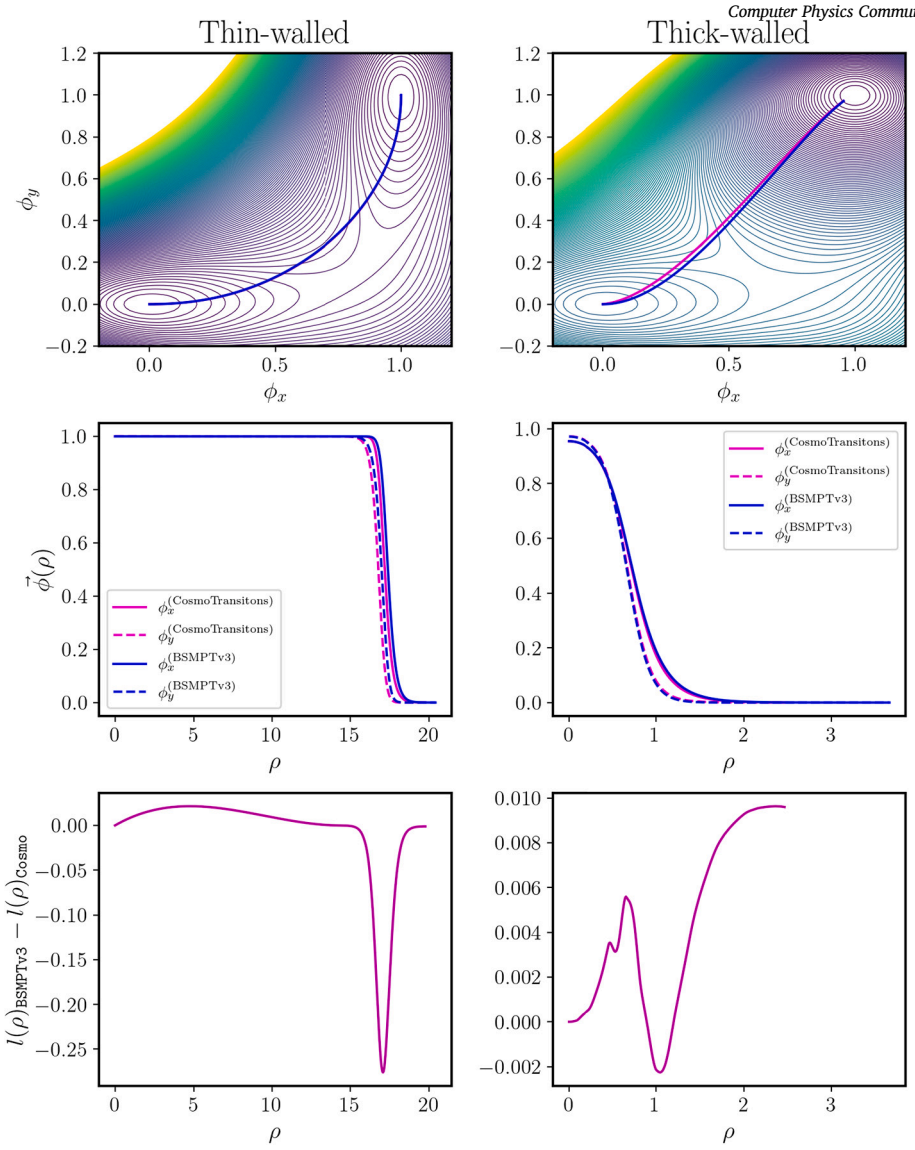

Fig. 5. Comparison between `CosmoTransitions` (red) and `BSMPTv3` (blue) for a toy model with $f_y = 2$ (left) and $f_y = 80$ (right). Upper: Potential contours in the (ϕ_y, ϕ_x) plane. The colour code denotes the potential values in arbitrary units. The lowest value is obtained at the true vacuum located at $(\phi_x, \phi_y) = (1, 1)$. Middle: Tunnelling path as a function of ρ. Lower: Difference between the tunnelling path calculated by `BSMPTv3` and `CosmoTransitions` as a function of ρ.

4.2.1. *The models*

The presented benchmark points are points of the CP-conserving 2HDM and CxSM. We briefly introduce the models to set our notation. For further details, we refer to [18,19].

The CP-conserving 2HDM In the 2HDM [234,235], the Higgs sector consists of two $SU(2)_L$ Higgs doublets Φ_1 and Φ_2. The tree-level potential with a softly broken $\mathbb{Z}_2$ symmetry, under which the doublets transform as $\Phi_1 \to \Phi_1$, $\Phi_2 \to -\Phi_2$, is given by

$$\begin{aligned} V_{\text{tree}} = {} & m_{11}^2 \Phi_1^\dagger \Phi_1 + m_{22}^2 \Phi_2^\dagger \Phi_2 - \left[m_{12}^2 \Phi_1^\dagger \Phi_2 + \text{h.c.} \right] + \frac{1}{2} \lambda_1 (\Phi_1^\dagger \Phi_1)^2 + \frac{1}{2} \lambda_2 (\Phi_2^\dagger \Phi_2)^2 \\ & + \lambda_3 (\Phi_1^\dagger \Phi_1)(\Phi_2^\dagger \Phi_2) + \lambda_4 (\Phi_1^\dagger \Phi_2)(\Phi_2^\dagger \Phi_1) + \left[\frac{1}{2} \lambda_5 (\Phi_1^\dagger \Phi_2)^2 + \text{h.c.} \right] . \end{aligned} \tag{4.2}$$

The mass parameters m_{11}^2, m_{22}^2 and m_{12}^2 and the couplings $\lambda_1 \dots \lambda_5$ are real in the CP-conserving 2HDM. Allowing in general for four VEV directions, given by the CP-even VEVs $\omega_{1,2}$ of the scalar components of the Higgs doublets, the charge-breaking VEV ω_{CB} and the CP-breaking VEV ω_{CP}, they can be parametrised in terms of the real fields ρ_i, η_i, ζ_i, and ψ_i $(i = 1, 2)$, as

$$\Phi_1 = \frac{1}{\sqrt{2}} \begin{pmatrix} \rho_1 + i\,\eta_1 \\ \zeta_1 + \omega_1 + i\,\psi_1 \end{pmatrix}, \quad \Phi_2 = \frac{1}{\sqrt{2}} \begin{pmatrix} \rho_2 + \omega_{\text{CB}} + i\,\eta_2 \\ \zeta_2 + \omega_2 + i\,(\psi_2 + \omega_{\text{CP}}) \end{pmatrix} . \tag{4.3}$$

At zero temperature, phenomenology requires that

$$\{\omega_{\text{CB}}, \omega_1, \omega_2, \omega_{\text{CP}}\}\big|_{T=0} = \{0, v_1, v_2, 0\} , \text{ with}$$

Table 2
Results for the benchmark points `BP1-BP3` (input parameters given in the main text) when tracing phases in a temperature range $T \in \{0, T_{\text{high}}\}$ GeV with `MinimaTracer` and calculating characteristic temperatures with `CalcTemps` as well as for `CosmoTransitions`, here short-named `Cosmo`. For all three benchmark points we set $T_{\text{high}} = 400$ GeV. Indices of phases and phase pairs found by `BSMPTv3` are given following the conventions of the output described in Sec. 3.6. The indices of the phases that coexist in a phase pair are given in square brackets in the format $[\texttt{i}_{\text{false}} \to \texttt{i}_{\text{true}}]$. Temperature ranges for the phases and pairs are noted in curly brackets, $\{T_{\text{low}} = 0\,\text{GeV}, T_{\text{high}}\}$ in units of GeV. Calculated characteristic temperatures are given for each phase pair, the nucleation temperature T_n from `BSMPTv3` is reported being calculated via Eq. (3.33) (first number) as well as Eq. (3.32) (second number). `history` comments on the transition history of the point, specifying the hierarchy of transitions that take place for this point. We also show runtimes for `MinimaTracer`, $t_{\texttt{MinimaTracer}}$, and for `CalcTemps`, $t_{\texttt{CalcTemps}}$, as well as the runtime for `CosmoTransitions`, $t_{\texttt{Cosmo}}$ and the respective results. Runtimes are measured on one core of an `Apple M1 Pro`. The timings for `CosmoTransitions` cover the initialisation of the model and running `findAllTransitions()`, where we decrease the epsilon used by numerical gradients `x_eps` in case the algorithm does not converge. The function also determines all transitions, calculates their critical and (approximate) nucleation temperatures and stores them in `self.TnTrans`.

	BP1	BP2	BP3
$\text{phases}_{\texttt{BSMPT}}$	0: {216, 400}	0: {0, 400}	0: {118, 400}
	1: {0, 237}	1: {0, 264}	1: {0, 133}
$\text{pairs}_{\texttt{BSMPT}}$	0: [0 → 1] {216, 237}	0: [0 → 1] {0, 264}	0: [0 → 1] {118, 133}
$t_{\texttt{MinimaTracer}}$	41.47 s	52.39 s	31.98 s
T_c	226.3	231.0	127.0
T_n	{222.9, 222.9}	{202.2, 203.5}	{122.2, 122.3}
T_p	222.6	199.0	121.8
T_f	222.6	198.4	121.8
$t_{\texttt{CalcTemps}}$	6.87 min	3.58 min	1.45 min
history	0 − (0) → 1	0 − (0) → 1	0 − (0) → 1
$\text{phases}_{\texttt{Cosmo}}$	{0, 206}	{0, 212}	{0, 135}
T_c	–	–	–
T_n	–	–	–
$t_{\texttt{Cosmo}}$	3.95 s	5.44 s	2.07 s

$$\omega_{\text{EW}}\big|_{T=0} \equiv \sqrt{\omega_1^2 + \omega_2^2 + \omega_{\text{CB}}^2 + \omega_{\text{CP}}^2}\Big|_{T=0} = \sqrt{v_1^2 + v_2^2} \equiv v = 246\ \text{GeV}\,. \tag{4.4}$$

The ratio of the zero-temperature CP-even VEVs is given by the mixing angle β as

$$\tan\beta = \frac{v_2}{v_1}\,. \tag{4.5}$$

After EWSB the Higgs spectrum consists of two scalar, $H_{1,2}$, and one pseudoscalar, A, Higgs bosons as well as a charged Higgs pair, $H^\pm$. By convention H_1 is to be taken as the lighter of the two CP-even Higgs bosons, i.e. $m_{H_1} < m_{H_2}$. In order to avoid tree-level flavour-changing neutral currents, the $\mathbb{Z}_2$ symmetry is extended to the Yukawa sectors, leading to four different types of 2HDM. The here presented benchmark points are those of the 2HDM type 1, where the doublet Φ_1 couples to all quarks and leptons.

The CxSM The Higgs potential of the CxSM [20,22,236–239] is based on the extension of the SM Higgs potential by a complex scalar singlet field $\mathbb{S}$. The tree-level potential with a softly broken global $U(1)$ symmetry is given by

$$V = \frac{m^2}{2}\Phi^\dagger\Phi + \frac{\lambda}{4}\left(\Phi^\dagger\Phi\right)^2 + \frac{\delta_2}{2}\Phi^\dagger\Phi|\mathbb{S}|^2 + \frac{b_2}{2}|\mathbb{S}|^2 + \frac{d_2}{4}|\mathbb{S}|^4 + \left(\frac{b_1}{4}\mathbb{S}^2 + a_1\mathbb{S} + c.c.\right), \tag{4.6}$$

where

$$\mathbb{S} = \frac{1}{\sqrt{2}}(S + iA) \tag{4.7}$$

is a hypercharge zero scalar field. Because of the hermicity of the potential, all parameters in Eq. (4.6) are real, except for b_1 and a_1. In our presented benchmark point, the parameters of the soft-breaking terms, written in parentheses, are set to zero, $b_1 = a_1 = 0$, so that the global $U(1)$ symmetry is exact. Denoting the electroweak VEV by ω_{EW}, and the VEVs of the CP-even and CP-odd singlet field components by ω_s and ω_a, respectively, the doublet and singlet fields can be parametrised as

$$\Phi = \frac{1}{\sqrt{2}}\begin{pmatrix} G^+ \\ \omega_{\text{EW}} + h + iG^0 \end{pmatrix}, \tag{4.8}$$

$$\mathbb{S} = \frac{1}{\sqrt{2}}\left(s + \omega_s + i\left(a + \omega_a\right)\right), \tag{4.9}$$

where G^+ and G^0 denote the charged and neutral Goldstone boson, respectively, and h is identified with the discovered SM-like Higgs boson. At $T = 0$

$$\{\omega_{\text{EW}}, \omega_s, \omega_a\}\big|_{T=0} = \{v, v_s, v_a\}\,, \quad \text{with } v = 246\ \text{GeV}\,. \tag{4.10}$$

The input parameters used by `ScannerS` are the SM VeV v, the real and imaginary parts of the complex singlet VEVs, v_s and v_a, respectively, and the potential parameters a_1, m^2, b_1, b_2, λ, δ_2, d_2.

In Table 2 all results are summarized for each benchmark point. In the following paragraphs, we show plots and discuss the points in detail.

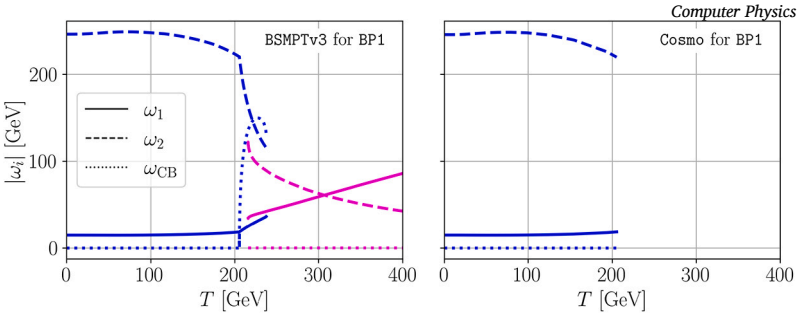

Fig. 6. `BP1`: Found phases as a function of the temperature $T \in \{0, 400\}$ GeV with `MinimaTracer` (left) and `CosmoTransitions` (right). High-temperature phase (magenta) and low-temperature phase (blue) for the three VEVs ω_1 (solid), ω_2 (dashed) and ω_{CB} (dotted). The forth VEV ω_{CP} is found to remain zero for all found phases and temperatures. Inside the low-temperature phase (in blue) found by `BSMPTv3` a second-order phase transition takes place into the electroweak phase that contains the electroweak minimum $v = 246$ GeV at $T = 0$ GeV.

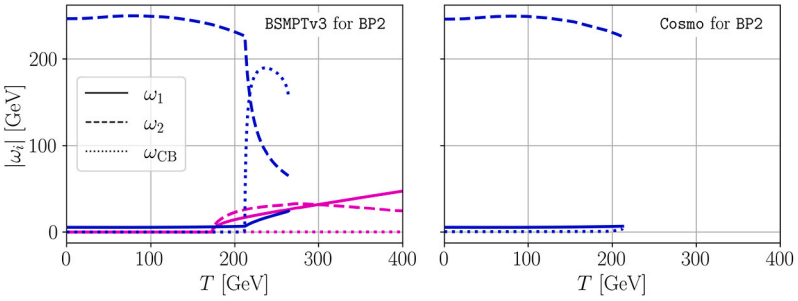

Fig. 7. `BP2`: Found phases as a function of the temperature $T \in \{0, 400\}$ GeV with `MinimaTracer` (left) and `CosmoTransitions` (right). Colour/Line code same as in Fig. 6. Inside the low-temperature phase (in blue) found by `BSMPTv3` a second-order phase transition takes place into the electroweak phase that contains the electroweak minimum $v = 246$ GeV at $T = 0$ GeV.

4.2.2. *Benchmark points `BP1` and `BP2`: multi-step phase transitions with four field directions*

Our first two benchmark points `BP1` and `BP2` are taken from [87] and are points of the CP-conserving 2HDM type 1. For both presented benchmark points, we find a multi-step phase structure in agreement with [87], and moreover, we can calculate a bounce solution and transition temperatures. The benchmark point `BP1` is defined by the following input parameter set,

$$\begin{aligned} &\texttt{BP1}\text{: type} = 1\,,\ \lambda_1 = 6.931\,,\ \lambda_2 = 0.2631\,,\ \lambda_3 = 1.287\,,\ \lambda_4 = 4.772\,,\ \lambda_5 = 4.728\,, \\ &\quad m_{12}^2 = 1.893 \times 10^4\,\text{GeV}^2\,,\ \tan\beta = 16.578\,. \end{aligned} \tag{4.11}$$

As can be inferred from Fig. 6, it features a first-order phase transition from a high-temperature neutral (magenta) to a charge-breaking (CB) phase (blue), that then transitions in a second-order phase transition back into a neutral minimum. The nucleation, percolation and completion temperatures lie close together slightly below $T = 223$ GeV and a transition history $0 \to 1$ is reported, meaning that the universe will end up in phase `1` that contains the EW minimum $v = \sqrt{\omega_1^2 + \omega_2^2}\Big|_{T=0} = 246$ GeV at $T = 0$ GeV, after the transition from the initial phase `0`. `CosmoTransitions` agrees with the found low-temperature phase until around $T = 206$ GeV and fails to trace any minima for higher temperatures. The code then terminates after $t_{\texttt{Cosmo}} = 3.95$ s with no transitions found. By increasing the upper temperature by hand, `CosmoTransitions` might, however, successfully find a transition and reproduce the phase structure found by `BSMPTv3`. E.g. we find that for $T_{\text{high}} = 900$ GeV `CosmoTransitions` confirms the results of `BSMPTv3`, however, with an increased runtime by a factor of almost 17, compared to the runtime of `CalcTemps` which also includes the calculation of the nucleation, percolation and completion temperatures.[30]

The second benchmark point `BP2` is defined by

$$\begin{aligned} &\texttt{BP2}\text{: type} = 1\,,\ \lambda_1 = 6.846\,,\ \lambda_2 = 0.2589\,,\ \lambda_3 = 1.466\,,\ \lambda_4 = 4.498\,,\ \lambda_5 = 4.450\,, \\ &\quad m_{12}^2 = 6.630 \times 10^3\,\text{GeV}^2\,,\ \tan\beta = 45.320\,. \end{aligned} \tag{4.12}$$

As can be inferred from Fig. 7, we find a first-order phase transition from the high-temperature phase (magenta lines) into the neutral low-temperature electroweak phase (blue lines) that contains the electroweak minimum at $T = 0$ GeV. This first-order phase transition happens around the same temperature as the second-order phase transition from the CB to the neutral phase, resulting in a transition history that unlike for `BP1` can never result in `BP2` undergoing a CB intermediate phase. Due to $T_p - T_c = 30$ GeV, the true minimum cools down during the CB phase and enters the neutral phase before the phase transition happens. `BP2`, similar to `BP1` can also not be traced with `CosmoTransitions` for $T_{\text{high}} = 400$ GeV, but for a choice of $T_{\text{high}} = 600$ GeV and a runtime of 4.80 min it finds a transition with $T_c = 233$ GeV and $T_n = 206$ GeV. These temperature results are then not only off by a few GeVs from the `BSMPTv3` results, but with this modified choice of T_{high}, `CosmoTransitions` also identifies three instead of two phases in the range of $T \in \{0, 400\}$ GeV. Even though, compared to `BP1`, `CosmoTransitions` reproducibly finds a transition for `BP2` if

[30] Note that `CosmoTransitions` is numerically not stable enough to be able to consistently reproduce this result.

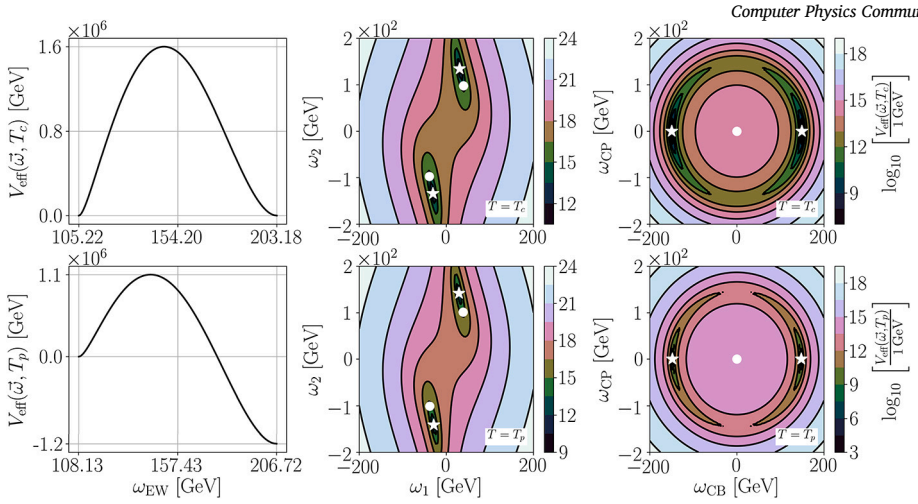

Fig. 8. BP1: Left: Slice of the effective potential from $\vec{\omega}_{\text{false}}$ to $\vec{\omega}_{\text{true}}$ at the critical temperature T_c, displayed via the coordinate of the EW VEV $\omega_{\text{EW}} \equiv \sqrt{\sum_{i=1,2,\text{CB,CP}} \omega_i^2}$. Middle and right: Two-dimensional contour slices at T_c in the $\omega_1 - \omega_2$ (middle) and $\omega_{\text{CB}} - \omega_{\text{CP}}$ (right) planes. The position of the false (true) minimum is denoted by a white dot (asterisk). Bottom: Same, but at the percolation temperature T_p. All contour plots are made with data-grids generated by `PotPlotter`. The potential is shifted such that $V_{\text{eff}}(\vec{\omega}_{\text{false}}, T) \equiv 0\,\text{GeV}$ (left column) as well as $V_{\text{eff}}(\vec{\omega}_{\text{false}}, T) \equiv 1\,\text{GeV}$ (middle and right column), respectively. The field directions which are not displayed in the two-dimensional contours are set to their global minimum coordinates.

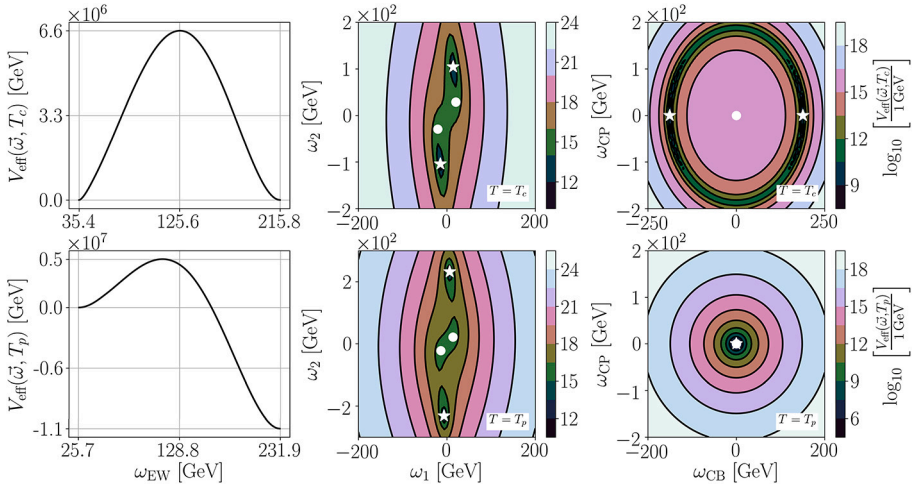

Fig. 9. Same plot as Fig. 8, but for BP2.

$T_{\text{high}} = 600\,\text{GeV}$, the phase tracing seems numerically unstable: `CosmoTransitions` is either observed to trace saddle point directions, or cannot trace the low-temperature phase around its second-order PT, resulting in it finding two unconnected phases.

To further illustrate the benchmark points, in Figs. 8 and 9 we illustrate selected potential contours at the critical and percolation temperature T_c and T_p, respectively, for BP1 and BP2. Note that because both points have $\lambda_4 \approx \lambda_5$, the potential almost exhibits an $SO(2)$ symmetry in the charge and CP-breaking VEV directions $\{\omega_{\text{CB}}, \omega_{\text{CP}}\}$, visible in Fig. 8 (right) as well as in Fig. 9 (right) by the circle in the $\{\omega_{\text{CB}}, \omega_{\text{CP}}\}$-plane which is dented in the ω_{CP}-direction inducing a non-zero ω_{CB} coordinate of the global minimum.

4.2.3. *Benchmark point BP3: dealing with flat field directions in three field directions*

For BP3 we illustrate a point of the complex singlet extension of the SM (CxSM). In terms of the CxSM input parameters, the point is defined by[31]

$$\begin{aligned} \text{BP3:}\quad & v = 246.22\,\text{GeV}\,,\ v_s = 0\,\text{GeV}\,,\ v_a = 0\,\text{GeV}\,,\ m^2 = -15\,650\,\text{GeV}^2\,, \\ & b_2 = -8859\,\text{GeV}^2\,,\ \lambda = 0.52\,,\ \delta_2 = 0.55\,,\ d_2 = 0.5\,, \\ & a_1 = 0\,\text{GeV}^3\,,\ b_1 = 0\,\text{GeV}^2\,. \end{aligned} \tag{4.13}$$

Since $b_1 = a_1 = 0$, the global $U(1)$ symmetry is exact and the potential is invariant under $v_s^2 + v_a^2$, respectively $\omega_s^2 + \omega_a^2$ at non-zero temperature. In the language of `BSMPTv3`, this means that there is a flat 2-dimensional direction in the potential. `BSMPTv3` recognizes this flat direction and without loss of generality sets $\omega_a = 0$. The resulting phase structure is shown in Fig. 10, and the point is further illustrated with contour slices in Fig. 11. We find a first-order phase transition between a high-temperature singlet phase (red) with $\sqrt{\omega_s^2 + \omega_a^2} \neq 0$ and the electroweak VEV in

[31] We took this benchmark point from [239], where it is benchmark point S2.

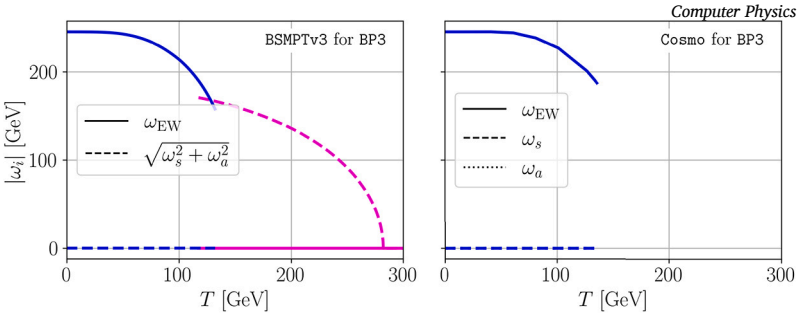

Fig. 10. `BP3`: Phase structure $|\omega_i|$ ($i = \mathrm{EW}, s, a$) as a function of the temperature T identified with `MinimaTracer` (left) and `CosmoTransitions` (right) for $T \in \{0, 300\}$ GeV. The low-temperature phase (blue) contains the electroweak minimum (solid line) at $T = 0$ GeV; the high-temperature phase (magenta) contains the singlet phase (dashed) and is only found by `MinimaTracer`.

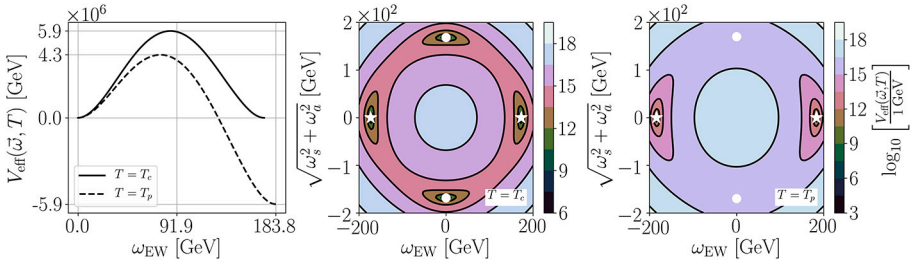

Fig. 11. `BP3`: Left: Slice of the effective potential from $\vec{\omega}_{\rm false}$ to $\vec{\omega}_{\rm true}$ at T_c (solid line) and T_p (dashed line), displayed via $\omega_{\rm EW}$. Middle and right: Two-dimensional contours at T_c (middle) and T_p (right) in the $\sqrt{\omega_s^2+\omega_a^2}-\omega_{\rm EW}$ plane. The position of the false (true) minimum is denoted by a white dot (asterisk). The potential is shifted such that $V_{\rm eff}(\vec{\omega}_{\rm false}, T) \equiv 0$ GeV (left) as well as $V_{\rm eff}(\vec{\omega}_{\rm false}, T) \equiv 1$ GeV (middle and right), respectively.

Table 3
Scan ranges for the CP-conserving 2HDM type 1 in the input parameters used by `ScannerS`.

m_{H_a} [GeV]	m_{H_s} [GeV]	m_A [GeV]	$m_{H^\pm}$ [GeV]	c_{H_sVV}	$\tan\beta$	m_{12}^2 [GeV^2]
125.09	[30, 1500]	[30, 1500]	[150, 1500]	[−0.3, 0.3]	[0.8, 25]	$[1\times10^{-3}, 5\times10^5]$

the SM field direction $\omega_{\rm EW} = 0$ (corresponding to v at $T = 0$), and the low-temperature electroweak phase (blue) with $\omega_{\rm EW} \neq 0$ and $\omega_s = \omega_a = 0$. The corresponding critical temperature is given by $T_c = 127$ GeV and the nucleation, percolation and completion temperatures lie close together at 122 GeV. `CosmoTransitions` cannot identify flat directions and is therefore forced to trace phases in all three dimensions. The code fails to find any phase above $T = 135$ GeV in the requested range of $T \in \{0, 300\}$, cf. Fig. 10 (right).

We end this section by noting that here we of course compared only three benchmark points, and in a broader comparison there may be scenarios where the comparison of the performance of the two codes `BSMPTv3` and `CosmoTransitions` may reveal different features. To get a broader view, we therefore performed a comparison based on a larger parameter sample, which we will present in the following section.

4.3. Parameter scan

For a broader comparison between `BSMPTv3` and `CosmoTransitions`, we performed a randomized parameter scan for the real, i.e. CP-conserving, 2HDM (R2HDM) type 1 by using `ScannerS-2.0.0` to check for theoretical and experimental constraints. Details can be found in [240]. Note, that for the check of the Higgs constraints in `ScannerS` the link has been updated to the recently released program packages `HiggsTools` [108]. For the scan, we chose the input parameters as those allowed by the code. They are given by the masses of the five Higgs states, the EW VEV v, the ratio of the CP-even VEVs, $\tan\beta = v_2/v_1$, the coupling c_{H_2VV} of H_2 to two massive gauge bosons $V = W^\pm, Z$, and the squared mass parameter m_{12}^2. The parameter ranges of our scan are given in Table 3.

The thus obtained theoretically and experimentally valid parameter points are then checked with respect to their phase transitions with `BSMPTv3` and independently with our `Python`-code that uses the methods of `CosmoTransitions` and traces the R2HDM potential in the full four-dimensional field space of the R2HDM that is also used in `BSMPTv3`, $\{\omega_{\rm CB}, \omega_1, \omega_2, \omega_{\rm CP}\}$.

In Fig. 12 (left) we show a histogram of the runtimes of `BSMPTv3` versus `CosmoTransitions`. The points taken into account are a subset of the full parameter sample, for which both codes find the same transitions.[32] Runtimes are measured by running the codes on a mixture of `Intel Xeon` and `AMD EPYC` processors with `Python 3.6.15` for `CosmoTransitions`. The runtime for `BSMPTv3` is derived for running `CalcTemps` which traces all found phases and determines their critical temperatures, bounce solutions, nucleation, percolation, and completion temperatures for all found phase pairs. The runtime of the `CosmoTransitions` routines is for initializing the model and running the `findAllTransitions()` method that calculates the critical and approximate nucleation temperatures for all found transitions. We find `BSMPTv3` to be up to 10^3 faster with a mean (median) runtime of 4.15 min (3.47 min). For `CosmoTransitions` we find a mean (median) runtime of 41.46 min (5.61 min). If we only take into

[32] If the number of found transitions differs between the two codes, the runtime comparison gets biased towards the code that finds less transitions. In that case, a direct runtime comparison would be biased towards the potentially less accurate code.

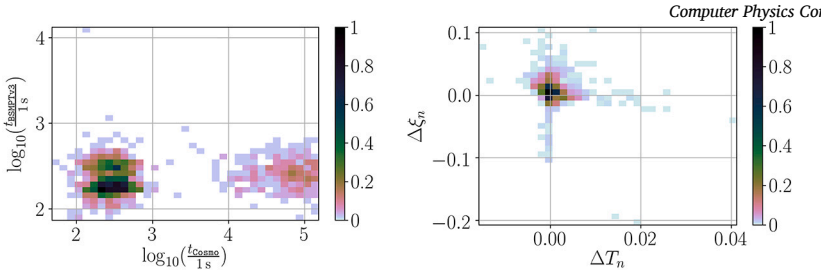

Fig. 12. Left: Two-dimensional histogram showing the runtime of BSMPTv3 versus the runtime of CosmoTransitions for the sample for which both codes identify the same phase transitions. Right: Two-dimensional histogram of the relative difference in ξ at the nucleation temperature determined via the approximate condition of Eq. (3.33) versus the relative difference in the approximate nucleation temperature for the same sample. The colour of the bin indicates the proportion of the points falling into it.

account points for which BSMPTv3 and CosmoTransitions each only find one transition, their mean (median) runtimes are 4.10 min (3.28 min) for BSMPTv3 and 3.89 h (5.60 min) for CosmoTransitions.

While improvements of the runtime are of course desirable, the determined temperatures of the phase transitions are the quantities interesting for physics. In the following, we compare the values of the temperatures and of the VEV-to-temperature ratios found by the two codes, as well as the associated runtimes. This can be done in a meaningful way only for parameter points where both codes find reliable results. Defining the respective relative difference in the critical and approximate nucleation temperatures found by BSMPTv3 and CosmoTransitions as ($i = c, n$)

$$\Delta T_i = \frac{\left(T_i^{\text{BSMPTv3}} - T_i^{\text{Cosmo}}\right)}{T_i^{\text{BSMPTv3}}}\,, \tag{4.14}$$

we find for the subset of points, in which both codes find the same transitions, a maximal relative deviation of 2.7 % in the critical temperature with mean (median) relative differences of 0.07 % (0.003 %). We define the ratio between the electroweak VEV $v(T_i)$ at the temperature T_i and the temperature T_i as ξ_i,

$$\xi_i = \frac{\sqrt{\sum_k \omega_k^2(T_i)}}{T_i} \quad \text{with} \quad \omega_k \in \{\omega_{\text{CB}}, \omega_1, \omega_2, \omega_{\text{CP}}\}\,, \tag{4.15}$$

and the relative difference $\Delta\xi_i$ in ξ_i found by BSMPTv3 and CosmoTransitions as

$$\Delta\xi_i = \frac{\left(\xi_i^{\text{BSMPTv3}} - \xi_i^{\text{Cosmo}}\right)}{\xi_i^{\text{BSMPTv3}}}\,. \tag{4.16}$$

In Fig. 12 (right) we show the relative differences $\Delta\xi_n$ versus the relative differences ΔT_n in the found approximate nucleation temperature. We find mean and median for both relative differences below 1 %, however, we see outliers of up to 4.1 % in ΔT_n as well as of up to −20.7 % in $\Delta\xi_n$. The outliers in $\Delta\xi_n$ are correlated with a rapidly changing potential in a small temperature interval. Small ΔT_n in that case can lead to larger $\Delta\xi_n$ if the position of the electroweak minimum changes significantly in small temperature ranges.

5. Conclusions

The detection of gravitational waves from first-order phase transitions during the evolution of the universe combines cosmological observation with particle physics in an exciting way that may answer some of our most urgent open questions: What is the true theory underlying nature? And how can we explain the observed matter-antimatter asymmetry? For this to be meaningful, we need to go through the whole chain from a particle physics model to the possible detection of gravitational waves sourced by FOPTs at future space-based interferometers like LISA, taking into account the state-of-the-art approaches to the various involved steps along this way. At present, there exists no public code that is able to perform this task. With the publication of the C++ code BSMPTv3 we close this gap. It is the first publicly available code that performs the whole chain from the particle physics model to the gravitational wave spectrum.

The code BSMPTv3 is based on the extension of the previous versions BSMPTv1 and v2, which calculate the loop-corrected effective potential at non-zero temperature in the on-shell renormalization scheme, including thermal masses, for extended Higgs sectors, to search for FOPTs. The new release BSMPTv3 is able to trace vacuum phases as functions of the temperature for complicated vacuum histories, involving also multi-step PTs. It is able to treat multiple phase directions, discrete symmetries and flat directions and to identify EW symmetry non-restoration at high temperature. After tracing the minima, the bounce action is computed and the bounce equation is solved for phase pairs exhibiting a critical temperature. This then allows to evaluate the tunnelling rate from the false to the true vacuum and to determine the nucleation temperature, and thereby to decide if the universe is trapped in a vacuum or if a phase transition actually takes place. In this case, the code also calculates the percolation and the completion temperature. Subsequently, the latent heat release and the inverse time scale characteristic for a phase transition are evaluated at the transition temperature, which by default is set to the percolation temperature, but can also be chosen by the user. Together with the wall velocity, for which various approximations are implemented among which the user can choose, the thermal parameters are used to calculate the GW spectrum sourced from bubble collisions and highly relativistic fluid shells, sound waves and turbulence. Lastly, the signal-to-noise ratio at LISA is evaluated.

We compared our code with CosmoTransitions and found good agreement between both codes, but showed that BSMPTv3 not only can be significantly faster, but also is more powerful in dealing with higher-dimensional potentials.

The code is publicly available and can be downloaded at:

https://github.com/phbasler/BSMPT.

It will constantly be upgraded to include new developments in the field and newly published improved calculations related to the various steps.

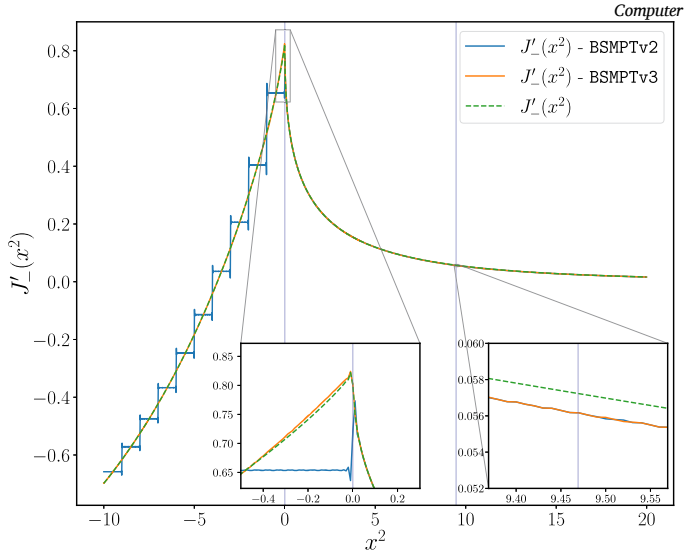

Fig. 13. Derivative $J'_-(x^2)$ of the bosonic thermal function as a function of x. We compare the implementation of `BSMPTv2` (blue line) and `BSMPTv3` (orange) as well as a precise numerical evaluation of the integral (green dashed line). The blue vertical lines, at $x^2 = 0$ and $x^2 = -9.4692$, are the positions where we patch different implementations of $J_-(x^2)$ together, cf. [18] for more details.

With the `C++` code `BSMPTv3` we provide an important contribution to the reliable derivation of gravitational wave signals from FOPTs of BSM Higgs sectors with several vacuum directions. Its application to the broad new physics landscape will provide an exciting field for the exploration and understanding of the Higgs vacuum structure and will advance our knowledge on the true model underlying nature.

CRediT authorship contribution statement

Lisa Biermann: Writing – review & editing, Writing – original draft, Visualization, Validation, Software, Resources, Methodology, Investigation, Formal analysis, Conceptualization. **Margarete Mühlleitner:** Writing – review & editing, Writing – original draft, Supervision, Project administration, Methodology, Funding acquisition, Conceptualization. **Rui Santos:** Writing – review & editing, Supervision, Project administration, Methodology, Funding acquisition, Conceptualization. **João Viana:** Writing – review & editing, Writing – original draft, Visualization, Validation, Software, Resources, Methodology, Investigation, Formal analysis, Data curation, Conceptualization.

Declaration of competing interest

The authors declare that they have no known competing financial interests or personal relationships that could have appeared to influence the work reported in this paper.

Acknowledgements

LB wants to thank Thomas Biekötter and Christoph Borschensky for helpful discussions about the code. Many thanks to Karo Erhardt and Guilherme Monsanto for testing early versions of `BSMPTv3`. MM and LB acknowledge support by the Deutsche Forschungsgemeinschaft (DFG, German Research Foundation) under grant 396021762 - TRR 257. RS and JV are supported by CFTC-UL under FCT contracts https://doi.org/10.54499/UIDB/00618/2020, https://doi.org/10.54499/UIDP/00618/2020 as well as by the projects CERN/FIS-PAR/0025/2021 and CERN/FIS-PAR/0021/2021. JV is also supported by a PT-CERN PhD Grant, contract PRT/BD/154191/2022.

Appendix A. Improvement of the bosonic thermal function $J_-(x^2)$

To solve the bounce equation, it is very important for the potential and its gradient to behave properly, without any discontinuities and/or unexpected behaviours. In the previous versions, `BSMPTv1` and `BSMPTv2`, where all observables were calculated without the use of the gradient, its behaviour was not critical.

The biggest problem arises from the evaluation of the bosonic thermal function $J_-(x^2)$ at negative input values. In the previous versions, the function values at $x^2 = \{0, -1, -2, \cdots, -3000\}$ were hard-coded, and to calculate the function value at a negative x-value a linear interpolation between the two closest nodes was used. In the past, this was more than enough as the derivative was never used and this interpolation produced a continuous $J_-(x^2)$ function. To solve the bounce equation we also need the derivative to be well-behaved. Our solution for this is the construction of a cubic spline using the same hard-coded function values shipped with the previous versions. We also imposed that the spline derivative at $x^2 = 0$ matches the analytical value of $J'_-(0) = -\frac{\pi^2}{12}$. The result can be see in Fig. 13 where we plot the derivative of $J_-(x^2)$ at negative values for `BSMPTv2` (blue) and `BSMPTv3` (orange) as well as a numerical derivative calculated with high precision (green dashed). The new solution in `BSMPTv3` approximates the derivative of the function at negative values much better.

It is important to check that this change does not completely alter the results found in previous calculations. We therefore re-scanned some points of the R2HDM and its CP-violating version, the C2HDM, applying both implementations of $J_-(x^2)$. We found that the difference is a few per-cent only. Overall, the critical temperature calculated before is above the critical temperature calculated in `BSMPTv3`. In the old version, $\xi_c = \omega_{\rm EW}(T_c)/T_c$ is slightly lower (by at most 0.1). The previously obtained results were hence a little bit more conservative.

Appendix B. Comparison with Espinosa-Konstandin analytical solutions

Recently, a way of finding an analytical solution for the bounce equation was developed in [241,242]. The potentials/solutions used throughout this section assume an $\mathcal{O}(4)$ symmetry although similar expression can be constructed for $\mathcal{O}(3)$-symmetric solutions. The method consists on defining the tunnelling potential

$$V_t(\phi) \equiv V(\phi) - \frac{1}{2}\dot{\phi}_b^2\,, \tag{B.1}$$

where the subscript "b" indicates bounce, to clarify that the tunnelling potential is only defined along the tunnelling path. The tunnelling potential is simply the negative value of the energy that is not conserved, hence

$$\frac{d}{d\rho}\left[\frac{1}{2}\dot{\phi}_b^2 - V(\phi_b)\right] = -\frac{3}{\rho}\dot{\phi}_b^2 \leq 0\,, \tag{B.2}$$

so that the tunnelling potential describes how energy is dissipated by the drag term. The Euler-Lagrange equations provide a differential equation,

$$\left(4V_t' - 3V'\right)V_t' = 6\left(V_t - V\right)V_t''\,, \tag{B.3}$$

where the prime denotes the derivative w.r.t. ϕ. The Euclidean action of the bounce solution can then be calculated as

$$S_E\left[V_t\right] = 54\pi^2 \int_{\phi_0}^{\phi_+} \frac{(V - V_t)^2}{(V_t')^3} d\phi\,, \tag{B.4}$$

where $\phi_0 \equiv \phi(\rho = 0)$ and ϕ_+ is the false vacuum. The Euclidean action can have an analytical expression provided that V and V_t are simple enough for the integral to be solvable but, even if the integral is not solvable, it can usually be calculated numerically with sufficient accuracy.

This method provides a way to produce analytical solutions. To solve the bounce equation one would use $V(\phi)$ to calculate $V_t(\phi)$, but we can start with $V_t(\phi)$ and calculate the $V(\phi)$ that solves Eq. (B.3), something that is far easier to do. The potential can be calculated from the tunnelling potential as

$$V(\phi) = V_t(\phi) + \frac{V_t'(\phi)^2}{3}\int_{\phi_0}^{\phi} \frac{d\overline{\phi}}{V_t'(\overline{\phi})}\,. \tag{B.5}$$

Therefore, given a tunnelling potential $V_t(\phi)$ and a wanted solution ϕ_0 one could construct the potential $V(\phi)$ that has this solution. This method allows one to manufacture potentials, and their respective solutions, that then can be used to test other methods. With this in mind, we compared the examples provided in Ref. [242] to verify the accuracy of our code. The results are provided here below.

B.1. Example A

We consider a tunnelling potential given by

$$V_t(\phi) = \phi^2(2\phi - 3)\,, \tag{B.6}$$

which produces the following potential

$$V(\phi) = \phi^2\left[2\phi - 3 + (1-\phi)^2 \log\frac{(1-\phi)^2\phi_0^2}{(1-\phi_0)^2\phi^2}\right]\,, \tag{B.7}$$

with $0 < \phi_0 < 1$ and $\phi_0 \equiv \phi(\rho = 0)$ being the solution for the bounce. The value for the action is given by

$$S(\phi_0) = -\frac{\pi^2}{3}\left[\phi_0 + \mathrm{Li}_2\left(\frac{\phi_0}{\phi_0 - 1}\right)\right]\,, \tag{B.8}$$

where $\mathrm{Li}_2(x)$ is the dilogarithm. For the value of $\phi_0 = 0.99$, the result of `BSMPTv3` matches the analytical result with a 0.0007% error. For the value of $\phi_0 = 0.50$, the result of `BSMPTv3` matches the analytical result with a 0.07% error.

B.2. Example B

We consider a tunnelling potential given by

$$V_t(\phi) = -\sin^2\phi\,, \tag{B.9}$$

which produces the following potential

$$V = \left[-1 + \frac{2}{3}\cos^2\phi \log\left(\frac{\tan\phi_0}{\tan\phi}\right)\right]\sin^2\phi\,, \tag{B.10}$$

with $0 < \phi_0 < \pi/2$. For the value of $\phi_0 = 1.4$, the result of `BSMPTv3` matches the analytical result with a 0.002% error. For the value of $\phi_0 = 1.54$, the result of `BSMPTv3` matches the analytical result with a 0.0003% error.

B.3. Example C

We consider a tunnelling potential given by

$$V_t(\phi) = \frac{\phi^2}{-1/2 + \log\phi}\,, \tag{B.11}$$

which produces the following potential

$$V(\varphi) = \frac{\phi^2}{-1/2+\log\phi} + \frac{8\phi^2(1-\log\phi)^2}{3(1-2\log\phi)^2}\left(2\log^2\phi - 2\log^2\phi_0 + \log\frac{1-\log\phi}{1-\log\phi_0}\right), \tag{B.12}$$

with $0 < \phi_0 < \sqrt{e}$. For the value of $\phi_0 = 0.8$, the result of `BSMPTv3` matches the analytical result with a 0.004% error.

B.4. Example D

We consider a tunnelling potential given by

$$V_t(\phi) = \mathrm{Ei}(2\log\phi)\,, \tag{B.13}$$

which produces the following potential

$$V(\varphi) = \mathrm{Ei}(2\log\phi) + \frac{1}{6}\phi^2\left(1 - \frac{\log^2\phi_0}{\log^2\phi}\right), \tag{B.14}$$

with $0 < \phi_0 < 1$. For the value of $\phi_0 = 0.8$, the result of `BSMPTv3` does not match the analytical solution. Instead, we find a tunnelling solution around $\phi_0 \approx 0.5323$, that can be checked using the undershoot/overshoot algorithm around this point. From Ref. [242], the analytical solution for this potential also has an explicit form for the $\phi_0 = 0.8$ solution, which is given by

$$\phi_B(\rho,\phi_0) = e^{-\sqrt{\rho^2/3+\log^2\phi_0}}\,. \tag{B.15}$$

If we use the analytical solution starting at a different starting point $\tilde{\phi}_0$, the Euler-Lagrange equations give

$$\left(\log^2(\phi_0) - \log^2(\tilde{\phi}_0)\right)\frac{\left(\sqrt{3\log^2(\tilde{\phi}_0)+\rho^2}+\sqrt{3}\right)}{\left(3\log^2(\tilde{\phi}_0)+\rho^2\right)^{3/2}}e^{-\frac{\sqrt{3\log^2(\tilde{\phi}_0)+\rho^2}}{\sqrt{3}}} = 0\,, \tag{B.16}$$

which is only realized for all $\rho \geq 0$ if $\phi_0 = \tilde{\phi}_0$.[33] This result indicates that there are two bounce solutions with different functionals, i.e. only one of the solutions is given by Eq. (B.15).

B.5. Example E

We consider a tunnelling potential given by

$$V_t = e^2\,\mathrm{Ei}(-2+2\log\phi) - e^3\,\mathrm{Ei}(-3+3\log\phi)\,, \tag{B.17}$$

which produces the following potential

$$V(\phi) = e^2\,\mathrm{Ei}(-2+2\log\phi) - e^3\,\mathrm{Ei}(-3+3\log\phi) + \frac{(1-\phi)^2\phi^2}{18(1-\log\phi)^2}r^2(\phi)\,, \tag{B.18}$$

where $r^2(\phi)$ is the bounce profile implicitly given by

$$r^2(\phi) = 3\left[2\log\frac{(1-\phi)\phi_0}{(1-\phi_0)\phi} + \log^2\phi - \log^2\phi_0 + 2\,\mathrm{Li}_2(1-\phi) - 2\mathrm{Li}_2\left(1-\phi_0\right)\right]. \tag{B.19}$$

For the value of $\phi_0 = 0.8$, the result of `BSMPTv3` matches the analytical result with a 0.0006% error.

B.6. 2-Dimensional example

There is a way to handle n-dimensional potentials. The method is described in detail in Ref. [242]. The tunnelling potential, that we consider here is the same as in example A. The 2-dimensional potential is given by

$$V_2\left(\phi_1,\phi_2\right) = V\left(\varphi\left(\phi_1\right)\right) + W\left(\phi_1\right)\left[\phi_2 - \Phi_2\left(\phi_1\right)\right] + \frac{9}{2}\left(2-\phi_1\right)\left(\phi_2^2 - \phi_1^2 - 1\right)^2\,, \tag{B.20}$$

where $\varphi(\phi_1) = -i\,\mathrm{E}\left[i\,\mathrm{Arcsinh}(\phi_1), 2\right]$ with $E[\phi, m]$ being the incomplete elliptic function of the second kind. The function $W(\phi_1)$ is given by

[33] There is another solution $1/\phi_0$ that fulfils the Euler-Lagrange equation but it lies outside the range $0 < \phi_0 < 1$.

$$W(\phi_1) = V'\left(\varphi(\phi_1)\right)\tanh\left(\phi_1/\alpha\right) + \frac{2[V\left(\varphi(\phi_1)\right) - V_t\left(\varphi(\phi_1)\right)]}{\alpha\cosh\left(\phi_1/\alpha\right)^3}\,. \tag{B.21}$$

The parameter α is free and generates different tunnelling paths, we set it to $\alpha = 1/2$ to match Ref. [242]. For $\phi_0 = 0.8$, the result of `BSMPTv3` matches the analytical result with a 1.5% error.

B.7. 3-Dimensional example

The tunnelling potential is the same as in example A and in the 2-dimensional example. The 3-dimensional potential is given by

$$V_3\left(\phi_1,\phi_2,\phi_3\right) = V\left(\varphi\left(\phi_1\right)\right) + W_2\left(\phi_1\right)\left(\phi_2 - \Phi_2\left(\phi_1\right)\right) + W_3\left(\phi_1\right)\left(\phi_3 - \Phi_3\left(\phi_1\right)\right) \tag{B.22}$$

$$+ 25\left(\phi_2 - \Phi_2\left(\phi_1\right)\right)^2 + 25\left(\phi_3 - \Phi_3\left(\phi_1\right)\right)^2\,, \tag{B.23}$$

where $\Phi_2(\phi_1)$ and $\Phi_3(\phi_1)$ are given by

$$\Phi_2\left(\phi_1\right) = \rho\sin\left(\frac{\sqrt{1-\alpha^2}}{\rho\alpha}\phi_1\right), \quad \Phi_3\left(\phi_1\right) = \rho - \rho\cos\left(\frac{\sqrt{1-\alpha^2}}{\rho\alpha}\phi_1\right), \tag{B.24}$$

and the $W_{1/2}$ functions are given by

$$W_2\left(\phi_1\right) = V'\left(\varphi\left(\phi_1\right)\right)\frac{\Phi_2'\left(\phi_1\right)}{\varphi'\left(\phi_1\right)} + 2\left[V\left(\varphi\left(\phi_1\right)\right) - V_t\left(\varphi\left(\phi_1\right)\right)\right]\left[\frac{\Phi_2''\left(\phi_1\right)}{\varphi'\left(\phi_1\right)^2} - \frac{\Phi_2'\left(\phi_1\right)\varphi''\left(\phi_1\right)}{\varphi'\left(\phi_1\right)^3}\right], \tag{B.25}$$

$$W_3\left(\phi_1\right) = V'\left(\varphi\left(\phi_1\right)\right)\frac{\Phi_3'\left(\phi_1\right)}{\varphi'\left(\phi_1\right)} + 2\left[V\left(\varphi\left(\phi_1\right)\right) - V_t\left(\varphi\left(\phi_1\right)\right)\right]\left[\frac{\Phi_3''\left(\phi_1\right)}{\varphi'\left(\phi_1\right)^2} - \frac{\Phi_3'\left(\phi_1\right)\varphi''\left(\phi_1\right)}{\varphi'\left(\phi_1\right)^3}\right]. \tag{B.26}$$

The parameters α and ρ are free and generate different tunnelling paths. We choose $\alpha = 1/2$ and $\phi_0 = 0.999$ to match Ref. [242]. We chose two values of ρ. When setting it to $\rho = \frac{1}{6}$, `BSMPTv3` matches the analytical result with a 1.5% error. If we set it to $\rho = \frac{1}{8}$, the same value as in Ref. [242], then `BSMPTv3` converges to a different solution with an Euclidean action of $S \approx 55.6$.

Appendix C. Effective degrees of freedom for the energy and entropy

At the early stages of the Universe, when the temperature was larger than $\mathcal{O}(100\text{GeV})$, the cosmic fluid was dense and hot enough that the interaction rate of the particles with the fluid was much larger than the Hubble rate so that the Universe was fully thermalised [195]. Therefore, all particles fulfilled their respective equilibrium distribution functions, i.e. the Bose-Einstein distribution for bosons and the Fermi-Dirac distribution for fermions. The cosmic fluid energy density and the entropy density can hence be calculated just by knowing what type of particles is present in the cosmic fluid. For each massless (relativistic) boson (b) and fermion (f) there is a contribution (in natural units) to the energy (ρ) and entropy (s) density of

$$\rho_\text{b}(T) = g\frac{\pi^2}{30}T^4\,, \qquad \rho_\text{f}(T) = \frac{7}{8}g\frac{\pi^2}{30}T^4\,, \tag{C.1}$$

$$s_\text{b}(T) = g\frac{2\pi^2}{45}T^3\,, \qquad s_\text{f}(T) = \frac{7}{8}g\frac{2\pi^2}{45}T^3\,, \tag{C.2}$$

where g are the internal degrees of freedom of the particle. To obtain the complete energy and entropy density, respectively, one simply has to sum over all particles in thermal equilibrium,

$$\rho(T) = \frac{\pi^2}{30}\left(\sum_{i\in\{\text{boson}\}} g_i^{(\rho)} + \frac{7}{8}\sum_{i\in\{\text{fermion}\}} g_i^{(\rho)}\right)T^4 = \frac{\pi^2}{30}g^{(\rho)}(T)T^4\,, \tag{C.3}$$

$$s(T) = \frac{2\pi^2}{45}\left(\sum_{i\in\{\text{boson}\}} g_i^{(s)} + \frac{7}{8}\sum_{i\in\{\text{fermion}\}} g_i^{(s)}\right)T^3 = \frac{2\pi^2}{45}g^{(s)}(T)T^3\,. \tag{C.4}$$

As the Universe cools down and expands, particles gain mass which decreases their contribution to the energy/entropy density of the cosmic fluid. Additionally, their interaction rate with the fluid decreases until the particle decouples from the cosmic fluid, which further decreases the energy/entropy density of the fluid. For this reason, it is customary to promote the $g_i^{(\rho/s)}$ in Eq. (C.3) and Eq. (C.4) to temperature dependent quantities and call the sum the effective degrees of freedom for the energy density and entropy density, respectively, i.e. $g^{(\rho)}(T)$ and $g^{(s)}(T)$.

For the scope of this paper, we make the approximation that the effective number of degrees of freedom for energy and entropy is the same, i.e. $g^{(\rho)}(T) \approx g^{(s)}(T)$, which we then denote as $g(T)$. This should be a good approximation until $T = 100\,\text{keV}$ [195]. In the end, we have that

$$g(T) = \sum_{i\in\{\text{boson}\}} g_i^{(\rho/s)}(T) + \frac{7}{8}\sum_{i\in\{\text{fermion}\}} g_i^{(\rho/s)}(T)\,, \tag{C.5}$$

where we assumed that the sum is the same for the energy and entropy degrees of freedom.

The effective degrees of freedom $g(T)$ have been calculated for the SM in detail, but for a generic model, the temperature dependence is non-trivial to compute. At high temperature, when we assume that all particles are thermalised and relativistic, we can calculate $g(T\to\infty) \equiv g(\infty)$, and it is given by the sums in Eq. (C.3) and (C.4).

To incorporate this in our code, $g(T)$ is calculated using an approximation by interpolating the SM effective degrees of freedom $g^{(\text{SM})}(T)$ and the correct value for a generic model in the relativistic limit $g(\infty)$. In our approximation, we assume that all additional fields decouple before the

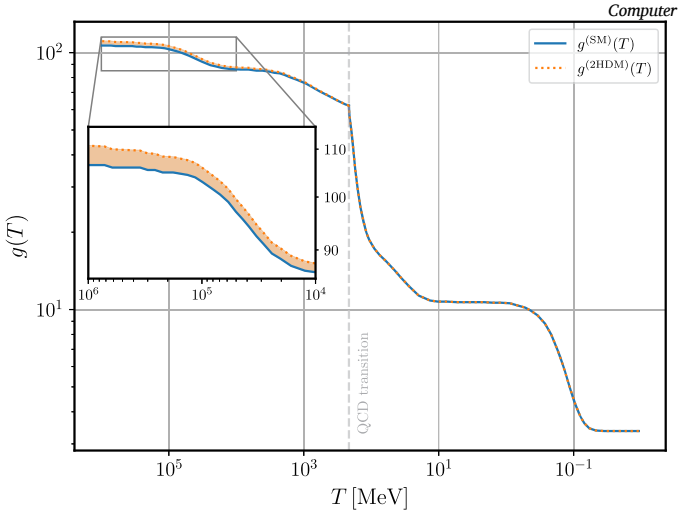

Fig. 14. Approximation used by `BSMPTv3` to estimate the effective degrees of freedom $g(T)$ for a generic model, here the 2HDM. The blue line represents the SM effective degrees of freedom $g^{(\mathrm{SM})}$ (with $g^{(\mathrm{SM})}(\infty) = 106.75$), the orange dotted line represents the 2HDM effective degrees of freedom $g^{(\mathrm{2HDM})}(T)$ (with $g^{(\mathrm{2HDM})}(\infty) = 110.75$), and the orange shaded region visualizes the change due to the additional degrees of freedom that the 2HDM has compared to the SM. The grey dashed vertical line at $T = 214\,\mathrm{MeV}$ is the temperature of the QCD phase transition where we assume that all additional particles have decoupled and we fall back to $g^{(\mathrm{SM})}$.

QCD transition at $T_{\mathrm{QCD}} = 214\,\mathrm{MeV}$, and we make a smooth interpolation between the QCD transition and $T_{\mathrm{h}} = 1\,\mathrm{TeV}$, the temperature at which we assume all particles are relativistic and thermalised. Explicitly, the approximation is given by

$$g(T) = \begin{cases} g(\infty), & \text{for } T \geq T_{\mathrm{h}} \\ (T/T_{\mathrm{QCD}})^{\log(g(\infty)/g^{(\mathrm{SM})}(T_{\mathrm{h}}))/\log(T_{\mathrm{h}}/T_{\mathrm{QCD}})}\, g^{(\mathrm{SM})}(T), & \text{for } T_{\mathrm{h}} > T > T_{\mathrm{QCD}} \\ g^{(\mathrm{SM})}(T), & \text{for } T_{\mathrm{QCD}} \geq T\,. \end{cases} \tag{C.6}$$

To show the effect of the additional degrees of freedom of the 2HDM, which has four more effective degrees of freedom at high temperature (one for each spin-zero boson), in comparison to the SM, we plot both $g^{(\mathrm{SM/2HDM})}$ in Fig. 14 where the shaded area represents the change due to the additional degrees of freedom of the additional fields.

Data availability

Data will be made available on request.

References

[1] Georges Aad, et al., Observation of a new particle in the search for the Standard Model Higgs boson with the ATLAS detector at the LHC, Phys. Lett. B 716 (2012) 1–29, https://doi.org/10.1016/j.physletb.2012.08.020, arXiv:1207.7214 [hep-ex].
[2] Serguei Chatrchyan, et al., Observation of a new boson at a mass of 125 GeV with the CMS experiment at the LHC, Phys. Lett. B 716 (2012) 30–61, https://doi.org/10.1016/j.physletb.2012.08.021, arXiv:1207.7235 [hep-ex].
[3] C.L. Bennett, et al., Nine-year Wilkinson microwave anisotropy probe (WMAP) observations: final maps and results, Astrophys. J. Suppl. Ser. 208 (2013) 20, https://doi.org/10.1088/0067-0049/208/2/20, arXiv:1212.5225 [astro-ph.CO].
[4] V.A. Kuzmin, V.A. Rubakov, M.E. Shaposhnikov, On the anomalous electroweak baryon number nonconservation in the early universe, Phys. Lett. B 155 (1985) 36, https://doi.org/10.1016/0370-2693(85)91028-7.
[5] Andrew G. Cohen, David B. Kaplan, Ann E. Nelson, Baryogenesis at the weak phase transition, Nucl. Phys. B 349 (1991) 727–742, https://doi.org/10.1016/0550-3213(91)90395-E.
[6] Andrew G. Cohen, D.B. Kaplan, A.E. Nelson, Progress in electroweak baryogenesis, Annu. Rev. Nucl. Part. Sci. 43 (1993) 27–70, https://doi.org/10.1146/annurev.ns.43.120193.000331, arXiv:hep-ph/9302210 [hep-ph].
[7] M. Quiros, Field theory at finite temperature and phase transitions, Helv. Phys. Acta 67 (1994) 451–583.
[8] V.A. Rubakov, M.E. Shaposhnikov, Electroweak baryon number nonconservation in the early universe and in high-energy collisions, Usp. Fiz. Nauk 166 (1996) 493–537, Phys. Usp. 39 (1996) 461, https://doi.org/10.1070/PU1996v039n05ABEH000145, arXiv:hep-ph/9603208 [hep-ph].
[9] Koichi Funakubo, CP violation and baryogenesis at the electroweak phase transition, Prog. Theor. Phys. 96 (1996) 475–520, https://doi.org/10.1143/PTP.96.475, arXiv:hep-ph/9608358 [hep-ph].
[10] Mark Trodden, Electroweak baryogenesis, Rev. Mod. Phys. 71 (1999) 1463–1500, https://doi.org/10.1103/RevModPhys.71.1463, arXiv:hep-ph/9803479 [hep-ph].
[11] Werner Bernreuther, CP violation and baryogenesis, Lect. Notes Phys. 591 (2002) 237–293, arXiv:hep-ph/0205279 [hep-ph].
[12] David E. Morrissey, Michael J. Ramsey-Musolf, Electroweak baryogenesis, New J. Phys. 14 (2012) 125003, https://doi.org/10.1088/1367-2630/14/12/125003, arXiv:1206.2942 [hep-ph].
[13] A.D. Sakharov, Violation of CP invariance, C asymmetry, and baryon asymmetry of the universe, Pis'ma Zh. Eksp. Teor. Fiz. 5 (1967) 32–35, Usp. Fiz. Nauk 161 (5) (1991) 61, https://doi.org/10.1070/PU1991v034n05ABEH002497.
[14] K. Kajantie, et al., Is there a hot electroweak phase transition at $m_H \gtrsim m_W$?, Phys. Rev. Lett. 77 (1996) 2887–2890, https://doi.org/10.1103/PhysRevLett.77.2887, arXiv:hep-ph/9605288.
[15] F. Csikor, Z. Fodor, J. Heitger, Endpoint of the hot electroweak phase transition, Phys. Rev. Lett. 82 (1999) 21–24, https://doi.org/10.1103/PhysRevLett.82.21, arXiv:hep-ph/9809291.
[16] B.P. Abbott, et al., Observation of gravitational waves from a binary black hole merger, Phys. Rev. Lett. 116 (6) (2016) 061102, https://doi.org/10.1103/PhysRevLett.116.061102, arXiv:1602.03837 [gr-qc].
[17] Carroll L. Wainwright, CosmoTransitions: computing cosmological phase transition temperatures and bubble profiles with multiple fields, Comput. Phys. Commun. 183 (2012) 2006–2013, https://doi.org/10.1016/j.cpc.2012.04.004, arXiv:1109.4189 [hep-ph].
[18] Philipp Basler, Margarete Mühlleitner, BSMPT (beyond the standard model phase transitions): a tool for the electroweak phase transition in extended Higgs sectors, Comput. Phys. Commun. 237 (2019) 62–85, https://doi.org/10.1016/j.cpc.2018.11.006, arXiv:1803.02846 [hep-ph].

[19] Philipp Basler, Margarete Mühlleitner, Jonas Müller, BSMPT v2 a tool for the electroweak phase transition and the baryon asymmetry of the universe in extended Higgs sectors, Comput. Phys. Commun. 269 (2021) 108124, https://doi.org/10.1016/j.cpc.2021.108124, arXiv:2007.01725 [hep-ph].
[20] Rita Coimbra, Marco O.P. Sampaio, Rui Santos, ScannerS: constraining the phase diagram of a complex scalar singlet at the LHC, Eur. Phys. J. C 73 (2013) 2428, https://doi.org/10.1140/epjc/s10052-013-2428-4, arXiv:1301.2599 [hep-ph].
[21] P.M. Ferreira, et al., Wrong sign and symmetric limits and non-decoupling in 2HDMs, J. High Energy Phys. 12 (2014) 067, https://doi.org/10.1007/JHEP12(2014)067, arXiv:1409.6723 [hep-ph].
[22] Raul Costa, et al., Singlet extensions of the standard model at LHC run 2: benchmarks and comparison with the NMSSM, J. High Energy Phys. 06 (2016) 034, https://doi.org/10.1007/JHEP06(2016)034, arXiv:1512.05355 [hep-ph].
[23] Margarete Muhlleitner, et al., The N2HDM under theoretical and experimental scrutiny, J. High Energy Phys. 03 (2017) 094, https://doi.org/10.1007/JHEP03(2017)094, arXiv:1612.01309 [hep-ph].
[24] Margarete Mühlleitner, et al., ScannerS: parameter scans in extended scalar sectors, Eur. Phys. J. C 82 (3) (2022) 198, https://doi.org/10.1140/epjc/s10052-022-10139-w, arXiv:2007.02985 [hep-ph].
[25] Binetruy Pierre, et al., Cosmological backgrounds of gravitational waves and eLISA/NGO: phase transitions, cosmic strings and other sources, J. Cosmol. Astropart. Phys. 06 (2012) 027, https://doi.org/10.1088/1475-7516/2012/06/027, arXiv:1201.0983 [gr-qc].
[26] Chiara Caprini, et al., Science with the space-based interferometer eLISA. II: gravitational waves from cosmological phase transitions, J. Cosmol. Astropart. Phys. 1604 (04) (2016) 001, https://doi.org/10.1088/1475-7516/2016/04/001, arXiv:1512.06239 [astro-ph.CO].
[27] David J. Weir, Gravitational waves from a first order electroweak phase transition: a brief review, Philos. Trans. R. Soc. Lond. A 376 (2114) (2018) 20170126, https://doi.org/10.1098/rsta.2017.0126, Erratum: Philos. Trans. R. Soc. Lond. A 381 (2023) 20230212, arXiv:1705.01783 [hep-ph].
[28] Chiara Caprini, et al., Detecting gravitational waves from cosmological phase transitions with LISA: an update, J. Cosmol. Astropart. Phys. 2003 (03) (2020) 024, https://doi.org/10.1088/1475-7516/2020/03/024, arXiv:1910.13125 [astro-ph.CO].
[29] Mark B. Hindmarsh, et al., Phase transitions in the early universe, SciPost Phys. Lect. Notes 24 (2021) 1, https://doi.org/10.21468/SciPostPhysLectNotes.24, arXiv:2008.09136 [astro-ph.CO].
[30] J.E. Camargo-Molina, et al., **Vevacious**: a tool for finding the global minima of one-loop effective potentials with many scalars, Eur. Phys. J. C 73 (10) (2013) 2588, https://doi.org/10.1140/epjc/s10052-013-2588-2, arXiv:1307.1477 [hep-ph].
[31] J.E. Camargo-Molina, et al., Constraining the natural MSSM through tunneling to color-breaking vacua at zero and non-zero temperature, Phys. Lett. B 737 (2014) 156–161, https://doi.org/10.1016/j.physletb.2014.08.036, arXiv:1405.7376 [hep-ph].
[32] Florian Staub, From superpotential to model files for FeynArts and CalcHep/CompHep, Comput. Phys. Commun. 181 (2010) 1077–1086, https://doi.org/10.1016/j.cpc.2010.01.011, arXiv:0909.2863 [hep-ph].
[33] Florian Staub, Automatic calculation of supersymmetric renormalization group equations and self energies, Comput. Phys. Commun. 182 (2011) 808–833, https://doi.org/10.1016/j.cpc.2010.11.030, arXiv:1002.0840 [hep-ph].
[34] Florian Staub, SARAH 3.2: Dirac gauginos, UFO output, and more, Comput. Phys. Commun. 184 (2013) 1792–1809, https://doi.org/10.1016/j.cpc.2013.02.019, arXiv:1207.0906 [hep-ph].
[35] Florian Staub, SARAH 4: a tool for (not only SUSY) model builders, Comput. Phys. Commun. 185 (2014) 1773–1790, https://doi.org/10.1016/j.cpc.2014.02.018, arXiv:1309.7223 [hep-ph].
[36] Ali Masoumi, Ken D. Olum, Jeremy M. Wachter, Approximating tunneling rates in multi-dimensional field spaces, J. Cosmol. Astropart. Phys. 10 (2017) 022, https://doi.org/10.1088/1475-7516/2017/10/022, Erratum: J. Cosmol. Astropart. Phys. 05 (2023) E01, arXiv:1702.00356 [gr-qc].
[37] Wolfgang G. Hollik, Georg Weiglein, Jonas Wittbrodt, Impact of vacuum stability constraints on the phenomenology of supersymmetric models, J. High Energy Phys. 03 (2019) 109, https://doi.org/10.1007/JHEP03(2019)109, arXiv:1812.04644 [hep-ph].
[38] P.M. Ferreira, et al., Vacuum instabilities in the N2HDM, J. High Energy Phys. 09 (2019) 006, https://doi.org/10.1007/JHEP09(2019)006, arXiv:1905.10234 [hep-ph].
[39] EVADE, https://gitlab.com/jonaswittbrodt/EVADE.
[40] Peter Athron, et al., BubbleProfiler: finding the field profile and action for cosmological phase transitions, Comput. Phys. Commun. 244 (2019) 448–468, https://doi.org/10.1016/j.cpc.2019.05.017, arXiv:1901.03714 [hep-ph].
[41] Sujeet Akula, Csaba Balázs, Graham A. White, Semi-analytic techniques for calculating bubble wall profiles, Eur. Phys. J. C 76 (12) (2016) 681, https://doi.org/10.1140/epjc/s10052-016-4519-5, arXiv:1608.00008 [hep-ph].
[42] Peter Athron, et al., PhaseTracer: tracing cosmological phases and calculating transition properties, Eur. Phys. J. C 80 (6) (2020) 567, https://doi.org/10.1140/epjc/s10052-020-8035-2, arXiv:2003.02859 [hep-ph].
[43] Peter Athron, et al., FlexibleSUSY—a spectrum generator generator for supersymmetric models, Comput. Phys. Commun. 190 (2015) 139–172, https://doi.org/10.1016/j.cpc.2014.12.020, arXiv:1406.2319 [hep-ph].
[44] Peter Athron, et al., FlexibleSUSY 2.0: extensions to investigate the phenomenology of SUSY and non-SUSY models, Comput. Phys. Commun. 230 (2018) 145–217, https://doi.org/10.1016/j.cpc.2018.04.016, arXiv:1710.03760 [hep-ph].
[45] Ryosuke Sato, SimpleBounce: a simple package for the false vacuum decay, Comput. Phys. Commun. 258 (2021) 107566, https://doi.org/10.1016/j.cpc.2020.107566, arXiv:1908.10868 [hep-ph].
[46] Ryosuke Sato, Simple gradient flow equation for the bounce solution, Phys. Rev. D 101 (1) (2020) 016012, https://doi.org/10.1103/PhysRevD.101.016012, arXiv:1907.02417 [hep-ph].
[47] Victor Guada, Miha Nemevšek, Matevž Pintar, FindBounce: package for multi-field bounce actions, Comput. Phys. Commun. 256 (2020) 107480, https://doi.org/10.1016/j.cpc.2020.107480, arXiv:2002.00881 [hep-ph].
[48] Victor Guada, Alessio Maiezza, Miha Nemevšek, Multifield polygonal bounces, Phys. Rev. D 99 (5) (2019) 056020, https://doi.org/10.1103/PhysRevD.99.056020, arXiv:1803.02227 [hep-th].
[49] Michael Bardsley, An optimisation based algorithm for finding the nucleation temperature of cosmological phase transitions, Comput. Phys. Commun. 273 (2022) 108252, https://doi.org/10.1016/j.cpc.2021.108252, arXiv:2103.01985 [astro-ph.CO].
[50] Sidney R. Coleman, V. Glaser, Andre Martin, Action minima among solutions to a class of Euclidean scalar field equations, Commun. Math. Phys. 58 (1978) 211–221, https://doi.org/10.1007/BF01609421.
[51] Fatih Ertas, Felix Kahlhoefer, Carlo Tasillo, Turn up the volume: listening to phase transitions in hot dark sectors, J. Cosmol. Astropart. Phys. 02 (02) (2022) 014, https://doi.org/10.1088/1475-7516/2022/02/014, arXiv:2109.06208 [astro-ph.CO].
[52] Torsten Bringmann, et al., Hunting WIMPs with LISA: correlating dark matter and gravitational wave signals, J. Cosmol. Astropart. Phys. 05 (2024) 065, https://doi.org/10.1088/1475-7516/2024/05/065, arXiv:2311.06346 [astro-ph.CO].
[53] Giuseppe Degrassi, et al., Higgs mass and vacuum stability in the standard model at NNLO, J. High Energy Phys. 08 (2012) 098, https://doi.org/10.1007/JHEP08(2012)098, arXiv:1205.6497 [hep-ph].
[54] A.V. Bednyakov, et al., Stability of the electroweak vacuum: gauge independence and advanced precision, Phys. Rev. Lett. 115 (20) (2015) 201802, https://doi.org/10.1103/PhysRevLett.115.201802, arXiv:1507.08833 [hep-ph].
[55] P. Basler, et al., Strong first order electroweak phase transition in the CP-conserving 2HDM revisited, J. High Energy Phys. 02 (2017) 121, https://doi.org/10.1007/JHEP02(2017)121, arXiv:1612.04086 [hep-ph].
[56] Philipp Basler, Margarete Mühlleitner, Jonas Wittbrodt, The CP-violating 2HDM in light of a strong first order electroweak phase transition and implications for Higgs pair production, J. High Energy Phys. 03 (2018) 061, https://doi.org/10.1007/JHEP03(2018)061, arXiv:1711.04097 [hep-ph].
[57] Philipp Basler, et al., Showcasing HH production: benchmarks for the LHC and HL-LHC, Phys. Rev. D 99 (5) (2019) 055048, https://doi.org/10.1103/PhysRevD.99.055048, arXiv:1812.03542 [hep-ph].
[58] Lei Wang, et al., Revisiting lepton-specific 2HDM in light of muon g-2 anomaly, Phys. Lett. B 788 (2019) 519–529, https://doi.org/10.1016/j.physletb.2018.11.045, arXiv:1809.05857 [hep-ph].
[59] Xiao Wang, Fa Peng Huang, Xinmin Zhang, Gravitational wave and collider signals in complex two-Higgs doublet model with dynamical CP-violation at finite temperature, Phys. Rev. D 101 (1) (2020) 015015, https://doi.org/10.1103/PhysRevD.101.015015, arXiv:1909.02978 [hep-ph].

[60] Philipp Basler, et al., Di-Higgs boson peaks and top valleys: interference effects in Higgs sector extensions, Phys. Rev. D 101 (1) (2020) 015019, https://doi.org/10.1103/PhysRevD.101.015019, arXiv:1909.09987 [hep-ph].
[61] Philipp Basler, Margarete Mühlleitner, Jonas Müller, Electroweak phase transition in non-minimal Higgs sectors, J. High Energy Phys. 05 (2020) 016, https://doi.org/10.1007/JHEP05(2020)016, arXiv:1912.10477 [hep-ph].
[62] Philipp Basler, Vacuum Structure of Models beyond the Standard Model, PhD thesis, KIT, Karlsruhe, 2019.
[63] Seraina Glaus, et al., Electroweak corrections in a pseudo-Nambu Goldstone dark matter model revisited, J. High Energy Phys. 12 (2020) 034, https://doi.org/10.1007/JHEP12(2020)034, arXiv:2008.12985 [hep-ph].
[64] Shehu Abdussalam, Mohammad Javad Kazemi, Layla Kalhor, Upper limit on first-order electroweak phase transition strength, Int. J. Mod. Phys. A 36 (05) (2021) 2150024, https://doi.org/10.1142/S0217751X21920032, arXiv:2001.05973 [hep-ph].
[65] Wei Su, Anthony G. Williams, Mengchao Zhang, Strong first order electroweak phase transition in 2HDM confronting future Z & Higgs factories, J. High Energy Phys. 04 (2021) 219, https://doi.org/10.1007/JHEP04(2021)219, arXiv:2011.04540 [hep-ph].
[66] Martin Gabelmann, M. Margarete Mühlleitner, Jonas Müller, Electroweak phase transitions with BSM fermions, J. High Energy Phys. 01 (2022) 012, https://doi.org/10.1007/JHEP01(2022)012, arXiv:2107.09617 [hep-ph].
[67] Philipp Basler, et al., Electroweak baryogenesis in the CP-violating two-Higgs doublet model, Eur. Phys. J. C 83 (1) (2023) 57, https://doi.org/10.1140/epjc/s10052-023-11192-9, arXiv:2108.03580 [hep-ph].
[68] Arnab Chaudhuri, Maxim Yu. Khlopov, Entropy production due to electroweak phase transition in the framework of two Higgs doublet model, MDPI Physics 3 (2) (2021) 275–289, https://doi.org/10.3390/physics3020020, arXiv:2103.03477 [hep-ph].
[69] Thomas Biekötter, et al., Fate of electroweak symmetry in the early universe: non-restoration and trapped vacua in the N2HDM, J. Cosmol. Astropart. Phys. 06 (2021) 018, https://doi.org/10.1088/1475-7516/2021/06/018, arXiv:2103.12707 [hep-ph].
[70] Arnab Chaudhuri, Maxim Yu. Khlopov, Shiladitya Porey, Effects of 2HDM in electroweak phase transition, Galaxies 9 (2) (2021) 45, https://doi.org/10.3390/galaxies9020045, arXiv:2105.10728 [hep-ph].
[71] Oliver Atkinson, et al., Cornering the two Higgs doublet model type II, J. High Energy Phys. 04 (2022) 172, https://doi.org/10.1007/JHEP04(2022)172, arXiv:2107.05650 [hep-ph].
[72] Arnab Chaudhuri, Maxim Yu. Khlopov, Shiladitya Porey, Particle dark matter density and entropy production in the early universe, Symmetry 14 (2) (2022) 271, https://doi.org/10.3390/sym14020271, arXiv:2110.14161 [hep-ph].
[73] Arnab Chaudhuri, Maxim Yu. Khlopov, Shiladitya Porey, Entopy release in electroweak phase transition in 2HDM, in: 24th Workshop on What Comes Beyond the Standard Models?, Oct. 2021, arXiv:2111.00139 [hep-ph].
[74] Jonas Müller, Linking Cosmology with Collider Phenomenology, PhD thesis, KIT, Karlsruhe, 2021.
[75] Felix Egle, et al., One-loop corrections to the Higgs boson invisible decay in a complex singlet extension of the SM, Phys. Rev. D 106 (9) (2022) 095030, https://doi.org/10.1103/PhysRevD.106.095030, arXiv:2202.04035 [hep-ph].
[76] Anisha, et al., Two Higgs doublets, effective interactions and a strong first-order electroweak phase transition, J. High Energy Phys. 08 (2022) 091, https://doi.org/10.1007/JHEP08(2022)091, arXiv:2204.06966 [hep-ph].
[77] Lisa Biermann, Margarete Mühlleitner, Jonas Müller, Electroweak phase transition in a dark sector with CP violation, Eur. Phys. J. C 83 (5) (2023) 439, https://doi.org/10.1140/epjc/s10052-023-11612-w, arXiv:2204.13425 [hep-ph].
[78] Oliver Atkinson, et al., The flavourful present and future of 2HDMs at the collider energy frontier, J. High Energy Phys. 11 (2022) 139, https://doi.org/10.1007/JHEP11(2022)139, arXiv:2202.08807 [hep-ph].
[79] Huayang Song, Wei Su, Mengchao Zhang, Electroweak phase transition in 2HDM under Higgs, Z-pole, and W precision measurements, J. High Energy Phys. 10 (2022) 048, https://doi.org/10.1007/JHEP10(2022)048, arXiv:2204.05085 [hep-ph].
[80] Shehu AbdusSalam, Leila Kalhor, Mohammad Mohammadidoust, Light dark matter around 100 GeV from the inert doublet model, Eur. Phys. J. C 82 (10) (2022) 892, https://doi.org/10.1140/epjc/s10052-022-10862-4, arXiv:2208.13705 [hep-ph].
[81] Thomas Biekötter, et al., The trap in the early Universe: impact on the interplay between gravitational waves and LHC physics in the 2HDM, J. Cosmol. Astropart. Phys. 03 (2023) 031, https://doi.org/10.1088/1475-7516/2023/03/031, arXiv:2208.14466 [hep-ph].
[82] María Olalla Olea Romacho, Higgs physics as a window to the electroweak epoch, PhD thesis, U. Hamburg (Main), Hamburg U., 2022.
[83] Jae Hyeok Chang, María Olalla Olea-Romacho, Erwin H. Tanin, Electroweak asymmetric early Universe via a scalar condensate, Phys. Rev. D 106 (11) (2022) 113003, https://doi.org/10.1103/PhysRevD.106.113003, arXiv:2210.05680 [hep-ph].
[84] Wei Su, Anthony G. Williams, Mengchao Zhang, Probing EWPT in 2HDM with future lepton colliders, Int. J. Mod. Phys. A 37 (30) (2022) 2246008, https://doi.org/10.1142/S0217751X22460083.
[85] Lisa Biermann, Margarete Mühlleitner, Jonas Müller, 'CP in the dark' and a strong first-order electroweak phase transition, PoS DISCRETE2022 (2024) 024, https://doi.org/10.22323/1.431.0024, arXiv:2301.09004 [hep-ph].
[86] Felix Egle, et al., Electroweak corrections to Higgs boson decays in a complex singlet extension of the SM and their phenomenological impact, J. High Energy Phys. 11 (2023) 116, https://doi.org/10.1007/JHEP11(2023)116, arXiv:2306.04127 [hep-ph].
[87] Mayumi Aoki, et al., Intermediate charge-breaking phases and symmetry non-restoration in the 2-Higgs-doublet model, J. High Energy Phys. 02 (2024) 232, https://doi.org/10.1007/JHEP02(2024)232, arXiv:2308.04141 [hep-ph].
[88] Dorival Gonçalves, Ajay Kaladharan, Yongcheng Wu, Gravitational waves, bubble profile, and baryon asymmetry in the complex 2HDM, Phys. Rev. D 108 (7) (2023) 075010, https://doi.org/10.1103/PhysRevD.108.075010, arXiv:2307.03224 [hep-ph].
[89] Sven Heinemeyer, et al., Higgs pair production and triple Higgs couplings at the LHC in the 2HDM framework, PoS EPS-HEP2023 (2024) 411, https://doi.org/10.22323/1.449.0411.
[90] S. Heinemeyer, et al., Higgs pair production in the 2HDM: impact of loop corrections to the trilinear Higgs couplings and interference effects on experimental limits, arXiv:2403.14776 [hep-ph], Mar. 2024.
[91] Anisha, et al., Effective 2HDM Yukawa interactions and a strong first-order electroweak phase transition, J. High Energy Phys. 02 (2024) 045, https://doi.org/10.1007/JHEP02(2024)045, arXiv:2311.06353 [hep-ph].
[92] Patrick Meade, Harikrishnan Ramani, Unrestored electroweak symmetry, Phys. Rev. Lett. 122 (4) (2019) 041802, https://doi.org/10.1103/PhysRevLett.122.041802, arXiv:1807.07578 [hep-ph].
[93] Iason Baldes, Géraldine Servant, High scale electroweak phase transition: baryogenesis & symmetry non-restoration, J. High Energy Phys. 10 (2018) 053, https://doi.org/10.1007/JHEP10(2018)053, arXiv:1807.08770 [hep-ph].
[94] Oleksii Matsedonskyi, Geraldine Servant, High-temperature electroweak symmetry non-restoration from new fermions and implications for baryogenesis, J. High Energy Phys. 09 (2020) 012, https://doi.org/10.1007/JHEP09(2020)012, arXiv:2002.05174 [hep-ph].
[95] Carena Marcela, et al., New approach to electroweak symmetry nonrestoration, Phys. Rev. D 104 (5) (2021) 055016, https://doi.org/10.1103/PhysRevD.104.055016, arXiv:2104.00638 [hep-ph].
[96] Sebastian Baum, et al., Nucleation is more than critical: a case study of the electroweak phase transition in the NMSSM, J. High Energy Phys. 03 (2021) 055, https://doi.org/10.1007/JHEP03(2021)055, arXiv:2009.10743 [hep-ph].
[97] Philip Bechtle, et al., HiggsBounds: confronting arbitrary Higgs sectors with exclusion bounds from LEP and the Tevatron, Comput. Phys. Commun. 181 (2010) 138–167, https://doi.org/10.1016/j.cpc.2009.09.003, arXiv:0811.4169 [hep-ph].
[98] Philip Bechtle, et al., HiggsBounds 2.0.0: confronting neutral and charged Higgs sector predictions with exclusion bounds from LEP and the Tevatron, Comput. Phys. Commun. 182 (2011) 2605–2631, https://doi.org/10.1016/j.cpc.2011.07.015, arXiv:1102.1898 [hep-ph].
[99] Philip Bechtle, et al., Recent developments in HiggsBounds and a preview of HiggsSignals, in: Enberg Rikard, Arnaud Ferrari (Eds.), PoS CHARGED2012, 2012, p. 024, arXiv:1301.2345 [hep-ph].
[100] Philip Bechtle, et al., HiggsBounds – 4: improved tests of extended Higgs sectors against exclusion bounds from LEP, the Tevatron and the LHC, Eur. Phys. J. C 74 (3) (2014) 2693, https://doi.org/10.1140/epjc/s10052-013-2693-2, arXiv:1311.0055 [hep-ph].
[101] Philip Bechtle, et al., Applying exclusion likelihoods from LHC searches to extended Higgs sectors, Eur. Phys. J. C 75 (9) (2015) 421, https://doi.org/10.1140/epjc/s10052-015-3650-z, arXiv:1507.06706 [hep-ph].

[102] Philip Bechtle, et al., HiggsBounds-5: testing Higgs sectors in the LHC 13 TeV era, Eur. Phys. J. C 80 (12) (2020) 1211, https://doi.org/10.1140/epjc/s10052-020-08557-9, arXiv:2006.06007 [hep-ph].
[103] Henning Bahl, et al., Testing exotic scalars with HiggsBounds, Eur. Phys. J. C 82 (7) (2022) 584, https://doi.org/10.1140/epjc/s10052-022-10446-2, arXiv:2109.10366 [hep-ph].
[104] Philip Bechtle, et al., *HiggsSignals*: confronting arbitrary Higgs sectors with measurements at the Tevatron and the LHC, Eur. Phys. J. C 74 (2) (2014) 2711, https://doi.org/10.1140/epjc/s10052-013-2711-4, arXiv:1305.1933 [hep-ph].
[105] Stål Oscar, Tim Stefaniak, Constraining extended Higgs sectors with HiggsSignals, PoS EPS-HEP2013 (2013) 314, https://doi.org/10.22323/1.180.0314, arXiv:1310.4039 [hep-ph].
[106] Philip Bechtle, et al., Probing the standard model with Higgs signal rates from the Tevatron, the LHC and a future ILC, J. High Energy Phys. 11 (2014) 039, https://doi.org/10.1007/JHEP11(2014)039, arXiv:1403.1582 [hep-ph].
[107] Philip Bechtle, et al., HiggsSignals-2: probing new physics with precision Higgs measurements in the LHC 13 TeV era, Eur. Phys. J. C 81 (2) (2021) 145, https://doi.org/10.1140/epjc/s10052-021-08942-y, arXiv:2012.09197 [hep-ph].
[108] Henning Bahl, et al., HiggsTools: BSM scalar phenomenology with new versions of HiggsBounds and HiggsSignals, Comput. Phys. Commun. 291 (2023) 108803, https://doi.org/10.1016/j.cpc.2023.108803, arXiv:2210.09332 [hep-ph].
[109] G. Belanger, et al., MicrOMEGAs: a program for calculating the relic density in the MSSM, Comput. Phys. Commun. 149 (2002) 103–120, https://doi.org/10.1016/S0010-4655(02)00596-9, arXiv:hep-ph/0112278.
[110] G. Belanger, et al., micrOMEGAs: version 1.3, Comput. Phys. Commun. 174 (2006) 577–604, https://doi.org/10.1016/j.cpc.2005.12.005, arXiv:hep-ph/0405253.
[111] G. Belanger, et al., MicrOMEGAs 2.0: a program to calculate the relic density of dark matter in a generic model, Comput. Phys. Commun. 176 (2007) 367–382, https://doi.org/10.1016/j.cpc.2006.11.008, arXiv:hep-ph/0607059.
[112] G. Belanger, et al., Dark matter direct detection rate in a generic model with micrOMEGAs 2.2, Comput. Phys. Commun. 180 (2009) 747–767, https://doi.org/10.1016/j.cpc.2008.11.019, arXiv:0803.2360 [hep-ph].
[113] G. Belanger, et al., Indirect search for dark matter with micrOMEGAs2.4, Comput. Phys. Commun. 182 (2011) 842–856, https://doi.org/10.1016/j.cpc.2010.11.033, arXiv:1004.1092 [hep-ph].
[114] G. Belanger, et al., micrOMEGAs_3: a program for calculating dark matter observables, Comput. Phys. Commun. 185 (2014) 960–985, https://doi.org/10.1016/j.cpc.2013.10.016, arXiv:1305.0237 [hep-ph].
[115] G. Bélanger, et al., micrOMEGAs4.1: two dark matter candidates, Comput. Phys. Commun. 192 (2015) 322–329, https://doi.org/10.1016/j.cpc.2015.03.003, arXiv:1407.6129 [hep-ph].
[116] D. Barducci, et al., Collider limits on new physics within micrOMEGAs_4.3, Comput. Phys. Commun. 222 (2018) 327–338, https://doi.org/10.1016/j.cpc.2017.08.028, arXiv:1606.03834 [hep-ph].
[117] Geneviève Bélanger, et al., micrOMEGAs5.0: freeze-in, Comput. Phys. Commun. 231 (2018) 173–186, https://doi.org/10.1016/j.cpc.2018.04.027, arXiv:1801.03509 [hep-ph].
[118] G. Alguero, et al., micrOMEGAs 6.0: N-component dark matter, Comput. Phys. Commun. 299 (2024) 109133, https://doi.org/10.1016/j.cpc.2024.109133, arXiv:2312.14894 [hep-ph].
[119] Aaron Meurer, et al., SymPy: symbolic computing in Python, PeerJ Comput. Sci. (ISSN 2376-5992) 3 (Jan. 2017) e103, https://doi.org/10.7717/peerj-cs.103.
[120] Maplesoft, a division of Waterloo Maple Inc., Maple, Version 2019, Waterloo, Ontario, https://hadoop.apache.org, 2019.
[121] Wolfram Research Inc., Mathematica, Champaign, IL, https://www.wolfram.com/mathematica, 2024.
[122] Peter Athron, et al., Cosmological phase transitions: from perturbative particle physics to gravitational waves, Prog. Part. Nucl. Phys. 135 (2024) 104094, https://doi.org/10.1016/j.ppnp.2023.104094, arXiv:2305.02357 [hep-ph].
[123] Kimmo Kainulainen, et al., On the validity of perturbative studies of the electroweak phase transition in the two Higgs doublet model, J. High Energy Phys. 06 (2019) 075, https://doi.org/10.1007/JHEP06(2019)075, arXiv:1904.01329 [hep-ph].
[124] Lauri Niemi, et al., Thermodynamics of a two-step electroweak phase transition, Phys. Rev. Lett. 126 (17) (2021) 171802, https://doi.org/10.1103/PhysRevLett.126.171802, arXiv:2005.11332 [hep-ph].
[125] Oliver Gould, Real scalar phase transitions: a nonperturbative analysis, J. High Energy Phys. 04 (2021) 057, https://doi.org/10.1007/JHEP04(2021)057, arXiv:2101.05528 [hep-ph].
[126] Oliver Gould, Sinan Güyer, Kari Rummukainen, First-order electroweak phase transitions: a nonperturbative update, Phys. Rev. D 106 (11) (2022) 114507, https://doi.org/10.1103/PhysRevD.106.114507, arXiv:2205.07238 [hep-lat].
[127] Mark Hindmarsh, et al., Numerical simulations of acoustically generated gravitational waves at a first order phase transition, Phys. Rev. D 92 (12) (2015) 123009, https://doi.org/10.1103/PhysRevD.92.123009, arXiv:1504.03291 [astro-ph.CO].
[128] Andreas Ekstedt, Philipp Schicho, Tuomas V.I. Tenkanen, DRalgo: a package for effective field theory approach for thermal phase transitions, Comput. Phys. Commun. 288 (2023) 108725, https://doi.org/10.1016/j.cpc.2023.108725, arXiv:2205.08815 [hep-ph].
[129] Andrei D. Linde, Infrared problem in thermodynamics of the Yang-Mills gas, Phys. Lett. B 96 (1980) 289–292, https://doi.org/10.1016/0370-2693(80)90769-8.
[130] Eric Braaten, Solution to the perturbative infrared catastrophe of hot gauge theories, Phys. Rev. Lett. 74 (1995) 2164–2167, https://doi.org/10.1103/PhysRevLett.74.2164, arXiv:hep-ph/9409434.
[131] Peter Brockway Arnold, Olivier Espinosa, The effective potential and first order phase transitions: beyond leading-order, Phys. Rev. D 47 (1993) 3546, https://doi.org/10.1103/PhysRevD.47.3546, Erratum: Phys. Rev. D 50 (1994) 6662, arXiv:hep-ph/9212235.
[132] K. Farakos, et al., 3-D physics and the electroweak phase transition: perturbation theory, Nucl. Phys. B 425 (1994) 67–109, https://doi.org/10.1016/0550-3213(94)90173-2, arXiv:hep-ph/9404201.
[133] Djuna Croon, et al., Theoretical uncertainties for cosmological first-order phase transitions, J. High Energy Phys. 04 (2021) 055, https://doi.org/10.1007/JHEP04(2021)055, arXiv:2009.10080 [hep-ph].
[134] Oliver Gould, Tuomas V.I. Tenkanen, On the perturbative expansion at high temperature and implications for cosmological phase transitions, J. High Energy Phys. 06 (2021) 069, https://doi.org/10.1007/JHEP06(2021)069, arXiv:2104.04399 [hep-ph].
[135] R. Jackiw, Functional evaluation of the effective potential, Phys. Rev. D 9 (1974) 1686, https://doi.org/10.1103/PhysRevD.9.1686.
[136] Hiren H. Patel, Michael J. Ramsey-Musolf, Baryon washout, electroweak phase transition, and perturbation theory, J. High Energy Phys. 07 (2011) 029, https://doi.org/10.1007/JHEP07(2011)029, arXiv:1101.4665 [hep-ph].
[137] Joonas Hirvonen, et al., Computing the gauge-invariant bubble nucleation rate in finite temperature effective field theory, J. High Energy Phys. 07 (2022) 135, https://doi.org/10.1007/JHEP07(2022)135, arXiv:2112.08912 [hep-ph].
[138] Johan Löfgren, et al., Nucleation at finite temperature: a gauge-invariant perturbative framework, Phys. Rev. Lett. 130 (25) (2023) 251801, https://doi.org/10.1103/PhysRevLett.130.251801, arXiv:2112.05472 [hep-ph].
[139] Philipp Schicho, Tuomas V.I. Tenkanen, Graham White, Combining thermal resummation and gauge invariance for electroweak phase transition, J. High Energy Phys. 11 (2022) 047, https://doi.org/10.1007/JHEP11(2022)047, arXiv:2203.04284 [hep-ph].
[140] Peter Athron, et al., How arbitrary are perturbative calculations of the electroweak phase transition?, J. High Energy Phys. 01 (2023) 050, https://doi.org/10.1007/JHEP01(2023)050, arXiv:2208.01319 [hep-ph].
[141] Renhui Qin, Ligong Bian, First-order electroweak phase transition with gauge-invariant approach, arXiv:2408.09677 [hep-ph], Aug. 2024.
[142] James M. Cline, Michael Joyce, Kimmo Kainulainen, Supersymmetric electroweak baryogenesis in the WKB approximation, Phys. Lett. B 417 (1998) 79–86, https://doi.org/10.1016/S0370-2693(97)01361-0, Erratum: Phys. Lett. B 448 (1999) 321, arXiv:hep-ph/9708393.
[143] Kimmo Kainulainen, et al., First principle derivation of semiclassical force for electroweak baryogenesis, J. High Energy Phys. 06 (2001) 031, https://doi.org/10.1088/1126-6708/2001/06/031, arXiv:hep-ph/0105295.
[144] Lars Fromme, Stephan J. Huber, Top transport in electroweak baryogenesis, J. High Energy Phys. 03 (2007) 049, https://doi.org/10.1088/1126-6708/2007/03/049, arXiv:hep-ph/0604159.
[145] Lars Fromme, Stephan J. Huber, Michael Seniuch, Baryogenesis in the two-Higgs doublet model, J. High Energy Phys. 11 (2006) 038, https://doi.org/10.1088/1126-6708/2006/11/038, arXiv:hep-ph/0605242.
[146] Antonio Riotto, Towards a nonequilibrium quantum field theory approach to electroweak baryogenesis, Phys. Rev. D 53 (1996) 5834–5841, https://doi.org/10.1103/PhysRevD.53.5834, arXiv:hep-ph/9510271.

[147] A. Riotto, Supersymmetric electroweak baryogenesis, nonequilibrium field theory and quantum Boltzmann equations, Nucl. Phys. B 518 (1998) 339–360, https://doi.org/10.1016/S0550-3213(98)00159-X, arXiv:hep-ph/9712221.
[148] Christopher Lee, Vincenzo Cirigliano, Michael J. Ramsey-Musolf, Resonant relaxation in electroweak baryogenesis, Phys. Rev. D 71 (2005) 075010, https://doi.org/10.1103/PhysRevD.71.075010, arXiv:hep-ph/0412354.
[149] Daniel J.H. Chung, et al., Supergauge interactions and electroweak baryogenesis, J. High Energy Phys. 12 (2009) 067, https://doi.org/10.1088/1126-6708/2009/12/067, arXiv:0908.2187 [hep-ph].
[150] Marieke Postma, Jorinde van de Vis, Graham White, Resummation and cancellation of the VIA source in electroweak baryogenesis, J. High Energy Phys. 12 (2022) 121, https://doi.org/10.1007/JHEP12(2022)121, arXiv:2206.01120 [hep-ph].
[151] The Python package installer, https://github.com/pypa/pip.
[152] M. Galassi, et al., GNU scientific library reference manual, https://www.gnu.org/software/gsl/, 2018.
[153] Niels Lohmann, JSON for modern C++, https://github.com/nlohmann/json.
[154] Martin Hořeňovský, et al., Catch2, https://github.com/catchorg/Catch2.
[155] Google, Benchmark, https://github.com/google/benchmark.
[156] Emmanuel Benazera, Nikolaus Hansen, et al., libcmaes, https://github.com/CMA-ES/libcmaes.
[157] Steven G. Johnson, The NLopt nonlinear-optimization package, https://github.com/stevengj/nlopt.
[158] J.M. Gablonsky, C.T. Kelley, A locally-biased form of the DIRECT algorithm, J. Glob. Optim. 21 (2001) 27–37, https://doi.org/10.1023/a:1017930332101.
[159] Rajesh R. Parwani, Resummation in a hot scalar field theory, Phys. Rev. D 45 (1992) 4695, https://doi.org/10.1103/PhysRevD.45.4695, Erratum: Phys. Rev. D 48 (1993) 5965, arXiv:hep-ph/9204216.
[160] J.A. Nelder, R. Mead, A simplex method for function minimization, Comput. J. 7 (1965) 308–313, https://doi.org/10.1093/comjnl/7.4.308.
[161] V. Branchina, F. Contino, P.M. Ferreira, Electroweak vacuum lifetime in two Higgs doublet models, J. High Energy Phys. (ISSN 1029-8479) 2018 (11) (Nov. 2018), https://doi.org/10.1007/jhep11(2018)107.
[162] Ya.B. Zeldovich, I.Yu. Kobzarev, L.B. Okun, Cosmological consequences of the spontaneous breakdown of discrete symmetry, Zh. Eksp. Teor. Fiz. 67 (1974) 3–11.
[163] T.W.B. Kibble, Topology of cosmic domains and strings, J. Phys. A 9 (1976) 1387–1398, https://doi.org/10.1088/0305-4470/9/8/029.
[164] W.H. Zurek, Cosmological experiments in superfluid helium?, Nature 317 (1985) 505–508, https://doi.org/10.1038/317505a0.
[165] Sebastian E. Larsson, Subir Sarkar, Peter L. White, Evading the cosmological domain wall problem, Phys. Rev. D 55 (1997) 5129–5135, https://doi.org/10.1103/PhysRevD.55.5129, arXiv:hep-ph/9608319.
[166] William H. Press, Barbara S. Ryden, David N. Spergel, Dynamical evolution of domain walls in an expanding universe, Astrophys. J. 347 (1989) 590–604, https://doi.org/10.1086/168151.
[167] A. Lazanu, C.J.A.P. Martins, E.P.S. Shellard, Contribution of domain wall networks to the CMB power spectrum, Phys. Lett. B 747 (2015) 426–432, https://doi.org/10.1016/j.physletb.2015.06.034, arXiv:1505.03673 [astro-ph.CO].
[168] Richard A. Battye, Gary D. Brawn, Apostolos Pilaftsis, Vacuum topology of the two Higgs doublet model, J. High Energy Phys. 08 (2011) 020, https://doi.org/10.1007/JHEP08(2011)020, arXiv:1106.3482 [hep-ph].
[169] Richard A. Battye, Apostolos Pilaftsis, Dominic G. Viatic, Simulations of domain walls in two Higgs doublet models, J. High Energy Phys. 01 (2021) 105, https://doi.org/10.1007/JHEP01(2021)105, arXiv:2006.13273 [hep-ph].
[170] Kai Hong Law, Apostolos Pilaftsis, Charged and CP-violating kink solutions in the two-Higgs-doublet model, Phys. Rev. D 105 (5) (2022) 056007, https://doi.org/10.1103/PhysRevD.105.056007, arXiv:2110.12550 [hep-ph].
[171] Mohamed Younes Sassi, Gudrid Moortgat-Pick, Domain walls in the two-Higgs-doublet model and their charge and CP-violating interactions with standard model fermions, arXiv:2309.12398 [hep-ph], Sept. 2023.
[172] Yucheng Yang, Igor P. Ivanov, Charge-breaking domain walls separating neutral vacua in multi-Higgs models, arXiv:2401.03264 [hep-ph], Jan. 2024.
[173] Takashi Hiramatsu, Masahiro Kawasaki, Ken'ichi Saikawa, Gravitational waves from collapsing domain walls, J. Cosmol. Astropart. Phys. 05 (2010) 032, https://doi.org/10.1088/1475-7516/2010/05/032, arXiv:1002.1555 [astro-ph.CO].
[174] Sidney Coleman, Fate of the false vacuum: semiclassical theory, Phys. Rev. D 15 (May 1977) 2929–2936, https://doi.org/10.1103/PhysRevD.15.2929, https://link.aps.org/doi/10.1103/PhysRevD.15.2929.
[175] Thomas Banks, Carl M. Bender, Tai Tsun Wu, Coupled anharmonic oscillators. I. Equal-mass case, Phys. Rev. D 8 (10) (Nov. 1973) 3346–3366, https://doi.org/10.1103/physrevd.8.3346.
[176] A.D. Linde, Fate of the false vacuum at finite temperature: theory and applications, Phys. Lett. B (ISSN 0370-2693) 100 (1) (1981) 37–40, https://doi.org/10.1016/0370-2693(81)90281-1, https://www.sciencedirect.com/science/article/pii/0370269381902811.
[177] Curtis G. Callan, Sidney Coleman, Fate of the false vacuum. II. First quantum corrections, Phys. Rev. D 16 (Sept. 1977) 1762–1768, https://doi.org/10.1103/PhysRevD.16.1762, https://link.aps.org/doi/10.1103/PhysRevD.16.1762.
[178] G.H. Derrick, Comments on nonlinear wave equations as models for elementary particles, J. Math. Phys. 5 (1964) 1252–1254, https://doi.org/10.1063/1.1704233.
[179] James M. Cline, Guy D. Moore, Géraldine Servant, Was the electroweak phase transition preceded by a color-broken phase?, Phys. Rev. D 60 (Oct. 1999) 105035, https://doi.org/10.1103/PhysRevD.60.105035, https://link.aps.org/doi/10.1103/PhysRevD.60.105035.
[180] Viatcheslav Mukhanov, Alexander Sorin, On the existence of the Coleman instantons, J. Cosmol. Astropart. Phys. 10 (2021) 066, https://doi.org/10.1088/1475-7516/2021/10/066, arXiv:2104.12661 [hep-th].
[181] J.R. Espinosa, Tunneling without bounce, Phys. Rev. D 100 (10) (2019) 105002, https://doi.org/10.1103/PhysRevD.100.105002, arXiv:1908.01730 [hep-th].
[182] Viatcheslav F. Mukhanov, Eliezer Rabinovici, Alexander S. Sorin, Quantum fluctuations and new instantons I: linear unbounded potential, Fortschr. Phys. 69 (2) (2021) 2000100, https://doi.org/10.1002/prop.202000100, arXiv:2009.12445 [hep-th].
[183] Viatcheslav Mukhanov, Eliezer Rabinovici, Alexander Sorin, Quantum fluctuations and new instantons II: quartic unbounded potential, Fortschr. Phys. 69 (2) (2021) 2000101, https://doi.org/10.1002/prop.202000101, arXiv:2009.12444 [hep-th].
[184] J.R. Espinosa, J. Huertas, Pseudo-bounces vs. new instantons, J. Cosmol. Astropart. Phys. 12 (12) (2021) 029, https://doi.org/10.1088/1475-7516/2021/12/029, arXiv:2106.04541 [hep-th].
[185] Chris Lorenz, Robert Ziff, Precise determination of the critical percolation threshold for the three-dimensional "Swiss cheese" model using a growth algorithm, J. Chem. Phys. 114 (Feb. 2001), https://doi.org/10.1063/1.1338506.
[186] Jianjun Lin, Huisu Chen, Continuum percolation of porous media via random packing of overlapping cube-like particles, Theor. Appl. Mech. Lett. (ISSN 2095-0349) 8 (5) (2018) 299–303, https://doi.org/10.1016/j.taml.2018.05.007, https://www.sciencedirect.com/science/article/pii/S209503491830196X.
[187] Mingqi Li, Huisu Chen, Jianjun Lin, Numerical study for the percolation threshold and transport properties of porous composites comprising non-centrosymmetrical superovoidal pores, Comput. Methods Appl. Mech. Eng. (ISSN 0045-7825) 361 (2020) 112815, https://doi.org/10.1016/j.cma.2019.112815, https://www.sciencedirect.com/science/article/pii/S0045782519307078.
[188] Pau Amaro-Seoane, et al., Laser interferometer space antenna, arXiv:1702.00786 [astro-ph.IM], 2017.
[189] Pierre Auclair, et al., Cosmology with the laser interferometer space antenna, Living Rev. Relativ. 26 (1) (2023) 5, https://doi.org/10.1007/s41114-023-00045-2, arXiv:2204.05434 [astro-ph.CO].
[190] Rong-Gen Cai, Misao Sasaki, Shao-Jiang Wang, The gravitational waves from the first-order phase transition with a dimension-six operator, J. Cosmol. Astropart. Phys. 08 (2017) 004, https://doi.org/10.1088/1475-7516/2017/08/004, arXiv:1707.03001 [astro-ph.CO].
[191] Mark Hindmarsh, et al., Shape of the acoustic gravitational wave power spectrum from a first order phase transition, Phys. Rev. D 96 (10) (2017) 103520, https://doi.org/10.1103/PhysRevD.96.103520, Erratum: Phys. Rev. D 101 (2020) 089902, arXiv:1704.05871 [astro-ph.CO].
[192] John Ellis, Marek Lewicki, José Miguel No, On the maximal strength of a first-order electroweak phase transition and its gravitational wave signal, J. Cosmol. Astropart. Phys. 04 (2019) 003, https://doi.org/10.1088/1475-7516/2019/04/003, arXiv:1809.08242 [hep-ph].
[193] Felix Giese, Thomas Konstandin, Jorinde van de Vis, Model-independent energy budget of cosmological first-order phase transitions—a sound argument to go beyond the bag model, J. Cosmol. Astropart. Phys. 07 (07) (2020) 057, https://doi.org/10.1088/1475-7516/2020/07/057, arXiv:2004.06995 [astro-ph.CO].
[194] Guy D. Moore, Measuring the broken phase sphaleron rate nonperturbatively, Phys. Rev. D 59 (1999) 014503, https://doi.org/10.1103/PhysRevD.59.014503, arXiv:hep-ph/9805264.

[195] Maciej Kierkla, Alexandros Karam, Bogumila Swiezewska, Conformal model for gravitational waves and dark matter: a status update, J. High Energy Phys. 03 (2023) 007, https://doi.org/10.1007/JHEP03(2023)007, arXiv:2210.07075 [astro-ph.CO].
[196] John Ellis, et al., The scalar singlet extension of the standard model: gravitational waves versus baryogenesis, J. High Energy Phys. 01 (2023) 093, https://doi.org/10.1007/JHEP01(2023)093, arXiv:2210.16305 [hep-ph].
[197] João Gonçalves, et al., Gravitational waves from supercooled phase transitions in conformal Majoron models of neutrino mass, arXiv:2412.02645 [hep-ph], Dec. 2024.
[198] John T. Giblin, Eric Thrane, The detectability of cosmological gravitational-wave backgrounds: a rule of thumb, https://api.semanticscholar.org/CorpusID:118954150, 2014.
[199] Thomas Konstandin, Geraldine Servant, Cosmological consequences of nearly conformal dynamics at the TeV scale, J. Cosmol. Astropart. Phys. 12 (2011) 009, https://doi.org/10.1088/1475-7516/2011/12/009, arXiv:1104.4791 [hep-ph].
[200] Chiara Caprini, Ruth Durrer, Gravitational waves from stochastic relativistic sources: primordial turbulence and magnetic fields, Phys. Rev. D 74 (2006) 063521, https://doi.org/10.1103/PhysRevD.74.063521, arXiv:astro-ph/0603476.
[201] Wen-Yuan Ai, Benoit Laurent, Jorinde van de Vis, Model-independent bubble wall velocities in local thermal equilibrium, J. Cosmol. Astropart. Phys. 07 (2023) 002, https://doi.org/10.1088/1475-7516/2023/07/002, arXiv:2303.10171 [astro-ph.CO].
[202] Marek Lewicki, Marco Merchand, Mateusz Zych, Electroweak bubble wall expansion: gravitational waves and baryogenesis in standard model-like thermal plasma, J. High Energy Phys. 2022 (Feb. 2022) 2, https://doi.org/10.1007/jhep02(2022)017.
[203] John Ellis, et al., The scalar singlet extension of the standard model: gravitational waves versus baryogenesis, J. High Energy Phys. 2023 (1) (Jan. 2023), https://doi.org/10.1007/jhep01(2023)093.
[204] Felix Giese, et al., Model-independent energy budget for LISA, J. Cosmol. Astropart. Phys. 01 (2021) 072, https://doi.org/10.1088/1475-7516/2021/01/072, arXiv:2010.09744 [astro-ph.CO].
[205] Andreas Ekstedt, et al., How fast does the WallGo? A package for computing wall velocities in first-order phase transitions, arXiv:2411.04970 [hep-ph], Nov. 2024.
[206] Christophe Grojean, Geraldine Servant, Gravitational waves from phase transitions at the electroweak scale and beyond, Phys. Rev. D 75 (2007) 043507, https://doi.org/10.1103/PhysRevD.75.043507, arXiv:hep-ph/0607107 [hep-ph].
[207] Leonardo Leitao, Ariel Megevand, Gravitational waves from a very strong electroweak phase transition, J. Cosmol. Astropart. Phys. 1605 (05) (2016) 037, https://doi.org/10.1088/1475-7516/2016/05/037, arXiv:1512.08962 [astro-ph.CO].
[208] Chiara Caprini, Ruth Durrer, Gravitational wave production: a strong constraint on primordial magnetic fields, Phys. Rev. D 65 (2001) 023517, https://doi.org/10.1103/PhysRevD.65.023517, arXiv:astro-ph/0106244.
[209] Daniel G. Figueroa, Mark Hindmarsh, Jon Urrestilla, Exact scale-invariant background of gravitational waves from cosmic defects, Phys. Rev. Lett. 110 (10) (2013) 101302, https://doi.org/10.1103/PhysRevLett.110.101302, arXiv:1212.5458 [astro-ph.CO].
[210] Mark Hindmarsh, Sound shell model for acoustic gravitational wave production at a first-order phase transition in the early Universe, Phys. Rev. Lett. 120 (7) (2018) 071301, https://doi.org/10.1103/PhysRevLett.120.071301, arXiv:1608.04735 [astro-ph.CO].
[211] N. Aghanim, et al., Planck 2018 results, Astron. Astrophys. 641 (Sept. 2020) A6, https://doi.org/10.1051/0004-6361/201833910.
[212] Chiara Caprini, et al., Gravitational waves from first-order phase transitions in LISA: reconstruction pipeline and physics interpretation, J. Cosmol. Astropart. Phys. 10 (2024) 020, https://doi.org/10.1088/1475-7516/2024/10/020, arXiv:2403.03723 [astro-ph.CO].
[213] Marek Lewicki, Ville Vaskonen, Gravitational waves from bubble collisions and fluid motion in strongly supercooled phase transitions, Eur. Phys. J. C 83 (2) (2023) 109, https://doi.org/10.1140/epjc/s10052-023-11241-3, arXiv:2208.11697 [astro-ph.CO].
[214] John Ellis, et al., Gravitational wave energy budget in strongly supercooled phase transitions, J. Cosmol. Astropart. Phys. 1906 (06) (2019) 024, https://doi.org/10.1088/1475-7516/2019/06/024, arXiv:1903.09642 [hep-ph].
[215] John Ellis, Marek Lewicki, Ville Vaskonen, Updated predictions for gravitational waves produced in a strongly supercooled phase transition, J. Cosmol. Astropart. Phys. 11 (2020) 020, https://doi.org/10.1088/1475-7516/2020/11/020, arXiv:2007.15586 [astro-ph.CO].
[216] Yann Gouttenoire, Ryusuke Jinno, Filippo Sala, Friction pressure on relativistic bubble walls, J. High Energy Phys. 05 (2022) 004, https://doi.org/10.1007/JHEP05(2022)004, arXiv:2112.07686 [hep-ph].
[217] Alan H. Guth, S.H.H. Tye, Phase transitions and magnetic monopole production in the very early universe, Phys. Rev. Lett. 44 (1980) 631, https://doi.org/10.1103/PhysRevLett.44.631, Erratum: Phys. Rev. Lett. 44 (1980) 963.
[218] Alan H. Guth, Erick J. Weinberg, Cosmological consequences of a first order phase transition in the SU(5) grand unified model, Phys. Rev. D 23 (1981) 876, https://doi.org/10.1103/PhysRevD.23.876.
[219] K. Enqvist, et al., Nucleation and bubble growth in a first order cosmological electroweak phase transition, Phys. Rev. D 45 (1992) 3415–3428, https://doi.org/10.1103/PhysRevD.45.3415.
[220] Michael S. Turner, Erick J. Weinberg, Lawrence M. Widrow, Bubble nucleation in first order inflation and other cosmological phase transitions, Phys. Rev. D 46 (1992) 2384–2403, https://doi.org/10.1103/PhysRevD.46.2384.
[221] Mårten Bertenstam, et al., Gravitational waves from color restoration in a leptoquark model of radiative neutrino masses, arXiv:2501.01286 [hep-ph], Jan. 2025.
[222] Dietrich Bodeker, Guy D. Moore, Can electroweak bubble walls run away?, J. Cosmol. Astropart. Phys. 05 (2009) 009, https://doi.org/10.1088/1475-7516/2009/05/009, arXiv:0903.4099 [hep-ph].
[223] Dietrich Bodeker, Guy D. Moore, Electroweak bubble wall speed limit, J. Cosmol. Astropart. Phys. 05 (2017) 025, https://doi.org/10.1088/1475-7516/2017/05/025, arXiv:1703.08215 [hep-ph].
[224] Stefan Höche, et al., Towards an all-orders calculation of the electroweak bubble wall velocity, J. Cosmol. Astropart. Phys. 03 (2021) 009, https://doi.org/10.1088/1475-7516/2021/03/009, arXiv:2007.10343 [hep-ph].
[225] Chiara Caprini, et al., Gravitational waves from decaying sources in strong phase transitions, arXiv:2409.03651 [gr-qc], Sept. 2024.
[226] Chiara Caprini, et al., Detecting gravitational waves from cosmological phase transitions with LISA: an update, J. Cosmol. Astropart. Phys. (ISSN 1475-7516) 2020 (03) (Mar. 2020) 024, https://doi.org/10.1088/1475-7516/2020/03/024.
[227] John Ellis, Marek Lewicki, José Miguel No, Gravitational waves from first-order cosmological phase transitions: lifetime of the sound wave source, J. Cosmol. Astropart. Phys. 07 (2020) 050, https://doi.org/10.1088/1475-7516/2020/07/050, arXiv:2003.07360 [hep-ph].
[228] Huai-Ke Guo, et al., Phase transitions in an expanding universe: stochastic gravitational waves in standard and non-standard histories, J. Cosmol. Astropart. Phys. 01 (2021) 001, https://doi.org/10.1088/1475-7516/2021/01/001, arXiv:2007.08537 [hep-ph].
[229] European Space Agency (ESA), Science requirements document (SciRD), https://www.cosmos.esa.int/documents/678316/1700384/SciRD.pdf, 2018.
[230] G.M. Harry, et al., LISA science requirements document, https://www.cosmos.esa.int/web/lisa/.
[231] Stanislav Babak, Antoine Petiteau, Martin Hewitson, LISA sensitivity and SNR calculations, arXiv:2108.01167 [astro-ph.IM], Aug. 2021.
[232] José Eliel Camargo-Molina, et al., All one-loop scalar vertices in the effective potential approach, J. High Energy Phys. 08 (2016) 073, https://doi.org/10.1007/JHEP08(2016)073, arXiv:1606.07069 [hep-ph].
[233] M.E. Carrington, Effective potential at finite temperature in the standard model, Phys. Rev. D 45 (Apr. 1992) 2933–2944, https://doi.org/10.1103/PhysRevD.45.2933, https://link.aps.org/doi/10.1103/PhysRevD.45.2933.
[234] T.D. Lee, A theory of spontaneous T violation, in: G. Feinberg (Ed.), Phys. Rev. D 8 (1973) 1226–1239, https://doi.org/10.1103/PhysRevD.8.1226.
[235] G.C. Branco, et al., Theory and phenomenology of two-Higgs-doublet models, Phys. Rep. 516 (2012) 1–102, https://doi.org/10.1016/j.physrep.2012.02.002, arXiv:1106.0034 [hep-ph].
[236] Vernon Barger, et al., Complex singlet extension of the standard model, Phys. Rev. D 79 (2009) 015018, https://doi.org/10.1103/PhysRevD.79.015018, arXiv:0811.0393 [hep-ph].
[237] Matthew Gonderinger, Hyungjun Lim, Michael J. Ramsey-Musolf, Complex scalar singlet dark matter: vacuum stability and phenomenology, Phys. Rev. D 86 (2012) 043511, https://doi.org/10.1103/PhysRevD.86.043511, arXiv:1202.1316 [hep-ph].
[238] Margarete Mühlleitner, et al., Phenomenological comparison of models with extended Higgs sectors, J. High Energy Phys. 08 (2017) 132, https://doi.org/10.1007/JHEP08(2017)132, arXiv:1703.07750 [hep-ph].
[239] Cheng-Wei Chiang, Michael J. Ramsey-Musolf, Eibun Senaha, Standard model with a complex scalar singlet: cosmological implications and theoretical considerations, Phys. Rev. D 97 (1) (2018) 015005, https://doi.org/10.1103/PhysRevD.97.015005, arXiv:1707.09960 [hep-ph].
[240] Abouabid Hamza, et al., Benchmarking di-Higgs production in various extended Higgs sector models, J. High Energy Phys. 09 (2022) 011, https://doi.org/10.1007/JHEP09(2022)011, arXiv:2112.12515 [hep-ph].

[241] J.R. Espinosa, T. Konstandin, A fresh look at the calculation of tunneling actions in multi-field potentials, J. Cosmol. Astropart. Phys. 01 (2019) 051, https://doi.org/10.1088/1475-7516/2019/01/051, arXiv:1811.09185 [hep-th].
[242] J.R. Espinosa, T. Konstandin, Exact tunneling solutions in multi-field potentials, J. Cosmol. Astropart. Phys. 03 (2024) 007, https://doi.org/10.1088/1475-7516/2024/03/007, arXiv:2312.12360 [hep-th].